Springer Theses
Recognizing Outstanding Ph.D. Research

Kinsuk Giri

Numerical Simulation of Viscous Shocked Accretion Flows Around Black Holes

Springer

Springer Theses

Recognizing Outstanding Ph.D. Research

Aims and Scope

The series "Springer Theses" brings together a selection of the very best Ph.D. theses from around the world and across the physical sciences. Nominated and endorsed by two recognized specialists, each published volume has been selected for its scientific excellence and the high impact of its contents for the pertinent field of research. For greater accessibility to non-specialists, the published versions include an extended introduction, as well as a foreword by the student's supervisor explaining the special relevance of the work for the field. As a whole, the series will provide a valuable resource both for newcomers to the research fields described, and for other scientists seeking detailed background information on special questions. Finally, it provides an accredited documentation of the valuable contributions made by today's younger generation of scientists.

Theses are accepted into the series by invited nomination only and must fulfill all of the following criteria

- They must be written in good English.
- The topic should fall within the confines of Chemistry, Physics, Earth Sciences, Engineering and related interdisciplinary fields such as Materials, Nanoscience, Chemical Engineering, Complex Systems and Biophysics.
- The work reported in the thesis must represent a significant scientific advance.
- If the thesis includes previously published material, permission to reproduce this must be gained from the respective copyright holder.
- They must have been examined and passed during the 12 months prior to nomination.
- Each thesis should include a foreword by the supervisor outlining the significance of its content.
- The theses should have a clearly defined structure including an introduction accessible to scientists not expert in that particular field.

More information about this series at http://www.springer.com/series/8790

Kinsuk Giri

Numerical Simulation of Viscous Shocked Accretion Flows Around Black Holes

Doctoral Thesis accepted by
the Jadavpur University, India

Springer

Author
Dr. Kinsuk Giri
National Tsing Hua University
Taiwan
People's Republic of China

Supervisor
Prof. Sandip K. Chakrabarti
S. N. Bose National Centre
for Basic Sciences
Kolkata
India

Title had been modified from "Numerical Simulation of Viscous Accretion Flows Around Black Holes Which Include Shocks"

ISSN 2190-5053 ISSN 2190-5061 (electronic)
ISBN 978-3-319-09539-4 ISBN 978-3-319-09540-0 (eBook)
DOI 10.1007/978-3-319-09540-0

Library of Congress Control Number: 2014947641

Springer Cham Heidelberg New York Dordrecht London

Printed on acid-free paper

Springer is part of Springer Science+Business Media (www.springer.com)

Supervisor's Foreword

When astronomers think of accretion flows around black holes, the first picture that comes in mind is the standard disc model of Shakura and Sunyaev (1973, hereafter SS73). Rightly so, since this model gives algebraic expressions for temperature, density, flux etc. as a function of radial distance from the black hole for various mass, mass accretion rate, viscosity parameter etc. However, as several authors, notably Sunyaev and Truemper (1979) showed, a multi-colour black body emission of SS73 disc fails to explain entire observed X-ray spectrum from a black hole candidate, especially high-energy radiation, generally known as a power-law component. Sunyaev and Titarchuk (1980, 1985) showed quantitatively that power-law component is due to repeated inverse Compton scattering of low-energy photons which interact with the electron cloud. Scientists made desperate attempts to find the source of this Compton cloud. It was generally believed that the cloud has to be somewhere close to the black hole (Zdziarski et al. 1994; Haardt and Maraschi 1994; Narayan and Yi 1994; Esin et al. 1997; etc.). However, these efforts only pushed the problem further: where is this elusive Compton cloud?

Meanwhile, in theoretical front, other ad-hoc and semi ad-hoc models were surfacing. For instance, efforts were on to 'mend' arbitrary chopping off of the disc by SS73 at an inner stable circular orbit or ISCO by a 'transonic component' (Muchotrzeb and Paczyński 1982). Radiation pressure-dominated thick accretion disc models of Polish group (Abramowicz et al. 1978; Paczyński and Wiita 1980), used pre-assigned angular momentum distribution and no advection. British group also came up with ion-pressure-supported tori which were of low-angular momentum, radiatively inefficient and hot (Rees et al. 1982). Advection-Dominated Accretion Flows (ADAF) assumed that inner SS733 disc can evaporate and resulting corona can emit very inefficiently.

Some purists, however, continue to struggle to find true configuration of accretion flows around a black hole and how it changes with flow parameters. Model to start with is clearly the Bondi flow (1952) solution which encompasses pressure and advection self-consistently. Our first job was to generalise Bondi flow solution by addition of angular momentum, viscosity and radiative transfer. Over the last 25 years, since Chakrabarti (1989), this was done with students and

collborators. First, only angular momentum and advection were added to Bondi flow (Chakrabarti 1989; Abramowicz and Chakrabarti 1990). It was truly, radiatively inefficient (the sense with which Narayan and Yi (1994) and others latter use the acronym ADAF) in that it conserves energy exactly and does not radiate anything at all. It allows solutions with standing shock waves and numerical simulations indicated that post-shock region is closest to what (non-accreting) solution of thick torus configuration (Paczyński and Wiita 1980; Rees et al. 1982) should have been, only more accurate, since it has advection and is now a part of a global solution and not just an ad-hoc model. Furthermore, post-shock region till inner sonic point (which Chakrabarti and collaborators termed as the CENtrifugal pressure-supported BOundary Layer, or CENBOL) produced winds and outflows also, a fraction of which goes off with flow angular momentum.

Next step was to include viscosity. For sub-critical α, ($<\alpha_{crit}$) flow continues to have a shock. For super-critical α ($>\alpha_{crit}$) topology changes dramatically and accretion flow becomes shock-free, Keplerian and can enter into a black hole through inner sonic point (Chakrabarti 1990a, b, 1996). Thus, all existing disc models are unified: one can have a subsonic, shock-free Keplerian disc for higher α; transonic advective discs (which could include shocks) for lower $\alpha$and thick torus in post-shock region, etc. Such a 'Keplerian' disc removes all deficiencies of an SS73 disc as it continues till the black hole horizon and has a significant advection close to the inner edge. Essential components of this most general solution including jets/outflows are shown in Fig. 1. CENBOL is the storehouse of thermal energy. This energy is extracted by soft-photons from the Keplerian disc through inverse Comptonization. Of course, whether all these components would be present simultaneously or not will depend on viscosity and mass supply rates (boundary conditions).

Does this generalised solution explain spectral and timing properties of black hole candidates? According to Chakrabarti and Titarchuk (1995) relative importance of Keplerian and sub-Keplerian accretion rates decide whether the black hole will be in soft or hard states. Cooling of CENBOL in soft state reduces outflows/jets (Garain et al. 2012). Oscillation of CENBOL, which takes place whenever cooling timescale inside CENBOL roughly agrees with infall timescale (Molteni et al. 1996; Chakrabarti, Acharyya and Molteni 2004; Garain et al. 2012). This oscillation produces observed quasi-periodic oscillations (QPOs) even in outburst sources (Ebisawa et al. 1996; Chakrabarti et al. 2008; Debnath et al 2008; Dutta et al. 2010).

However, there was a big caveat! Theoretical prediction of switching of solutions from a transonic radiatively inefficient flow with a CENBOL for sub-critical α to a generally Keplerian flow (having super-critical α) passing through the inner sonic point must be shown to lead to a stable configuration. The questions obviously were: Is there really a critical viscosity α_{crit} at which flow topology changes? If indeed α is higher on the equatorial plane (as is usually thought to be the reason for all the outbursting sources), then do we have a *stable* two-component configuration—both being separately transonic, even though one moves relatively slower compared to the other? Does the Keplerian component indeed weaken or in fact disappear, inside the CENBOL? How does the interface between the Keplerian

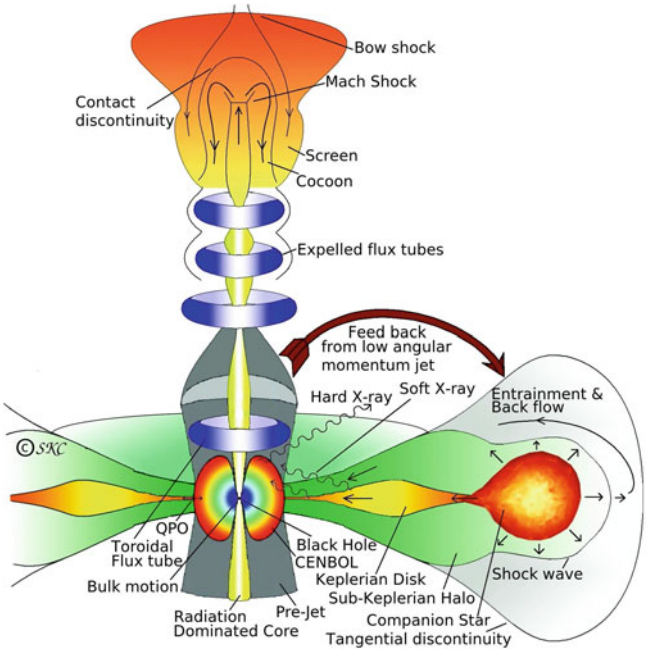

Fig. 1 Generalised TCAF with CENBOL, Keplerian and sub-Keplerian flows and the outflows (from Chakrabarti 2013)

component and the sub-Keplerian component behave? Does the oscillation of CENBOL produce quasi-periodic oscillations (QPOs) as observed in black hole candidates?

Thesis of Dr. Kinsuk Giri addresses precisely these very fundamental questions. He uses two-dimensional finite difference (using total variation diminishing or TVD criteria) code. This code was thoroughly described. Results of the code for inviscid flow were presented and it was shown that they agree with theoretical predictions. Then he describes implementation of viscosity in the code in great detail. In Chap. 4, he tests Bondi flow solution and checked that there is negligible dissipation in the code. From Chap. 5 onward new results on advective discs are presented. In Chap. 5, he showed that when Rankine–Hugoniot conditions are not fulfilled, flow still forms a shock, but it oscillates back and forth constantly trying to settle down. Reason for this behaviour is that if there is already a solution through outer sonic point, the solution through inner sonic point must require higher entropy and is favoured by the flow. He also showed that pre-shock flow behaves more like a conical flow, while post-shock region behaves like a flow in vertical equilibrium. Fourier transform of shock location clearly indicated sharp peaks where QPOs are observed in black hole candidates.

In Chap. 6, viscous flow was simulated for various α parameters. It was shown that there is a critical α (α_{crit} which depends on energy and angular momentum)

where solution topology changes as predicted before (Chakrabarti 1990a, b). Fig. 6.3 and Fig. 6.15 beautifully illustrate this point. Simulations clearly showed that for high α, the shock propagates away to 'infinity' leaving behind a Keplerian disc. Within sub-critical α regime, interesting result was found: he showed that as viscosity parameter is increased, outflow rate is decreased. This is because higher α transports away angular momentum on the equatorial plane, leaving behind lower angular momentum matter in the post-shock region which produces lesser centrifugally driven outflow.

Formation of a 'Keplerian' disc is a necessary condition, but it is not sufficient to have an SS73 type disc. 'Keplerian' flow must be cooled down to emit black body radiation. So, in Chap. 7 of his thesis, Dr. Giri showed that cooling triggers Keplerian component to settle down on the equatorial plane, raising its density farther till an equilibrium height is achieved. Figures 7.3a and 7.4a show this. Moreover, Keplerian and sub-Keplerian components co-exist without destroying each other. Inner disc puffs up by thermal pressure. It behaves as an ion-pressure-supported torus and acts as a Compton cloud. Thus, a single numerical simulation was able to unify all disc models existing in the literature.

What do we go from here? It is clear that in a truly self-consistent disc, photons have to be generated *ab initio* by thermal or magnetic bremsstrahlung process. They need to scatter in denser disc region in order to produce multi-colour black body spectrum from innermost disc. These photons would then be inverse Comptonized by otherwise radiatively inefficient sub-Keplerian halo, giving up their own thermal energy so as to produce harder X-rays. Another point of interest would be to see how weaker magnetic fields are stretched out to produce dynamically important toroidal fields which are ejected from the halo in order to produce collimation for the jets (Fig. 1). Dynamics of these magnetic tori would be interesting: thicker filaments would be diverted to vertical direction while thinner filaments would be advected into CENBOL as drag force takes into effect. Since it is believed that tension would be the strongest force inside a CENBOL (Chakrabarti and D'Silva 1994; Nandi et al. 2001), the filaments are expected to collapse by tension destroying CENBOL momentarily and squirting matter out as relativistic jets. Spectrum at this stage should soften. That would resolve remaining long standing problems of acceleration and collimation of jets, and cause of variabilities of light curves in enigmatic black hole candidates, such as GRS 1915 + 105.

Kolkata, India, August 2014 Prof. Sandip K. Chakrabarti

References

Abramowicz, M., Jaroszynski, M., & Sikora, M. (1978). *Astronomy and Astrophysics, 63,* 22.
Abramowicz, M., & Chakrabarti. S. K. (1990). *Astrophysical Journal, 350,* 281.
Bondi, H. (1952). *MNRAS, 112,* 195.
Chakrabarti, S. K. (1989). *Astrophysical Journal, 347,* 365.

Chakrabarti, S. K. (1990a). *Theory of Transonic Astrophysical Flows.* Singapore: World Scientific.
Chakrabarti, S. K. (1990b). *MNRAS, 243,* 610.
Chakrabarti, S. K., & Titarchuk, L. G. (1995). *Astrophysical Journal, 455,* 623.
Chakrabarti, S. K. (1996). *Physics Reports, 266,* 229.
Chakrabarti, S. K. (2013). Recent trends in the study of compact objects. In S. Das, A. Nandi & I. Chattopadhyay (Eds.), *Theory and Observation* (p. 1).
Chakrabarti, S. K., Acharyya, K., & Molteni, D. (2004). *Astronomy and Astrophysics, 421,* 1.
Chakrabarti, S. K., Debnath, D., Nandi, A., & Pal, P. S. (2008). *Astronomy and Astrophysics, 489,* 41.
Chakrabarti, S. K., & D'Silva, S. (1994). *Astrophysical Journal, 424,* 138.
Debnath, D., Chakrabarti, S, K., Nandi, A., & Mandal, S. (2008). *BASI, 36,* 151.
Dutta, B. G., & Chakrabarti, S. K. (2010). *MNRAS, 404,* 2136.
Ebisawa, K., Ueda, Y., Inoue, H., Tanaka, Y., & White, N. E. (1996). *Astrophysical Journal, 467,* 419.
Esin, A. A., McClintock, J. E., & Narayan, R. (1997). *Astrophysical Journal, 489,* 865.
Haardt, F., Maraschi, L., & Ghisellini, G. (1994). *Astrophysical Journal, 432,* 95.
Garain, S., Ghosh, H., & Chakrabarti, S. K. (2012). *Astrophysical Journal, 758,* 114.
Molteni, D., Ryu, D., & Chakrabarti, S. K. (1996). *Astrophysical Journal, 470,* 460.
Muchotrzeb, B., & Paczyński, B. (1982). *Acta Astron., 32,* 1.
Nandi, A., Chakrabarti, S. K., Vadawale, S. V., & Rao, A. R. (2001). *Astrophysical Journal, 380,* 245.
Narayan, R., & Yi. (1994). *Astrophysical Journal, 428,* 13.
Paczyński, B., & Wiita, P. J. (1980). *Astronomy and Astrophysics, 88,* 23.
Rees, M. J., Begelman, M. C., Blandford, R. D., & Phinney, E.S. (1982). *Nature, 295,* 17.
Shakura, N. I., & Sunyaev, R. A. (1973). *Astronomy and Astrophysics, 24,* 337.
Sunyaev, R. A., & Titarchuk, L. G. (1980). *Astronomy and Astrophysics, 86,* 121.
Sunyaev, R. A., & Titarchuk, L. G. (1985). *Astronomy and Astrophysics, 143,* 374.
Sunyaev, R. A., & Truemper, J. (1979). *Nature, 279,* 506.
Zdziarski, A. A., Zycki, P. T., Svensson, R., & Boldt, E. (1994). *Astrophysical Journal, 429,* 928.

Preface

The process by which a massive compact object (like white dwarfs, neutron stars, black holes etc) gravitationally captures ambient matter is called accretion. The accretion of matter on to a compact massive star is the likely source of energy in the observed binary X-ray sources. Since black holes are 'black', there cannot be any direct observational evidence of them. Thus they must be observed by detecting the radiations emitted by accreting matter. For typical gas dynamical conditions found in the interstellar medium and in the matter exchanged between the binary stars, it is expected that accretion flows on to compact objects will be hydrodynamical or magneto-hydrodynamical in nature. Thus, to study black hole accretion, it is necessary to know the hydrodynamic properties of the flow of the matter as it is the matter which, after all, will emit the radiation that we detect by satellites. The variation of thermodynamic quantities such as the initial energy density of the accreted matter plays important roles as the emitted radiation intensity from the flow depends on the density and the temperature at each point of the flow at each moment of time. So the spectral and temporal properties of emitted radiations are directly determined by the hydrodynamical variables.

In my Ph.D. work, I mainly made effort to study the hydrodynamic properties of the flow and its stability properties through time-dependent numerical simulations. We started with time-dependent solutions of one-dimensional (spherically symmetric) and two-dimensional (axially symmetric) accretion flows around compact objects, in particular black holes, after examining the steady-state solutions. We describe the development of a two-dimensional hydrodynamic code and its application to various astrophysical problems. A FORTRAN code for two-dimensional numerical hydrodynamics has been developed to model viscous accretion discs. We employ a grid-based finite difference method called the total variation diminishing method (TVD). The effective shear viscosity present in the code is evaluated. The simulations were carried out for flows in the Schwarzschild geometry. By numerical simulation, we show that the theoretical solutions (with or without shocks) which are claimed to be stationary are indeed so. When the shocks are absent, they show steady oscillations. Our survey was carried out using the entire inflow parameter space spanned by the specific energy, angular momentum, shear viscosity and a

power-law cooling. It is believed that high-viscosity flows reside on the equatorial plane, and supply low energy X-rays, while the low-viscosity and low-angular-momentum flows fall rapidly on to the black holes away from the equatorial plane and have little time to radiate X-rays. However, they can energise low-energy photons and produce hard X-rays and contribute to the spectrum of black holes candidates. In the thesis work, for the first time, numerically we have simulated two-component advective flows (TCAF) where a cold Keplerian disc is surrounded by hot sub-Keplerian flow. Interestingly, we have found the stability of this flow. It is believed that the soft-photons originated from the low-temperature Keplerian discs are reprocessed by the hot electrons of CENBOL through the inverse-Comptonisation process. They are emitted as hard X-rays. Thermal pressure gradient force at the shock location becomes significant in the transverse direction which drives matter upward and downward in the from of jets or outflows. These X-rays and outflows are observed.

Accretion flow dynamics during an outburst phase of transient BHCs can be explained by a model analysis of spectral and temporal behaviour of the source. The spectral and temporal properties of the black hole candidates can be explained using several models, which generally include two components, namely a Keplerian disc and a hot corona, only the nature of the corona varies from model to model. In the observational prospect, TCAF model requires two accretion rates, namely the Keplerian disc accretion rate and the halo accretion rate, the latter being composed of a sub-Keplerian, low-angular-momentum flow which may or may not develop a shock. In this solution, the relevant parameter is the relative importance of the halo (which creates the Compton cloud region) rate with respect to the Keplerian disc rate (soft photon source). Since last decade, TCAF model has been used to manually fit data of several black hole candidates quite satisfactorily. Quasi-periodic oscillations (QPOs) observed in X-rays are very important features for the study of accreting black holes. Observations and possible explanations of QPOs in black hole candidates have been reported quite extensively in the literature. Low- and intermediate-frequency QPOs in black hole candidates are believed to be due to oscillations of the shocks, i.e. Comptonising regions in an accretion flow. Using our simulated TCAF, one can numerically simulate the light curves emitted from an accretion disc for different accretion rates and also can find how the QPO frequencies vary. Thus the explanations of spectral and timing properties of galactic and extra-galactic black holes based on TCAF models appear to have firm foundation.

In Chap. 1, we explain the terms associated with the title of the thesis. First, we discuss the general view of accretion processes around compact objects, in particular around black holes. Then, we point out the basic properties of accretion around non-rotating black holes. In case of the black hole physics, a full general relativistic approach is recommended, but it makes the time-dependent hydrodynamic equation which includes radiative transfer very complex. This problem is circumvented using a pseudo-Newtonian potential. We briefly discuss the governing equations for fluid dynamical study in a pseudo-Newtonian geometry. Subsequently, we discuss the mathematical aspects of shock waves and their

presence in accretion processes. Historical studies of spherical accretion process through various approaches are briefly presented. We start with the Bondi flow for spherical accretion of an ordinary star. A qualitative discussion on the development of disc accretion process is also presented. We then discuss the standard Keplerian disc model. This model explains the nature of the multi-colour soft X-ray spectrum very well but it fails to explain very high-energy radiation coming from the stellar mass black holes and distant Quasars and AGNs. This brings the advective flows in the picture. This component has lower angular momentum than a Keplerian disc, and is called a sub-Keplerian flow. A realistic accretion flow may have both the components, a sub-Keplerian flow surrounding a Keplerian flow. This is the so-called two-component advective flow or TCAF model of Chakrabarti and Titarchuk.

In Chap. 2, we give an overview on the past works done on numerical simulation for accretion flows around black holes. We start with non-viscous cases. We also point out some important simulations of viscous accretion discs. In the last Section of this Chapter, we present the precise goals for this thesis work.

Chapter 3 describes the numerical methods employed to model accretion flows and their implementation in a FORTRAN code. We present all the governing equations for both non-viscous and viscous flows. We discuss the solution technique for a non-viscous system. Subsequently, we give all the schemes to incorporate turbulent viscosity in the non-viscous system. Finally, we add a power-law cooling in our viscous system and study the properties.

In Chap. 4, we pointed out the procedure of simulation and the computational box in details. We study the accretion processes on a black hole by numerical simulation. We use a grid-based finite difference code for this purpose. Tests of the code are made using the flow without angular momentum, namely, the Bondi flow.

In Chap. 5, we scan the parameter space spanned by the specific energy and the angular momentum of the inflow and compare the time-dependent solutions with those obtained from theoretical considerations. We found several important results: (a) The time-dependent flow behaves close to a constant height model flow in the pre-shock region and a flow in vertical equilibrium in the post-shock region. (b) The infall time scale in the post-shock region is several times longer than the free-fall time scale. (c) There are two discontinuities in the flow, one being just outside of the inner sonic point. Turbulence plays a major role in determining the locations of these discontinuities. (d) The two discontinuities oscillate with two different frequencies and the post-shock flow behaves as a coupled harmonic oscillator. A Fourier analysis of the variation of the outer shock location indicates a higher power at the lower frequency and lower power at the higher frequency. The opposite is true when the analysis of the inner shock is made. These behaviours will have implications in the spectral and timing properties of the black hole candidates.

In Chap. 6, we study the time evolution of a rotating, axisymmetric, viscous accretion flow around black holes using a grid-based finite difference method. We use the Shakura-Sunyaev viscosity prescription. However, we compare with the results obtained when all the three independent components of the viscous stress are kept. We show that the centrifugal pressure-supported shocks become weaker with

the inclusion of viscosity. The shock is formed farther out when the viscosity is increased. When the viscosity is above a critical value, the shock disappears altogether and the flow becomes subsonic and Keplerian everywhere except in a region close to the horizon, where it remains supersonic. We also find that as the viscosity is increased, the amount of outflowing matter in the wind is decreased to less than a percentage of the inflow matter. Since the post-shock region could act as a reservoir of hot electrons or the so-called Compton cloud, the size of which changes with viscosity, the spectral properties are expected to depend on viscosity strongly: the harder states are dominated by low-angular momentum and the low-viscosity flow with significant outflows while the softer states are dominated by the high-viscosity Keplerian flow having very little outflows.

In Chap. 7, we carry out a series of numerical simulations of viscous accretion flows having a reasonable spatial distribution of the viscosity parameter. We add the power-law cooling throughout the flow. We show that in agreement with the theoretical solutions of viscous transonic flows, matter having viscosity parameter above a critical value becomes a Keplerian disc while matter having lesser viscosity remains a low-angular momentum, sub-Keplerian flow. The latter component produces centrifugal pressure-supported shock waves. Thus, for instance, the flows having sufficiently high viscosity on the equatorial plane and low viscosity above and below, produce a Two-Component Advective Flow (TCAF) where a Keplerian disc is surrounded by a rapidly moving sub-Keplerian halo. We find that the post-shock region of the Keplerian disc is evaporated and the configuration is stable. This agrees with the theoretical models which attempt to explain the spectral and timing properties of black hole candidates.

Finally, in Chap. 8, we draw concluding remarks and briefly mention our future plans.

List of Publications

1. Kinsuk Giri and S. K. Chakrabarti, **Hydrodynamic Simulation of Two Component Advective Flows Around Black Holes**, *Mon. Not. R. Astron. Soc.*, 430, 4, (pp 2836–2843) (2013)

2. Kinsuk Giri and S. K. Chakrabarti, **Hydrodynamic Simulations of Viscous Accretion Flows Around Black Holes**, *Mon. Not. R. Astron. Soc.*, 421, 1, (pp 666–678) (2012)

3. H. Ghosh, S. K. Garain, Kinsuk Giri and S. K. Chakrabarti, **Effects of Compton Cooling on the Hydrodynamic and the Spectral Properties of a Two-Component Accretion Flow Around a Black Hole**, *Mon. Not. R. Astron. Soc.*, 416, 1, (pp 959–971) (2011)

4. H. Ghosh, S. K. Garain, Kinsuk Giri, S. K. Chakrabarti, **Monte Carlo Simulations of Comptonization Process in a Two Component Accretion Flow Around a Black Hole in Presence of an Outflow**, *Proc. 12th Marcel Grossman Meeting on General Relativity, Eds. T. Damour, R. T. Jantzen & R. Ruffini*, World Scientific (pp 985–989) (2011)

5. Kinsuk Giri, S. K. Chakrabarti, M. M. Samanta and D. Ryu, **Hydrodynamic simulations of oscillating shock waves in a sub-Keplerian accretion flow around black holes**, *Mon. Not. R. Astron. Soc.*, 403, 1, (pp 516–524) (2010)

6. S. K. Chakrabarti, S. K. Mondal,….., Kinsuk Giri,…, **VLF signals in summer and winter in the Indian sub-continent using multi-station campaigns**, *Indian J. Phys.*, 2012, 86, (pp 323–334) (2012)

Acknowledgments

In the first place, I owe my deepest gratitude to Prof. Sandip K. Chakrabarti for giving me the opportunity to work with him. He has taught me how to think like a scientist and how to prepare scientific writings clearly. I also thank him as a teacher, especially for the lesson that one should take the time to start from fundamental theory, and the importance of deriving even "basic" equations before applying them to a problem.

I would like to thank all the academic and non-academic staff of the S. N. Bose National Centre for Basic Sciences for their enthusiastic support during my Ph.D. period. I express my gratitude to the Director of SNBNCBS, Prof. A.K. Ray-Chaudhuri for giving me the opportunity to work here. I would like to thank Prof. Dongsu Ryu for his kind collaboration with me. In particular, the hydrodynamic code which I have developed to include viscosity and cooling is based on one basic inviscid code that Dongsu developed. I want to thank my collaborators Himadri Ghosh, Sudip K. Garain: it is a pleasure to collaborate with you!

I would also like to acknowledge the Abdus Salam International Centre for Theoretical Physics, Trieste, Italy, for giving me an opportunity to participate in the Winter School on Numerical Astrophysics in November, 2011. I would like to thank the organiser of International conference on Accretion and Outflow in Black Hole Systems, and South Asian Physics Foundation (SAPF) for giving me the opportunity to attend the conference and financial support at Kathmandu in 2010. I also would like to thank to the organiser of 13th Marcel Grossmann Meeting for providing me the opportunity to attend the conference and financial support at Stockholm in 2012. Finally, I would like to thank the Kyoto University for giving me an opportunity and financial support to attend 5th East Asia Numerical Astrophysics Meeting at Kyoto University in 2012. Attending them has improved my understanding of the subject and the thesis.

I would like to thank all the members of Indian Centre for Space Physics (ICSP) for providing a broad spectrum of Astrophysics. In particular, I would like to thank Dr. Ankan Das, Dr. Dipak Debnath and Mr. Liton Majumder at ICSP for providing me some important suggestions related to my work.

I would like to show my gratitude to all my seniors in S. N. Bose National Centre for Basic Sciences. They have made available their support in various number of ways. In particular, I would like to show my special gratitude to Dr. Indranil Chattopadhyay, Dr. Santarata Das for their generous help and friendly behaviour which boosted me to carry on my research work. I would also like to thank the members of my thesis committee, Prof. Parthasarathi Majumdar and Prof. Debashis Gangopadhyay for their time and insightful questions.

My heartiest thanks go to my friends and colleagues in SNBNCBS, with whom I have shared my stay here. Particularly, I must mention the names of Himadri, Sudip, Sujay, Wasim, Tamal, Arnab and Abhisek with whom I have shared moments of various shades.

Finally, I am ever indebted to my parents and my other family members for their tireless endeavour to help me for the completion of my work.

Contents

Chapter 1
Introduction

Abstract We explain the terms associated with the title of the thesis. First, we discuss the general view of accretion processes around compact objects, in particular around black holes. Then, we point out the basic properties of accretion around non-rotating black holes. In the case of black hole physics, a full general relativistic approach is recommended, but it makes the time-dependent hydrodynamic equation, which includes radiative transfer, very complex. This problem is circumvented using a pseudo-Newtonian potential. We briefly discuss the governing equations for fluid dynamical study in a pseudo-Newtonian geometry. Subsequently, we discuss the mathematical aspects of shock waves and their presence in accretion processes. Historical studies of the spherical accretion process through various approaches are briefly presented. We start with the Bondi flow for spherical accretion of a normal star. A qualitative discussion on the development of the disc accretion process is also presented. We then discuss the standard Keplerian disc model. This model explains the nature of the multi-coloured soft X-ray spectrum well but fails to explain the high energy radiation coming from stellar mass black holes and distant Quasars and AGNs. This brings advective flows into the picture. This component has lower angular momentum than a Keplerian disc, and is called a sub-Keplerian flow. A realistic accretion flow may have both components, a sub-Keplerian flow surrounding and a Keplerian flow. This is the so-called two-component advective flow or TCAF model of Chakrabarti and Titarchuk.

A black hole is the most COMPACT of gravitating objects in the sky. Briefly, 'Compact Objects' are born when a normal star dies. Compact stars are broadly grouped into white dwarfs, neutron stars and black holes. The key factor that determines whether a star ends up as a white dwarf, a neutron star or a black hole is believed to be the star's initial mass. When a massive star has exhausted most of the nuclear fuels in its core, the core collapses and a compact star is created. In general, these stars differ from normal stars due to their exceedingly small size. As a result, they have stronger gravitational attraction. As compact stars do not have nuclear fuel to burn, they are unable to generate internal thermal pressure to protect them from inward gravitational collapse. In case of white dwarfs, inward gravitational pressure at the core is supported by electron degeneracy pressure, while for neutron stars the support comes from the pressure of degenerate neutrons. However, black holes are

K. Giri, *Numerical Simulation of Viscous Shocked Accretion Flows Around Black Holes*,
Springer Theses, DOI 10.1007/978-3-319-09540-0_1

fully collapsed and nothing can neutralize the gravitational pull. This leads to their collapse to singularity. It is believed that white dwarf stars originated from lighter mass progenitor stars, while neutron stars and black holes originated from more massive stars.

Of all the celestial objects, black holes are the simplest in form. The defining feature of a black hole is the appearance of an event horizon, a boundary in space-time through which matter and light can only pass inward towards the centre of the black hole. All matter enters into its event horizon at the speed of light and thus the inner boundary condition is fixed, independent of the mass of black holes or the origin of the accreting matter. Nothing, not even light, can escape from inside the event horizon. The simplest among the black holes is the Schwarzschild black hole, which is a non-rotating black hole characterised only by its mass M.

Accretion flows are common in a variety of astrophysical systems, including young stars, X-ray binaries and active galactic nuclei. The goal of the study of accretion processes is to understand the basics of how matter enters into black holes both theoretically as well as through numerical simulations, including the hydrodynamics and radiations emitted from the matter before entering a black hole. Eventually, one requires to fit the observation of radiations coming from individual systems. Scientists have been trying to understand accretion flows around black holes for the last five decades. Much theoretical work has been done on accretion models around black holes. The main purpose is to know the distribution of (a) the density, radial velocity and angular velocity of the accretion gas as a function of radius and time by solving the basic equations of hydrodynamics, (b) the temperature of matter by solving energy equation with account of viscosity and radiative losses and (c) angular momentum inside the flow and the way the angular momentum is transported. A complete analytical solution of this problem does not exist, in part because some of the physics is not fully known (e.g. viscous effects and the effects of radiative losses). Hence, in this thesis we will mainly study the hydrodynamic properties of flow and its stability properties through time-dependent numerical simulations.

1.1 Properties of Black Holes in a Nutshell

A region of space-time into which signals can enter, but from which no signal can ever emerge, is called a black hole. Based on a simple calculation using Newton's gravitational theory, the existence of no-escape radius for light was suggested by Laplace more than 200 years ago. The energy condition for a body of mass m starting with velocity v to escape to infinity from the surface of a star of mass M and radius R requires that the initial kinetic energy exceeds the gravitational binding energy:

$$\frac{mv^2}{2} \geq \frac{GMm}{R},$$

i.e.

$$v \geq \sqrt{\frac{2GM}{R}},$$

where, G is the universal gravitational constant. Escape is only possible for velocities greater than $\sqrt{2GM/R}$. If the radius of the star is reduced, the escape velocity increases until eventually it reaches the velocity of light. At this stage the radius is

$$r_g = \frac{2GM}{c^2}, \tag{1.1}$$

where, c is the velocity of light. When even light cannot escape from a star, such a star will become invisible. Using full general relativity theory of Einstein, Laplace's radius was found to be a correct estimate, though for an entirely different reason. Laplace's result is based on the assumption that stars of arbitrary mass may be compactified to an arbitrarily small size and yet they remain stable—an assumption that is known to be wrong due to gravitational instability.

The Schwarzschild solution of the gravitational field equations in the vacuum region surrounding a point mass M is given as

$$\mathrm{d}s^2 = \left(1 - \frac{2GM}{c^2 r}\right) c^2 \mathrm{d}t^2 - \frac{\mathrm{d}r^2}{\left(1 - \frac{2GM}{c^2 r}\right)} - r^2 \left(\mathrm{d}\theta^2 + \sin^2\theta\, \mathrm{d}\varphi^2\right). \tag{1.2}$$

The metric develops a singularity as $r \to \frac{2GM}{c^2}$. At this point,

$$g_{00} = \left(1 - \frac{2GM}{c^2 r}\right) \to 0,$$

and

$$g_{11} = -\frac{1}{\left(1 - \frac{2GM}{c^2 r}\right)} \to \infty.$$

The quantity $r_g = \frac{2GM}{c^2}$ is called the Schwarzschild radius or the gravitational radius of mass M. If a spherical star is compressed by some astrophysical processes to a radius smaller than the Schwarzschild radius, then the gravitational collapse necessarily follows and collection of the entire matter at $r = 0$ is inevitable. If the Sun were to become a black hole, the r_g would be only 3 km.

1.2 Gravitational Fields Around a Black Hole

From the metric above, we note that for $r >> r_g$, the metric is Newtonian and thus Newton's laws of gravity prevails. However, at $r \sim r_g$, the general-relativistic effects are important. For a wide range of accretion problems, such as in the case of binary systems consisting of non-compact stars, the Newtonian theory of gravity is adequate for the description of background gravitational forces. Extensive experience with Newtonian astrophysics has shown that explorations of the relativistic regime can also benefit from the use of model potentials, one of which is the well-known Paczyński-Wiita pseudo-Newtonian potential that can be used around a Schwarzschild black hole. Paczyński and Wiita (1980) potential is given as

$$\Phi = -\frac{GM}{(r - \frac{2GM}{c^2})}. \tag{1.3}$$

Fortunately, the Keplerian distribution of angular momentum and the locations of the marginally bound and marginally stable orbits as derived from this potential match exactly those obtained from the exact general relativity theory. Hence, we carry out our simulations assuming this potential. There is a similar potential for a rotating black hole also. We now briefly describe the effective potential both of the general relativistic and the pseudo-potential approach.

1.2.1 General Relativistic Approach

In the spherical polar coordinate system, adopting the gravitational constant G, the central mass M and the velocity of light c to be unity ($G = M = c = 1$), the Schwarzschild metric Eq. 1.2 is given as

$$\mathrm{d}s^2 = -(1 - 2/r)\,\mathrm{d}t^2 + (1 - 2/r)^{-1}\,\mathrm{d}r^2 + r^2\mathrm{d}\theta^2 + r^2 sin^2\theta \mathrm{d}\phi^2. \tag{1.4}$$

Solving the geodesic equation one obtains

$$-u_t = (1 - 2/r)\,u^t = E = \text{constant of motion}, \tag{1.5}$$

and, for $\theta = \pi/2$,

$$u_\phi = r^2 u^\phi = l = \text{constant of motion}. \tag{1.6}$$

Using the above equations in GR, the equation for the radial coordinate r of a test particle orbiting a non-rotating black hole can be written as

$$\left(\frac{\mathrm{d}r}{\mathrm{d}s}\right)^2 = E^2 - \left(1 - \frac{2}{r}\right)\left(1 + \frac{l^2}{r^2}\right). \tag{1.7}$$

The second term on the RHS of Eq. 1.7 behaves like an effective potential ($V_{\rm eff}$),

$$V_{\rm eff}^2 = \left(1 - \frac{2}{r}\right)\left(1 + \frac{l^2}{r^2}\right), \tag{1.8}$$

or

$$V_{\rm eff} = [\left(1 - \frac{2}{r}\right)\left(1 + \frac{l^2}{r^2}\right)]^{\frac{1}{2}}. \tag{1.9}$$

By defining an effective potential $V_{\rm eff}$, one can classify the possible trajectories/orbits as in classical mechanics.

The gravitational potential that a test particle around a Newtonian star feels is given as

$$\Phi_N = -\frac{1}{r}. \tag{1.10}$$

The effective potential of a rotating gas with specific angular momentum l is obtained by summation of the gravitational potential and the centrifugal potential.

$$V_{\rm Newt}(r) = 1 + \Phi_N + \frac{1}{2}\frac{l^2}{r^2}. \tag{1.11}$$

Here, we added the rest mass '1' to compare with GR results.

In Fig. 1.1 we plot both $V_{\rm eff}$ and $V_{\rm Newt}$ against r to compare the GR potential with the Newtonian one. We see some remarkable features. First, we notice that for small r, $V_{\rm eff}$ dives down decreasing r and $V_{\rm eff} = 0$ at $r = r_g = 2$. r_g is called the event horizon or the Schwarzschild radius. Second, no matter how hard one throws a particle at a Newtonian star it will bounce back, while a black hole definitely consumes a particle if it is thrown 'hard' enough. The particle enters the black hole in trajectories known as 'capture orbits'. We will focus on the bound particles. Conditions for the circular orbits are: (a) $\frac{\delta V_{\rm eff}}{\delta r} = 0$ and, (b) $\frac{{\rm d}r}{{\rm d}s} = 0$. Condition (a) gives the following equation:

$$r^2 - l^2 r + 3l^2 = 0. \tag{1.12}$$

Thus, for $l \geq 2\sqrt{3}$, the real values of r exist, which implies $V_{\rm eff}$ has an extremum for $l \geq 2\sqrt{3}$. For $l = 2\sqrt{3}$, we have the position for the *last stable orbit* or the *marginally stable orbit* (r_{ms}; shown in Fig. 1.1). Putting $l = 2\sqrt{3}$ in Eq. 1.12, we get $r_{ms} = 6$. Imposing condition (b) in Eq. 1.9, and using Eq. 1.12 we get

$$E^2 = \frac{(r-2)^2}{r\,(r-3)}. \tag{1.13}$$

If we take the definition of specific angular momentum as $-u_\phi/u_t$ (e.g., Chakrabarti 1996), the specific Keplerian angular momentum curve is the locus of the extrema

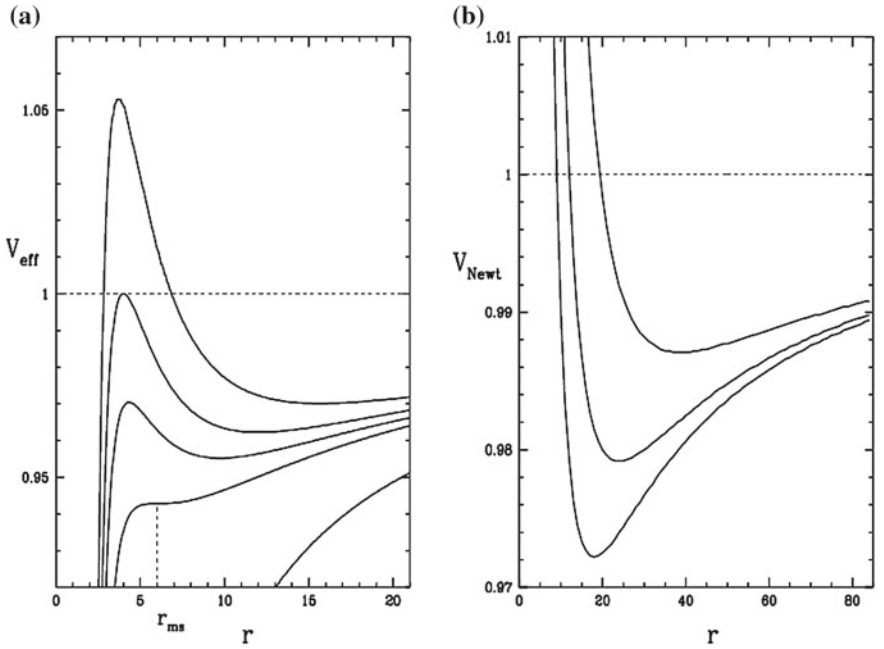

Fig. 1.1 Comparison of general relativistic (*a*) and Newtonian (*b*), effective potentials. **a** The effective potential V_{eff} is drawn for values of $l = 0$, 3.464, 3.75, 4 and 4.4, from the lowest curve upwards, respectively. r_{ms} is the marginally stable radius. The *dotted line* for which $V_{\text{eff}} = 1$ denotes rest mass energy of particle falling into the *black hole*. **b** The Newtonian effective potential V_{Newt} is drawn for the values of $\ell = 3$, 3.464 and 4.4 from the lowest curve upwards, respectively (Chattopadhyay, 2003)

of V_{eff}. Hence,

$$\lambda^2_{\text{Kep}} = \left(-\frac{u_\phi}{u_t}\right)^2 = \frac{r^3}{(r-2)^2}. \tag{1.14}$$

Putting $r = 6$ and $l = 2\sqrt{3}$ into Eq. 1.9, we have

$$V_{\text{eff}}(r_{ms}) = \sqrt{\frac{8}{9}}. \tag{1.15}$$

Therefore, the binding energy at r_{ms} is

$$E_{\text{bind}} = 1 - \sqrt{\frac{8}{9}} = 5.72\,\%. \tag{1.16}$$

When a particle enters into a black hole, E_{bind} amount of energy will be liberated as radiation.

1.2.2 Pseudo-Newtonian Approach

In the case of most astrophysical systems involving a rotating compact star or a black hole, it is not essential that one solves the problem using full general relativity. As long as one is not interested in processes very close (within r_g to $2r_g$, say) to the horizon, one may safely use the so-called *Paczyński-Wiita potential* (Paczyński and Wiita 1980). Paczyński-Wiita potential or the pseudo-Newtonian potential is given as

$$\Phi_{\rm PW} = -\frac{1}{(r-2)}. \tag{1.17}$$

Adding the rest mass energy to this potential and then writing the effective potential

$$V_{\rm eff(PW)} = 1 + \frac{l^2}{2r^2} + \Phi_{\rm PW}. \tag{1.18}$$

Putting the condition $\delta V_{\rm eff(PW)}/\delta r = 0$, we get

$$l^2_{\rm Kep} = \frac{r^3}{(r-2)^2}. \tag{1.19}$$

We find that the specific Keplerian angular momentum distribution produced by $\Phi_{\rm PW}$ is the same as that produced by exact GR calculations. We have already seen that r_{ms} is the position of the minima of the Keplerian angular momentum. Taking the minima of Eq. 1.19, we find, $r_{ms} = 6$.

Note that we are using two different notations for the specific angular momentum: in GR we use λ and in pseudo-Newtonian potential we use ℓ to differentiate these two approaches. The binding energy at r_{ms} in pseudo-Newtonian description is

$$E_{\rm bind} = 1 - V_{\rm eff(PW)}\,(r_{ms}) = 6.25\,\%. \tag{1.20}$$

Thus, we find that the pseudo-Newtonian approach is quite accurate, and the error is within a few per cents. In the following chapters, we shall use $\Phi_{\rm PW}$ to take care of the general relativistic effects.

1.2.3 Fate of Matter When It Approaches the Innermost Stable Orbit

As matter slowly drifts radially inwards in an accretion disc (probably determined by the viscosity), roughly half of the gravitational energy of the matter is released and radiated away if the disc is Keplerian (in the Newtonian case anyway). Once it

reaches the innermost stable orbit, matter will rapidly fall into the black hole (i.e. pass through the event horizon) taking with it its total mass-energy (including all of its kinetic energy), adding to the mass of the black hole without further radiating away much of its energy. Therefore, the binding energy at the innermost stable orbit limits the maximum energy that can be radiated away by an accreting black hole.

1.3 Accretion Processes: General Views

In the astrophysical context, the process in which diffuse gas or matter is accumulated around a compact object under the influence of gravity is called 'accretion'. In other words, accretion is a process in which gas and dust are accumulated around massive celestial objects which could be stars, planets or any massive objects. The importance of accretion as power source was first widely recognized in the study of binary systems, especially X-ray binaries. There are two main reasons for which the matter can be supplied to the compact object from the companion. At the time of its evolution, one of the stars in the binary system may increase in radius, or the distance between them may shrink such that the gravitational pull of the companion can remove the outer layers of its envelope. This is called the Roche lobe overflow. On the other hand, at some evolutionary phase, one of the stars may eject some of its mass in the form of the stellar wind. This ejected material will be captured gravitationally by companion. This process is known as wind accretion. Isolated compact stars with mass $M \sim M_{\odot}$ may also be accreting gas as they wander through the interstellar medium of our galaxy. The number of such objects could be considerable. Thus accretion is a process that can be considerably more efficient as a cosmic energy source than many other commonly invoked mechanisms in astrophysics. Calculations of accretion flows onto a compact star and the emitted radiation pattern are very complex. Suppose the effective mean free path of gas particles is sufficiently short that the flow is hydrodynamical in nature, first, one must determine the flow geometry. In general, if the gas possesses intrinsic angular momentum, the flow will be two or three dimensional, depending on the flow symmetry. In simple cases, the flow may be spherical (a star dipped inside a static gas cloud) or disc-like (as in axisymmetric flow of gas with intrinsic angular momentum). Matter falling into a compact star tends to form a disc because an initially spherical mass of gas that starts spinning will tend to flatten out. The faster it spins, the flatter it gets. So, if the falling material is orbiting around the central mass, the spinning flattens the matter into an accretion disc.

Figure 1.2 shows an accretion disc in a binary system. The yellow star on the right is filling its Roche lobe and matter is therefore streaming over the compact object on the left. Since the accreted matter possesses a significant amount of angular momentum, it cannot fall directly onto the compact object, instead it forms an accretion disc surrounding the compact object.

In general, some matter is assumed to rotate in Keplerian orbits inside an accretion disc. But this is only possible when it is in equilibrium, i.e. gravity is balanced by the

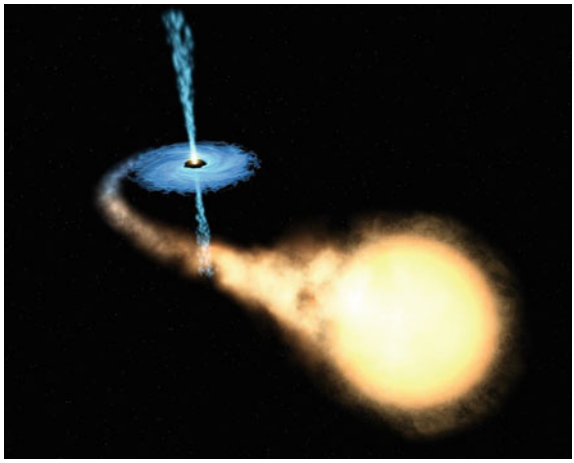

Fig. 1.2 Artist's visualization of a binary system. This figure has been taken from "http://upload.wikimedia.org/wikipedia/commons/2/2a/Accretion_disk.jpg"

centrifugal force and gas is sufficiently cold and has only rotational motion. If this is the case, then nothing would have ever happened inside the accretion disc. In this situation, matter would just go on revolving around the accreting star forever. However, this is not what happens because of viscosity which transports momentum, and therefore angular momentum. The role of viscosity is to transfer angular momentum from one gas layer to another which is further out from the accreting object. The first gas layer will then move slightly closer to the accreting object as its new angular momentum corresponds to a smaller orbit. Repeating this process many times, the gas element eventually falls down to the central object and forms an accretion disc.

1.4 Fluid Dynamical Aspects of an Accretion Flow

In this section, we briefly discuss various conservation laws of fluid dynamics. If the effective mean free path for particles l_{mf} is shorter than the accretion flow spatial length scale L:

$$l_{mf} \ll L \tag{1.21}$$

the accretion flow is hydrodynamical in nature and the system is regarded as a continuous flow characterized by a velocity $\mathbf{v}$, temperature T and density ρ. A continuum physical system is described by the laws of conservation of mass, momentum and energy. These conservation laws along with an equation of state explicitly describe the nature of the flow dynamics considering the appropriate boundary conditions.

The conservation of mass of the flow is described by the continuity equation for the density ρ and flow velocity $\mathbf{v}$ which is given by Landau and Lifshitz (1959)

$$\frac{\partial \rho}{\partial t} + \nabla.(\rho \mathbf{v}) = 0. \tag{1.22}$$

The momentum conservation is given by the *Navier-Stokes equation*:

$$\frac{\partial \mathbf{v}}{\partial t} + \mathbf{v}.\nabla \mathbf{v} = -\frac{1}{\rho}\nabla P + \mathbf{f}_{\mathbf{external}}, \tag{1.23}$$

where, P is the gas pressure at each point arising because of the thermal motion of the gas particles and $\mathbf{f}_{\mathbf{external}}$ denotes the external forces like gravity, viscosity, body forces, etc. Clearly, *Navier-Stokes equation* states that the rate of change of momentum per unit volume is caused by pressure, viscous and gravity forces. The energy equation for the gas element is given as

$$\frac{\partial}{\partial t}\left(\frac{1}{2}\rho v^2 + \rho\mathcal{E}\right) + \nabla.\left[\left(\frac{1}{2}\rho v^2 + \rho\mathcal{E} + P\right)\mathbf{v}\right] = \mathbf{f}.\mathbf{v} - \nabla.\mathbf{F}_{\mathbf{rad}} - \nabla.\mathbf{q}, \tag{1.24}$$

where, the terms ρv^2 and $\rho\mathcal{E}$ measure the kinetic energy density and internal energy density respectively. On the right-hand side, $\mathbf{F}_{\mathbf{rad}}$ represents the radiative flux vector and $\mathbf{q}$ denotes the conductive heat flux. In general, $\mathbf{q}$ estimates the rate of transport of thermal energy inside the gas due to random motions. Apart from these conservation laws, an equation of state is necessary to describe an astrophysical flow. For this purpose, the equation of state of a perfect gas is very useful, which is given as

$$P = \frac{\rho k T}{\mu m_p}, \tag{1.25}$$

where, k is the Boltzmann constant, m_p is the mass of the hydrogen atom and μ is the mean molecular weight for neutral hydrogen, $\mu = 1$ and for fully ionized hydrogen, $\mu = \frac{1}{2}$.

The important physical phenomena exhibited by these hyperbolic conservation laws is a shock. It is a genuinely nonlinear phenomenon in a flow. In the followig section, we look at the shocks, their origins and physical properties.

1.5 Shocks

A shock is a place where certain jumps in thermodynamic variables, such as pressure and temperature, take place. These develop spontaneously from smooth distributions and can remain stable. The shock jump is self-forming and also self-maintaining. This is unlike a contact discontinuity which must be put in the system initially and will not re-sharpen itself if it is smeared out by some other process. Some familiar examples of shock waves are the ‘sonic booms of a jet aircraft’, or the ‘bang from a gun’. These sounds are our perceptions of a sudden jump in air pressure. It is

convenient to define a shock in terms of Mach number. The Mach number is defined as the ratio of the flow velocity to the velocity of the sound. If the Mach number is less than unity, the flow is called subsonic and if it is greater than unity it is called supersonic. A flow is called transonic if it makes a transition from subsonic to supersonic flow or vice versa either continuously or discontinuously. The point of continuous transition is called the sonic point and the location of discontinuous transition is a shock. However, shocks and sonic points do not happen arbitrarily. Several conditions are to be fulfilled simultaneously. First, we discuss the conditions of shock formation (LL59).

1.5.1 Shock Conditions from Conservation Equations

Let us consider conservation of mass, momentum and energy (Eqs. 1.22, 1.23 and 1.24) for a gas in the conserved form

$$\frac{\delta \mathbf{U}}{\delta t} + \Delta \cdot \mathbf{F} = 0, \tag{1.26}$$

with conserved variables

$$\mathbf{U} = \begin{pmatrix} \rho \\ \rho \mathbf{v} \\ \rho(\frac{v^2}{2} + e) \end{pmatrix}, \tag{1.27}$$

and flux

$$F = \begin{pmatrix} \rho \mathbf{v} \\ \rho \mathbf{g} + \rho \mathbf{v} \otimes \mathbf{v} \\ \rho \mathbf{v}(\rho + \frac{v^2}{2} + \frac{p}{\rho}) \end{pmatrix}, \tag{1.28}$$

with $\mathbf{g} = \delta_{ij}$, a metric tensor that allows us to write the momentum flux density as a tensor. A discontinuity in a gas flow occurs over one or more surfaces, i.e. the quantities change discontinuously as we cross such a surface, which is called surface of discontinuity. Certain boundary conditions must be satisfied on surface of discontinuity.

Consider applying Gausss theorem to a short cylindrical volume at a stationary discontinuity with normal $\mathbf{n} = (0, 0, 1)$ in the z direction. This is equivalent to working in the frame moving with the discontinuity. Gausss law for any divergence

$$\int \Delta \cdot \mathbf{F} dV = \int_S F \cdot d\mathbf{A}. \tag{1.29}$$

Adjusting our volume so that it is a narrow slab and oriented with normal n

$$[\mathbf{F}\cdot\mathbf{n}] = (\mathbf{F_2} - \mathbf{F_1})\cdot\mathbf{n} = 0 \tag{1.30}$$

across a discontinuity (where [..] refer to quantities on one side subtracted by those on the other side).

First, the mass flux must be continuous, i.e. with $F = \rho\mathbf{v}$,

$$[\rho\mathbf{v}] = 0, \tag{1.31}$$

where, $\mathbf{v} = v_x\mathbf{i} + v_y\mathbf{j} + v_z\mathbf{k}$.

Second, the momentum flux must be continuous. The momentum flux per unit area is given by $\Pi_{ij} = pn_i + \rho v_i v_k n_k$, where, $\mathbf{n} = n_x\mathbf{i} + n_y\mathbf{j} + n_z\mathbf{k}$. Applying Gausss theorem to each component we have three equations (each one through surfaces with direction $\mathbf{n}$):

$$[\mathbf{\Pi}\cdot\mathbf{n}] = 0, \tag{1.32}$$

or, in a summation notation,

$$[\Pi_{ij}n_j] = 0, \tag{1.33}$$

or, orienting the shock normal along the z axis,

$$[\Pi_{xz}] = [\Pi_{yz}] = [\Pi_{zz}] = 0. \tag{1.34}$$

For each of these equations, the conservation of momentum implies

$$[p + \rho {v_x}^2] = 0, [\rho v_x v_y] = 0, [\rho v_x v_z] = 0, \tag{1.35}$$

while the second two equations (along with that for conservation of mass) imply that the velocity components parallel to the discontinuity do not change.

Third, the energy flux has to be continuous. The conservation of energy leads to the following shock condition:

$$\left[\rho\mathbf{v}\cdot\mathbf{n}\left(\frac{v^2}{2} + \frac{p}{\rho} + e\right)\right] = 0, \tag{1.36}$$

where, e = internal energy.

Equations 1.31, 1.35 and 1.36 represent a complete system of boundary conditions at a surface of discontinuity. There are two possibilities of two types of surface of discontinuity. The first type is that there is no mass flux through the surface. But this is not possible for an accretion flow around a black hole. So we consider the second type, i.e. where the mass flux is non-zero. In other words, $\rho v_{x_1} = \rho v_{x_2} \neq 0$, where, 1 and 2 represent quantities before and after the discontinuity. So, from Eq. 1.34, we

get $[\rho v_y = 0]$, $[\rho v_z = 0]$, i.e. the tangential velocity is continuous at the surface of discontinuity. So from Eqs. 1.35 and 1.36, we get

$$\left[\frac{1}{2}{v_x}^2 + \frac{p}{\rho} + e\right] = 0. \tag{1.37}$$

Thus, the following conditions of discontinuity must hold at the surface of discontinuity:

$$[\rho v_x] = 0, \left[p + \rho {v_x}^2\right] = 0, \left[\frac{1}{2}{v_x}^2 + \frac{p}{\rho} + e\right] = 0. \tag{1.38}$$

This kind of discontinuity of a flow is called a shock-wave or simply a shock. Equation 1.38 is called the normal Rankine-Hugoniot conditions and such a shock is termed as a Rankine-Hugoniot shock.

1.5.2 Relation Between the Pre-shock and the Post-shock Mach Numbers in an Adiabatic Case

In terms of the upstream Mach number, $M_1 = u_1/a_1$ (a_1 is upstream sound speed and so on), and using an equation of state with adiabatic index γ it is possible to show that

$$\frac{\rho_2}{\rho_1} = \frac{v_1}{v_2} = \frac{(\gamma+1){M_1}^2}{(\gamma-1){M_1}^2 + 2}, \tag{1.39}$$

and

$$\frac{p_1}{p_2} = \frac{2\gamma {M_1}^2}{(\gamma+1)} - \frac{(\gamma+1)}{(\gamma-1)}. \tag{1.40}$$

Also, the downstream Mach number (M_2) is given by

$${M_2}^2 = \frac{2 + (\gamma-1){M_1}^2}{2\gamma {M_1}^2 - (\gamma-1)}. \tag{1.41}$$

There are maximum density and velocity changes allowed across a shock jump that depends on the adiabatic index. Strong shocks are those in which $M_1 \to \infty$ giving

$$\frac{\rho_2}{\rho_1} = \frac{v_1}{v_2} \to \frac{(\gamma+1)}{(\gamma-1)}, \tag{1.42}$$

$$\frac{p_1}{p_2} \to \frac{2\gamma {M_1}^2}{(\gamma+1)} \tag{1.43}$$

For $\gamma = 5/3$ the density and velocity ratio is 4. This is the maximum value. A strong shock for a gas with $\gamma = 5/3$ can have a maximum density and velocity contrast across the shock of 4.

Now, using the relation

$$\gamma = 1 + \frac{1}{n}$$

in Eq. 1.41, we have

$$M_2{}^2 = \frac{M_1{}^2 + 2n}{2M_1{}^2(1+n) - 1}. \tag{1.44}$$

If $M_1 > 1$ then clearly,

$$2M_1{}^2 + 2M_1{}^2 n - 1 > M_1{}^2 + 2n \Rightarrow M_2 < 1, \tag{1.45}$$

as

$$2M_1{}^2 - 1 > 1, 2nM_1{}^2 > 2n. \tag{1.46}$$

So, for an adiabatic shock with constant γ the post-shock flow is subsonic.

Three different types of shocks are of special interest to us which correspond to three extreme physical considerations (Chakrabarti 1990a). These are: Rankine-Hugoniot shock, isentropic compression waves and isothermal shock.

1.5.3 Comments on Entropy

We note that we could look at $p/\rho^\gamma = K$ where, K is the coefficient in $P = K\rho^\gamma$, on both sides of the shock. The ratio

$$\frac{p_1 \rho_1{}^{-1}}{p_2 \rho_2{}^{-1}} \tag{1.47}$$

is not in general equal to 1. This means that K is not the same on both sides of the shock and that entropy is not conserved across a shock. The gas jumps from one adiabat to another of higher entropy. It may be puzzling to consider that we have specified an equation of state on either side of the shock that implies that variations are adiabatic. While we have assumed that $p \propto \rho^\gamma$ on either side of the shock and with the same γ, we have not specified that the constant K is the same on either side of the discontinuity. Since the entropy cannot decrease across a shock, entropy must be generated at the shock. Dissipation from viscosity and turbulence dictate the shape of the actual shock interface on small scales (Chakrabarti 1990a).

1.5.4 Rankine-Hugoniot Shocks, Isentropic Compression Waves and Isothermal Shocks

A Rankine-Hugoniot shock is a dissipation-less shock where there is an increase in entropy. The velocity jumps from the supersonic to the subsonic value and the post-shock temperature is high. Thus the sound speed and the thickness of the flow increases after the shock. In case of an isentropic compression wave, the entropy does not change in the flow but a considerable part of the energy is lost at the shock. The amount of entropy at the shock front is comparable to the entropy radiated away from the disc which may help to maintain a proper balance of entropy. After a shock front the gas is heated but this gas may cool in some cases back to its original temperature. If the cooling length is short then we call the shock isothermal (Chakrabarti 1990a).

We can summarize three types of jumps (Chakrabarti 1990a). Let $(\mathcal{E}_-, \mathcal{E}_+)$, (T_-, T_+) and (s_-, s_+) be energies, temperatures and entropies of the flow, where the subscripts '$-$' and '$+$' denote the quantities before and after the shock. Then, for the Rankine-Huginiot shock,

$$\mathcal{E}_- = \mathcal{E}_+, T_- < T_+, s_- < s_+. \tag{1.48}$$

For the isentropic compression wave,

$$\mathcal{E}_- < \mathcal{E}_+, T_- < T_+, s_- = s_+. \tag{1.49}$$

For the isothermal shock,

$$\mathcal{E}_- < \mathcal{E}_+, T_- = T_+, s_- > s_+. \tag{1.50}$$

Shocks in accretion flows (Chakrabarti 1989) are also an important phenomenon which influence the geometry as well as the radiations emitted from the flow. We will discuss this in Sect. 1.5.5.

1.5.5 Shocks in Accretion Flows (Chakrabarti 1989)

The rotating matter accreting around a black hole experiences mainly two forces which dictate the motion of the particle trajectories. The first is the inward gravitational force, $F_g = \frac{1}{r^2}$ and the second is the outward centrifugal force, $F_{\rm cen} = \frac{1}{r^3}$ for a flow having constant angular momentum. Both the principal forces strictly depend on the radial distance. Therefore, the gravity dominates over the centrifugal force at a distance either close to or far away from the black hole, whereas the centrifugal force becomes comparable to gravity at intermediate locations. Accordingly, matter at infinity feels the gravitational pull due to the black hole and accretes towards it with increasing inward velocity which becomes supersonic at some point. The incoming

matter is piled up behind the centrifugal barrier. At a distance of a few tens of r_g the outward centrifugal force starts to dominate over gravity and thus the matter slows down. Therefore, the density goes up and matter makes a discontinuous transition from a supersonic branch to the subsonic branch which is termed as a shock. Just after the shock, the subsonic matter is again attracted towards the black hole due to gravity and crosses the inner sonic point to become supersonic before crossing the black hole horizon (Chakrabarti 1989, 1996).

1.6 Importance of Numerical Simulations in Astrophysics

An wide range of astrophysical phenomena are described by time-dependent flow dynamical equations. If we want to seek the time evolution of the accretion phenomena, we need to solve numerically the time-dependent equations since analytical solutions are prohibitive in most cases. Hydrodynamic properties of matter can be derived from basic flow equations such as the continuity, momentum and energy equations. The flow equations consist of partial differential equations. These are replaced by finite difference equations for simplified geometries and are numerically solved with sufficient boundary conditions when the initial conditions are properly specified. A number of numerical methods to solve the fluid equations have been developed so far. The general requirement is that the obtained solutions must be stable, should be computationally stable and the conserved quantities should remain conserved. Some numerical methods may have more advantages than others in satisfying these requirements. So we need to select the most efficient numerical method for solving a specific problem.

In the case of accretion flows around black holes, the system of equations reduces the problem to a boundary value problem. The initial conditions are assumed to be fixed and the boundary condition for the black holes is that the flow velocity of matter is the same as the velocity of light on the horizon. However, it is impossible to solve all the equations simultaneously (momentum equations, continuity equation and energy equation) in an analytical way. So, we use a numerical method to solve these equations. However, in order to trust the results of a numerical simulation, one must have a thorough knowledge of the analytical solutions and, if possible, the numerical solutions are to be validated with known analytical solutions, wherever available.

1.7 An Overview of Steady Accretion Flow Models: Analytical Aspects

There are several accretion and wind solutions in the literature, but their applicability is restricted. To describe a black hole accretion, several quantities are important: specific energy (ϵ), specific angular momentum (λ), viscous stress, etc. A mass

accretion rate ($\dot{M}$) is also needed. Some models use two mass accretion rates, one for the Keplerian disc and the other for the sub-Keplerian disc.

Historically, the study of the interaction of a spherical gravitating star moving supersonically with respect to a uniform medium started with the pioneering work of Hoyle and Lyttleton (1939) and Bondi and Hoyle (1944). The problem was to quantify the amount of matter which was accumulated on the star surface while coming from the interstellar medium. The result was not complete as the gas pressure was ignored. Several years later Bondi (1952) published his pioneering work on the spherical accretion process. This solution was later applied by Parker (1959) to explain winds emerging from the sun.

1.7.1 Spherical Accretion: Bondi Flow

The study of modern accretion processes on stars and compact objects began with the revolutionary work on spherical flows onto normal stars by Bondi (1952). The objects named 'black holes' were unknown (at least in the context of astrophysical object) at the time of the publication of this paper. Bondi considered the situation where an isolated star was at rest inside an ambient medium and the matter was accreted onto the star's surface spherically symmetrically due to gravitational attraction. To treat the problem mathematically, one can take spherical polar coordinates (r, θ, ϕ) with the origin at the centre of the star. The flow variables are independent of θ and ϕ due to spherical symmetry. The gas velocity has only a radial component $v_r = v$. We consider radial flows near a central Newtonian star with mass M. Parameters describing the flow are the density and sound speeds at infinity ρ_∞ and a_∞, and the mass of the central object, M. It can also be subsonic throughout, depending on the boundary condition. It is instructive to revisit the Bondi solution briefly as presented by Chakrabarti (1990a).

We consider a spherically symmetric radial flow on a central star having mass M. The motion of the gas is assumed to be steady and the flow has no magnetic field. The increase in the mass of the central star is neglected and thus the external force field remains unchanged. In spherical coordinates, the mass conservation equation becomes

$$\frac{\partial \rho}{\partial t} + \frac{1}{r^2}\frac{\mathrm{d}}{\mathrm{d}r}\left(\rho v r^2\right) = 0. \tag{1.51}$$

For a steady flow, we can set $\frac{\partial}{\partial t} = 0$. Then we have

$$\frac{1}{r^2}\frac{\mathrm{d}}{\mathrm{d}r}\left(\rho v r^2\right) = 0. \tag{1.52}$$

We integrate the previous equation to obtain the constant outflow or inflow rate

$$4\pi\rho v r^2 = \dot{M}, \tag{1.53}$$

where, $\dot{M}$ is known as the accretion rate. Equation 1.52 may also written as

$$\rho v r^2 = \dot{m}, \tag{1.54}$$

where, $\dot{m} = \frac{\dot{M}}{4\pi}$. The equation of motion of the accreting matter of unit mass in the steady-state condition is obtained from Euler equation where the only contribution to the external force, f_{external}, is from gravity. Due to spherical symmetry and steady-state condition the Euler equation becomes

$$v\frac{\mathrm{d}v}{\mathrm{d}r} + \frac{1}{\rho}\frac{\mathrm{d}P}{\mathrm{d}r} + \frac{1}{r^2} = 0. \tag{1.55}$$

In these equations, we have chosen the geometric units $G = c = M = 1$ where G is the gravitational constant, c is the velocity of light. Hence, the unit of length, mass, velocity and time would be GM/c^2, M, c and GM/c^3 respectively. Moreover, the matter is considered to be adiabatic in nature that follows from the equation of state $P = K\rho^\gamma$ where K is a constant which measures the specific entropy of the matter and γ is the adiabatic index. We integrate radial momentum equation using adiabatic sound speed, $a^2 = \gamma P/\rho$, to obtain the *Bernoulli integral* which is given as

$$\mathcal{E} = \frac{1}{2}v^2 + na^2 - \frac{1}{r} = na_\infty^2, \tag{1.56}$$

where, $\mathcal{E}$ and n $(= \frac{1}{\gamma-1})$ are the specific energy and polytropic index of the flow respectively.

One can re-express the polytropic equation of state in terms of adiabatic sound speed as

$$\rho = \left(\frac{a^2}{\gamma K}\right)^n. \tag{1.57}$$

Using the expression for ρ, Eq. 1.44 can be written as

$$\dot{\mathcal{M}} = a^{2n} v r^2. \tag{1.58}$$

The new term $\dot{\mathcal{M}} = \gamma^n K^n \dot{m}$ first introduced by Chakrabarti (1989) is also a conserved quantity in the flow known as *entropy accretion rate*. Chakrabarti (1989, 1990a) introduced a clever method of calculating the location of the sonic point (r_c) and the value of radial derivative of velocity ($\frac{\mathrm{d}v_r}{\mathrm{d}r}$) at $r = r_c$.

Differentiating Eqs. 1.56 and 1.58 and eliminating da/dr we get the gradient of radial velocity

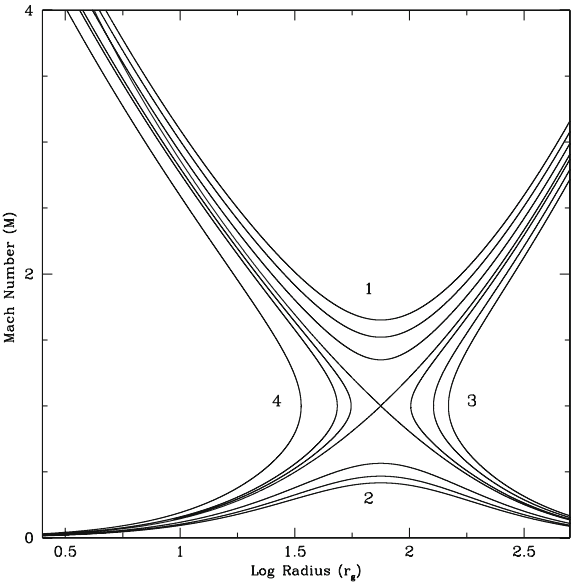

Fig. 1.3 Plot of Mach number (M) versus radius (Log scale) of a Bondi flow around a Newtonian star for $n = 3$ and $\mathcal{E} = 0.01$. The transonic flows in accretion and outflows are shown. This solution was given byBondi (1952). We have replotted this solution. The curves from the regions marked 1, 2, 3 and 4 are not transonic. Among them, branch-2 is subsonic at every point and can also be a solution on a star. Branch-4 is supersonic always and could be excluded as unrealistic

$$\frac{\mathrm{d}v}{\mathrm{d}r} = \frac{\dfrac{2a^2}{r} - \dfrac{1}{r^2}}{v - \dfrac{a^2}{v}} = \frac{N}{D}, \tag{1.59}$$

where, N and D stand for numerator and denominator respectively.

A flow with a constant energy and entropy must be smooth at every point. Thus, if at some point the denominator vanishes, the numerator must also vanish there as $\mathrm{d}v/\mathrm{d}r$ has to be finite. Such a special point is called the critical point of the flow. We therefore have the critical point condition given as

$$v_c^2 = a_c^2 = \frac{1}{2r_c}. \tag{1.60}$$

The subscript 'c' denotes the flow variables at the critical point. The Mach number, defined as the ratio of the flow radial velocity to the sound speed, is unity at the critical point: $M(r_c)(= v_c/a_c) = 1$. Therefore, the critical points are renamed as the sonic points (r_c). This sonic point, r_c, would then correspond to a spherical surface called the sound horizon. This name is particularly suited since any acoustic disturbance created at the downstream region ($r < r_c, u < a$) will not be carried out to the upstream ($r > r_c, u > a$).

Let us concentrate on the length scale of the accretion flow problem. Define the 'accretion radius', r_{acc} as the radius at which the kinetic energy of matter is balanced by its potential energy and is given as

$$r_{\rm acc} = \frac{2}{v_\infty^2}. \tag{1.61}$$

This length scale gives the range of influence of the central star onto the gas cloud. From the previous expression, it is clear that for $r \to \infty$, contribution of gravity is negligible and the flow does not feel any inward pull. But at the same location, the sound speed has some non-zero value which asymptotically approaches to a_∞. As one now proceeds towards the central star, the flow velocity increases and the flow must be subsonic at a large r. In the accretion process, the gradient of the radial velocity must always be negative throughout the flow. In the vicinity of the accreting star, the gravity dominates over all other forces. This makes the numerator negative. Therefore, accretion is possible if and only if $D > 0$ this implies $v > a$, i.e., the flow is supersonic in nature at that region. Thus the accretion flow solutions are always transonic and transonic transition between sub- and supersonic branches occur at the sonic point. This is not true for the Neutron star accretion where the whole accretion could be subsonic. Limitation of the transonic flow solution can be clearly understood when the flow variable (u or a) at the critical points is expressed in terms of a_∞ and is given as

$$a_c = \left(\frac{n}{n-3/2}\right)^{1/2} a_\infty. \tag{1.62}$$

This indicates that the transonic flow exists if and only if $n > 3/2$ i.e., for $\gamma < 5/3$.

More importantly, the conserved quantities $\mathcal{E}$ and $\dot{\mathcal{M}}$ could be expressed in terms of an unknown variable, r_c using two critical point conditions. This implies that $\mathcal{E}$ and $\dot{\mathcal{M}}$ cannot be independent and this would provide a single parameter family of solutions. The entropy accretion rate $\dot{\mathcal{M}}$ can be estimated from a_∞ as

$$\dot{\mathcal{M}}_c = \frac{1}{4}\left(\frac{n a_\infty}{n-3/2}\right)^{n-3/2}. \tag{1.63}$$

The nature of the Bondi solutions needs a detailed study of radial velocity gradient $[(\mathrm{d}v/\mathrm{d}r)_c]$ at the critical point. At this point, $\mathrm{d}v/\mathrm{d}r = 0/0$, so one must apply L'Hospital rule to understand the behavior of the flow properly. Thus using the critical point conditions at r_c one obtains

$$(\mathrm{d}v/\mathrm{d}r)_c = -\frac{4a_c^3}{2n+1}[1 \mp \sqrt{n(n-3/2)}]. \tag{1.64}$$

The nature of the critical points is dictated by the discriminant $\mathcal{D} = n(n-3/2)$. A transonic flow solution is possible when velocity gradient at the critical point becomes real and it happens for $n > 3/2$. Classification of the critical points mainly depends on the exact value of the discriminant ($\mathcal{D}$) and Chakrabarti (1990a) has done a detailed study on it, which will not be repeated here. For $n > 2$, a saddle type sonic point exists since derivatives $(\mathrm{d}v/\mathrm{d}r)_c$ at the critical point are real and of opposite signs. When $n < 3/2$, $\mathcal{D} < 0$ and the critical point are of spiral type, critical point

becomes nodal when n lies in the range $2 > n > 3/2$. Thus, in a Bondi flow, the behaviour of the critical point strongly depends on polytropic index (n) and its nature is highly sensitive to the numerical value of n.

In Fig. 1.3, we replot the Bondi solution and present the variation of Mach number with the logarithmic radial distance for a set of fixed input parameters $n = 3$ and $\mathcal{E} = 0.01$. The solid curves connect the flow solution from infinity to the star surface and hence are considered to be physically significant. Details of the figure description are shown in the caption.

1.7.2 Approaches to Disc-Type Solutions

In 1963, the first quasar QSO 3C273 was discovered (Hazard et al. 1963; Schmidt 1963). Various explanations were proposed and it was generally felt that the enormous energy radiated by a QSO must be gravitational in nature. The computed luminosity was found to be of the order of 10^{47} ergs per sec for reasonable parameters.

Using the Schwarzschild solution Salpeter (1964) explained that luminosity could be due to Bondi accretion on very massive compact objects ($>10\,M_{\odot}$). Originally these objects were called 'collapsars'. Later the phrase 'black hole' was coined by (Wheeler 1968). Lynden-Bell (1969) argued that the accretion close to the Eddington rate on supermassive black holes must be responsible for this tremendous activity. Some efforts were made to compute spherically symmetric Bondi accretion in the presence of heating and cooling terms. Shapiro (1973a) included electron–electron and electron–proton bremsstrahlung effects. Schvartsman (1971a), Zel'dovich and Novikov (1973) and Shapiro (1973b) included effects of tangled magnetic field with equipartition energy density. They found that the synchrotron radiation will be predominantly emitted in the infrared region. The effect of pre-heating on the luminosity of the spherical emission was established by Ostriker et al. (1976). The boundary layer of a neutron star where the flow settles down to zero velocity was first studied by Shapiro and Salpeter (1975). Thus the importance of the inner boundary condition was recognized, and it was particularly realised that the boundary layer is an extension of the disc flow itself. This concept was extended even for black holes by Chakrabarti (1996), even when there was no hard surface. This is simply because matter with angular momentum stays away from the black hole due to centrifugal force and the centrifugal barrier behaves like a hard surface.

The simple spherical flow was very soon improved upon by adding an angular momentum. Numerical integration of the non-relativistic fluid equations performed by Hunt (1973) for the case of gravitating point source moving through the adiabatic gas for different Mach numbers. Hunt found that in the case of a supersonic flow, the source was preceded by the bow shock with an accretion rate comparable to the classical value obtained by Bondi and Hoyle (1944).

1.7.3 The Standard Disc Model

The so-called 'standard Keplerian disc' was then proposed by Shakura and Sunyaev (1973). For a disc in nearly circular motion around a star or black hole, they expected that v_ϕ, the component of the velocity in the tangential direction to be large compared to a small radial component v_r. They also assumed that the disc is thin and integrated physical quantities vertically. The paper (Shakura and Sunyaev 1973) made a simple assumption that let all the matter move in Keplerian orbits inside the disc, even when the disc has pressure and inertial forces and close to a black hole and even when the viscosity is small. The inner edge of the disc was truncated at $\frac{6GM}{c^2}$, i.e. 3 Schwarzschild radii for a non-rotating black hole. Here, G, M and c are the gravitational constant, the mass of the black hole and the velocity of light respectively. The angular momentum was transported outward by viscous processes. It was also assumed that the heat generated by viscosity was assumed to be radiated away instantaneously from the surface. The viscous stress was assumed to be dominated by the $W_{r\phi}$ component and the viscous stress is considered to be proportional to the local pressure by the relation $W_{r\phi} = -\alpha\rho {v_s}^2$, where α is a constant, ρ is density and v_s is the isothermal sound velocity. For causality, $\alpha < 1$ always. The disc was assumed to be in vertical equilibrium. The above work was carried out using Newtonian equations.

One can estimate the energy dissipation rate for the Keplerian accretion disc. The energy per unit area dissipated per unit time would be

$$Q(R) = \eta \Sigma^2 R^2 (\frac{\mathrm{d}\Omega}{\mathrm{d}R})^2. \tag{1.65}$$

We can evaluate this for a steadily accreting Keplerian disc using

$$\frac{\mathrm{d}\Omega}{\mathrm{d}R} = -\frac{3}{2}(\frac{\Omega}{R}). \tag{1.66}$$

After some simple algebra, for the steady-state disc, the energy flux, radiated from unit surface area of the disc per unit time at a radius R can be written as

$$Q(R) = \frac{3}{8\pi}\dot{M}\frac{GM}{R^3}\left[1 - \left(\frac{R_0}{R}\right)^{1/2}\right], \tag{1.67}$$

Consider Eq. 1.67 for the energy dissipated per unit area for a nearly Keplerian system in steady state. This viscously dissipated energy escapes as radiation from the top and bottom of the disc. Let us integrate between inner and outer disc radii $(R_{\mathrm{in}}, R_{\mathrm{out}})$ to estimate the total luminosity of the disc due to accretion

$$L(R_{\mathrm{in}}, R_{\mathrm{out}}) = \int_{R_{\mathrm{in}}}^{R_{\mathrm{out}}} 2\pi R Q(R) \mathrm{d}R \tag{1.68}$$

After completing the algebra, for a Keplerian system accreting in a steady state with an accretion rate $\dot{M}$, the corresponding luminosity produced by the disc in between $R_{\rm in}$ and $R_{\rm out}$ is given as

$$L(R_{\rm in}, R_{\rm out}) = \frac{3GM\dot{M}}{2}\left[\frac{1}{R_{\rm in}}\left[1-\frac{2}{3}\left(\frac{R_0}{R_{\rm in}}\right)^{1/2}\right]-\frac{1}{R_{\rm out}}\left[1-\frac{2}{3}\left(\frac{R_0}{R_{\rm out}}\right)^{1/2}\right]\right]. \tag{1.69}$$

For $R_{\rm in} = R_0$ (the radius of the central star or the Schwarzschild radius) and $R_2 = \infty$ the total luminosity radiated from the accretion disc becomes

$$L_{\rm disc} = \frac{GM\dot{M}}{2R_0}. \tag{1.70}$$

So, half the gravitational energy is radiated away from the accretion disc.

To compute the temperature and density structure of a disc, the opacity as a function of depth and wavelength must be taken into account. In case the Shakura-Sunyaev disc is optically thick and opacity due to free-free absorption is more important than the opacity due to scattering, each element of the disc surface radiates black body spectrum with surface temperature $T(R)$ given by equating the dissipation rate to the black body flux

$$T(R) \approx 5\times 10^7\left(\frac{M}{M_\odot}\right)^{-1/2}\dot{M}_{17}^{1/4}(2R)^{-3/4}\left(1-\sqrt{\frac{3}{R}}\right)^{1/4} K. \tag{1.71}$$

In this equation M is measured in units of $M_\odot$, $\dot{M}_{17}$ is in units of 10^{17} g s^{-1} and R is measured in units of $2GMM_\odot/c^2$.

This disc is radiatively very efficient. However, the disc is terminated at the last stable circular orbit. The effective temperature of the radiation is around $\sim$1 keV for stellar black holes ($M \sim 10M_\odot$). For Quasars, the radiation emitted from such a disc is in the ultraviolet region and is widely known to produce the big blue bump. This disc is an ideal solution, as it assumes the angular momentum distribution to be predetermined (Keplerian λ_K) and it has no solution below $r = 3r_g$. The gas pressure is assumed to be negligible. This model is unable to explain the observed emission features of accreting black holes at energies higher than 10 keV.

Novikov and Thorne (1973) almost simultaneously completed this work to include general relativity. Soon after the standard disc model was published Lightman and Eardley (1974) pointed out that in a radiation pressure dominated region, viscosity prescription of Shakura and Sunyaev was inconsistent if α remains constant and the disc might break into thin rings. Eardley et al. (1975) had a very successful model with a Keplerian disc which flares into a thick disc closer to the inner edge. They considered a two-temperature flow and it was a single component disc with a small accretion rate. Pringle (1976) showed that such a disc is thermally unstable.

1.7.4 Thick Accretion Discs

Lynden-Bell (1978) first computed the steady-state structure of a flow with a constant angular momentum in general relativistic flows and predicted that the flow would develop giant vortices along the axis, since the centrifugal force would keep matter away from the axis. He also found that discs thicken up closer to the black hole. These models were later developed to produce thick accretion disc models. The work of Lynden-Bell was extended and thick accretion disc models were constructed by Paczyński and his collaborators (Kozlowski et al. 1978; Abramowicz et al. 1978;) by choosing various combinations of angular momentum distribution. Abramowicz et al. (1978) and Kozlowski et al. (1978) showed that a cusp exists at the inner edge of the discs and the fat disc can be constructed whose inner edges extend down to the marginally bound circular orbit, r_{mb} ($r_{mb} = 4\,GM/c^2$ for a Schwarzschild black hole).

In (Paczyński and Wiita 1980) discovered a modified Newtonian potential which we mentioned earlier. They (PW) were able to construct thick discs whose inner radii lie within $r_{ms} = (6\,GM/c^2)$ and match onto more standard thin discs. They also showed that accretion can exceed the nominal critical rates and because of the bloated shape of their discs, the total luminosities can exceed the nominal Eddington luminosity. The first prescription of how the angular momentum should be distributed in a general relativistic thick accretion disc was given by Chakrabarti (1985). The Chakrabarti distribution makes use of the properties of the constant angular momentum surfaces (which are also angular constant velocity surfaces for barotropic flows) called von-Zeipel cylinders. The solution of Chakrabarti (1985) is valid for any axisymmetric space-time, including the Kerr geometry.

1.7.5 Advective Discs

After the discovery of the pseudo-Newtonian potential (PW80), the transonic accretion flow with angular momentum onto a black hole was investigated by Liang and Thompson (1980), Abramowicz and Zurek (1981), Loska (1982), Muchotrzeb (1983), Matsumoto et al. (1984) and Abramowicz (1985). Using the Paczyński-Wiita potential Liang and Thompson (1980) argued that unlike a Bondi flow, a thin, rotating, adiabatic flow can have three sonic points, two of saddle type and one of centre type. It was noticed by Abramowicz and Zurek (1981) that there exist two transonic solutions with the same specific energy and the same specific angular momentum but with two different sonic points. They argued that the disc could go back and forth from one solution to the other. Chakrabarti (1989) showed that this is not possible, since the entropy has to go up and down, which is impossible. It is well known in the context of solar winds that if the flow has more than one saddle-type sonic point, shocks may form (Holzer and Axford 1970). Chang and Ostriker (1985) found necessary conditions for the existence of solutions with two sonic points when the gas is

pre-heated and pointed out that these would often be satisfied in astrophysical environments. They showed that the presence of pre-heating in a spherical flow would increase the number of sonic points and shocks could form.

Meanwhile, important work on sub-Keplerian flows around black holes started. In the late 1980s and early 1990s, improvements in space-borne (satellite) and ground-based (radio antennas) instruments triggered the challenge to explain the observed X-ray spectra of the black hole binaries. In the low energy ranges (<10 keV), the spectrum was modelled as a black body spectrum but at high energies (few 100 keV) there was a power-law behaviour whose slope changed from time to time. The standard disc and the thick-disc both were unable to reproduce the hard component (high energy) of the spectrum which extend up to 100 keV and beyond. To explain this, the presence of a hot ($T_e \sim 10^9$ K), optically thin plasma was required. At the same time, an interesting feature called quasi-periodic oscillations (QPOs) was also observed in most of the galactic black hole candidates. It was found that the X-ray variabilities are quasi-periodic in nature and their Fourier decomposition shows a prominent peak in the power density spectrum (PDS). The radio observations confirmed that the jets and outflows that are observed in GBHs come out from the vicinity of the hole. To explain the above features, a complete accretion disc model was needed instead of different models to explain different observations.

Self-consistent studies of the accretion disc problem were started in the late 1980s by Chakrabarti and his collaborators. In Chakrabarti (1989) presented a global solution for the astrophysical flow (will refer hereafter as the 'Chakrabarti solution'). According to Chakrabarti's approach, the various properties of astrophysical flows can be understood through a systematic study of the basic flow equations which contain both the radial and azimuthal components of the velocity. These solutions are perfectly stable and the global solutions seem to exist even without any viscosity. This was because for a black hole accretion, the gravity eventually wins and allows matter to sink in even with a constant angular momentum. The study of shock waves in accretion discs also turned out to be important in black hole astrophysics. The shocks in accretion discs are essential to explain many observable phenomenon. Non-dissipative accretion discs around a black hole could be modelled in different ways depending on the flow geometry. In the astrophysical literature, three models, namely Conical model, Constant Height model and Vertical Equilibrium model (Chakrabarti 1990a) are mostly considered. An advective accretion disc is the one that advects, or carries 'something', namely mass, entropy, energy, etc. This means an advective disc should have a significant radial velocity which may even reach the velocity of light on the horizon. Therefore, before entering into a black hole, matter had to be supersonic (i.e., Mach number, $M_a = v/a > 1$, where v and a are radial velocity and sound speed respectively). As $v \sim 0$ at infinity, the matter must pass through at least one sonic point ($M_a = 1$), and as a sub-Keplerian flow (i.e., a flow with specific angular momentum $\lambda < \lambda_K$, the Keplerian angular momentum). Close to the black hole, the matter falls very rapidly towards the horizon, thus making $\lambda \sim$ constant. One of the consequences of existence of multiple sonic points is that the flow accreting through the outer sonic point can be slowed down by the centrifugal barrier. This slowed down matter acts as a barrier to the faster fluid following it. If

the strength of the barrier is strong enough then the shocks may form Chakrabarti (1989) whose properties vary systematically as the flow parameters are changed. For a large region of the parameter space (Chakrabarti 1990a), a stable solution can have a standing shock wave. Depending on the physical parameters, a shock may be steady or oscillating in nature, and it may even be absent. The oscillations of the shock may give rise to the temporal variability in the form of QPOs which are observed in many of the BH candidates. In this 'boundary layer', the flow kinetic energy is converted into the thermal energy forming a hot Compton cloud which can inverse-Comptonize the soft photons into hard photons and produce outflows and winds (Chakrabarti 1999). This boundary layer is called the CENtrifugal pressure supported BOundary Layer (or, CENBOL).

In the 1990s, the transonic flow model of the accretion was perfected after the inclusions of heating, cooling, viscosity, etc. This paradigm is called the *Advective Disc Paradigm*. Here the goal was to achieve a single paradigm so that the varied observations from black hole candidates could be explained within a single framework. The Advective Disc Paradigm appears to be the closest to reality as most of the observations could be explained by using one or the other predictions of this paradigm. A cartoon diagram is shown in Fig. 1.4.

1.7.6 Two Component Advective Flows

Chakrabarti and Titarchuk (1995), based on the solutions of viscous and inviscid transonic flows around black holes (Chakrabarti 1989, 1990a, b) proposed that, in general, the accretion disc should really have two components: a Keplerian accretion on the equatorial plane and a sub-Keplerian halo which surrounds the Keplerian disc, and the puffed up post-shock region of the flow should act as the Compton cloud. So, Two Component Advective Flow (TCAF) (Fig. 1.5) is a combination of two types of flows: a highly viscous Keplerian component which is accreted in long, viscous timescale and a initially sub-Keplerian component, with higher radial velocity and lower angular momentum. The sub-Keplerian flow is accreted in the short, free-fall

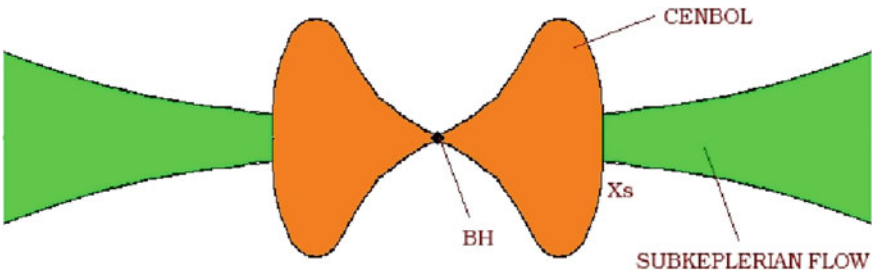

Fig. 1.4 Geometry of an advective disc around a *black hole*. We draw this cartoon diagram for sub-Keplerian flow

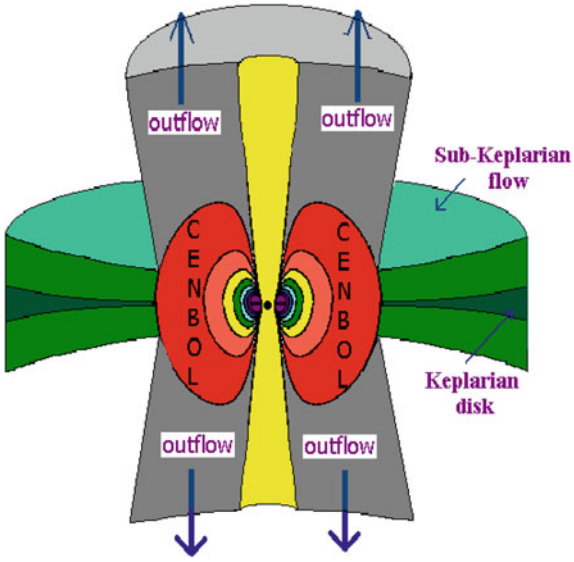

Fig. 1.5 Cartoon diagram of a Two-Component Advective Flow (TCAF) around *black holes* which shows the disc-outflows connection (diagram has been taken from Dr. Samir Mandal's Ph.D thesis 2005)

timescale. The Keplerian disc, because of its low energy, resides at the equatorial plane, while matter with lower angular momentum flows above and below it. The wind is predominantly produced from the post-shock (CENBOL) area. A transient shock can also be present just outside the inner sonic point. The inner edge of the Keplerian disc is terminated at the shock location. The amount of matter inside the jet and outflow vary due to the shock-oscillation.

In the above discussions, we have concentrated on the theoretical models of accretion flows. Basically they describe the stationary properties of an accretion disc. Some of the theoretical models of the accretion disc which we discussed in the past have been put to rigorous tests of numerical simulation. In Chap. 2, we present some important developments in numerical simulation in this direction in the last three decades. After that we present the goal of my thesis.

References

Abramowicz, M. A. (1985), *PASJ, 37*, 727.
Abramowicz, M., Jaroszynski, M., & Sikora, M. (1978). *Journal of Astrophysics & Astronomy*, *63*, 221.
Abramowicz, M., & Zurek, W. H. (1981). *The Astrophysical Journal*, *246*, 314.
Bondi, H. & Hoyle, F. (1944). *MNRAS*, *104*, 273.
Bondi, H. (1952). *MNRAS*, *112*, 195.
Chakrabarti, S. K. & Titarchuk, L. G. (1995). *The Astrophysical Journal*, *455*, 623.
Chakrabarti, S. K. (1989). *The Astrophysical Journal*, *347*, 365.
Chakrabarti, S. K. (1990a). *Theory of transonic astrophysical flows* Singapore: World Scientific.

Chakrabarti, S. K. (1990b). *MNRAS*, *243*, 610.
Chakrabarti, S. K. (1996). *Physics Reports*, *266*, 229.
Chakrabarti, S. K. (1985). *The Astrophysical Journal*, *294*, 383.
Chang, K. M., & Ostriker, J. P. (1985). *The Astrophysical Journal*, *288*, 428.
Chattopadhyay, I. (2003). *Ph.D. Thesis*. Kolkata: Jadavpur University.
Eardley, D. M., Lightman, A. P., & Shapiro, S. L. (1975). *The Astrophysical Journal*, *199*, 153.
Hazard, C., Mackay, M. B., & Shimmins, A. J. (1963). *Nature*, *197*, 1037.
Holzer, T. E., & Axford, W. I. (1970). *The Annual Review of Astronomy and Astrophysics*, *8*, 31.
Hoyle, F., & Lyttleton, R. A. (1939). *The Cambridge Philosophical Society*, *39*, 592.
Hunt, B.G. (1973). *JATP, 35*, 1755.
Kozlowski, M., Jaroszynski, M., & Abramowicz, M. A. (1978). *Acta Astronomica*, *63*, 209.
Landau, L. D., & Lifshitz , E. M. (1959). Fluid Mechanics. Oxford: Pergamon Press.
Liang, E. P. T., & Thompson, K. A. (1980). *The Astrophysical Journal*, *240*, 271.
Lightman, A. P., & Eardley, D. M. (1974). *The Astrophysical Journal*, *187*, 1.
Loska, Z. (1982). *Acta Astronomica*, *33*, 79.
Lynden-Bell, D. (1969). *Nature*, *223*, 690.
Lynden-Bell, D. (1978). *Phys. Scri.*, *17*, 185.
Matsumoto, R., Kato, S., Fukue, J., & Okazaki, A. T. (1984). *Publications of the Astronomical Society of Japan*, *36*, 71.
Muchotrzeb, B. (1983). *Acta Astronomica*, *32*, 13.
Novikov, I. & Thorne, K. S. (1973). In: C. DeWitt & B. DeWitt (Eds.), *Black Holes* (pp. 343) New York: Gordon and Breach.
Ostriker, J. P., McCray, R., Weaver, R., & Yahil, A. (1976). *The Astrophysical Journal*, *208*, 61.
Paczyński, B. & Wiita, P. J. (1980). *Astronomy and Astrophysics* , *88*, 23.
Parker, E. N. (1959). *The Astrophysical Journal*, *129*, 217.
Pringle, J. (1976). *MNRAS*, *177*, 65.
Salpeter, E. (1964). *The Astrophysical Journal*, *140*, 796.
Schmidt, M. (1963). *Nature*, *197*, 1040.
Schvartsman, V F Sh. (1971a). *Soviet Astronomy*, *15*, 342.
Shakura, N. I. & Sunyaev, R. A. (1973). *Astronomy & Astrophysics*, *24*, 337.
Shapiro, S. L. (1973a). *The Astrophysical Journal*, *180*, 531.
Shapiro, S. L. (1973b). *The Astrophysical Journal*, *185*, 69.
Shapiro, S. L., & Salpeter, E. (1975). *The Astrophysical Journal*, *198*, 671.
Wheeler, J. A. (1968). *American Scientist*, *56*, 1.
Zel'dovich, Ya. B., & Novikov, I.D. (1973). Relativistic astrophysics: Stars and relativity (Vol. 1). Chicago: University of Chicago Press.

Chapter 2
Overview of Numerical Simulations on Accretion Processes and Our Objectives

Abstract We give an overview of the past work done on numerical simulation for accretion flows around black holes. We start with non-viscous cases. We also point out some important simulations of viscous accretion discs. In the last section of this chapter, we present the precise goals for this thesis work.

2.1 Introduction

We turn now to present an overview of various simulations in astrophysics using numerical methods to solve the basic conservation equations. Numerical simulations of fluid flows in the vicinity of strongly gravitating compact objects require a three-dimensional description because of their complex nature and lack of symmetry. To provide a physical basis for the interpretative framework that the source is accretion driven, a detailed description of the relevant hydrodynamical (and radiative) process is required. One of the most convincing ways to study whether a solution is stable or not is to perform time-dependent numerical simulations.

Prendergast (1960) was the first to carry out numerical simulation of gaseous flows, while ignoring the pressure. His model expressed two constituent stars as two mass points and ignored either release or accretion of the gas (see also, Huang 1965, 1966). These drawbacks were corrected by Prendergast and Taam (1974), who used the beam scheme and with mass-accreting star of large size, were unable to find the formation of any accretion disc. Biermann (1971) conducted simulations by the characteristic line method for models close to wind accretion rather than accretion discs. Sorensen et al. (1974, 1975) made calculations using fluid in cell method (FLIC) and Cartesian coordinates. They took the mass-losing star and the mass-accreting star into consideration and assumed the latter to be of sufficiently small size to allow formation of an accretion disc. The results of their calculation showed a gas stream from the L1 point flowing towards the compact star and formation of an accretion disc. However, Wilson (1972) first investigated numerically time-dependent accretion of inviscid matter onto a rotating (Kerr) black hole. This was the first problem to which his formulation of the hydrodynamic equations was applied.

K. Giri, *Numerical Simulation of Viscous Shocked Accretion Flows Around Black Holes*,
Springer Theses, DOI 10.1007/978-3-319-09540-0_2

Nowadays, there is a large body of numerical investigations in the literature dealing with hydrodynamical integrations in static background space-times. Most of these are based on the Wilson formulation of hydrodynamic equations and use schemes based on finite differences with some amount of artificial viscosity. More recently, researchers have started to use conservative formulations of the equations, and their characteristic information, in the design of numerical schemes.

Satisfactory numerical solutions of hydrodynamical equations were obtained for spherical accretion Kylafis and Lamb (1979) and for steady-state flow onto magnetic white dwarfs (Wada et al. 1980). In 1981, Langer et al. presented the first time-dependent numerical solutions to hydrodynamical equations for accretion onto a white dwarf. They demonstrated that the shock height underwent a periodic limit cycle due to thermal instability in the bremsstrahlung dominated cooling. In their next paper (1981), they described in detail their method of solution and considered a wide range of accretion rates and white masses and radii of the white dwarfs. The effect of cyclotron emission on the same work was included by Chanmugam et al. (1985). Sawada et al. (1986a, b), Spruit et al. (1987) made a second attempt on the same problem that Sorenson et al. (1976) had worked on earlier. They worked using state-of-the-art techniques such as the Osher upwind finite difference method with second-order accuracy, generalised curvilinear coordinates and a supercomputer of vector type. The Osher upwind difference method can run the calculation stably while suppressing the artificial viscosity at a low level and is a predecessor of the Total Variation Diminishing (TVD) method, which is a representative modern computational fluid dynamics scheme. As a result, they discovered in accretion disc the presence of spiral shocks, the very feature that was never discovered using other schemes with more dissipations. Since then, authors have been carrying out two-dimensional simulation for accretion discs by various methods and they all obtained spiral shocks (Spruit et al. 1987; Rozyczka and Spruit 1989; Matsuda et al. 1990; Savonije et al. 1994; Godon 1997).

In the following, we present a summary of illustrative time-dependent accretion simulations in hydrodynamics. We concentrate on the progress of multidimensional simulations around black holes.

2.2 Simulation of Inviscid Flows

There are a variety of astrophysical situations in which one expects to find fluid accreting onto a black hole. Among these are the stellar collapse to a black hole, a black hole in a binary system and a supermassive black hole in active galactic nuclei. Pioneering numerical efforts in the study of black hole accretion made use of the so-called frozen star paradigm of a black hole. The first numerical attempt to study the behaviour of matter around black holes was made nearly three decades ago (Hawley and Smarr 1983). They developed a 2D axisymmetric, general relativistic, Eulerian, first-order backward space difference technique inviscid hydrodynamic accretion flow in a fixed Kerr black hole gravitational field. It was shown that the large angular

momentum accretion is accompanied by shock waves that travel outwards. These simulations also confirm the results of Wilson (1978) that non-steady shock waves are formed which travel outward. A series of important simulations were carried out with this code to show that thick accretion discs can indeed form in inviscid flows (Hawley et al. 1984a, b). In these simulations, a shock wave was found but it was not steady at all as it travelled outwards. Furthermore, theoretical models were not mature enough (no radial velocity included, for example). Fryxell et al. (1987) devoted their attention to the hydrodynamical aspects of the problem in adiabatic approximation. They presented the results of a number of numerical simulations to describe the dependence of hydrodynamical flows on the boundary conditions at the surface of the gravitating object. In the above simulations, no standing shock waves were found as the parameter space (spanned by energy and angular momentum) for which standing shock may form was not used at the outer boundary. Livio et al. (1991) showed that the shock cone exhibited a side-to-side motion, which was termed the 'flip-flop' instability. The flip-flop motion was accompanied by the episodic accretion of material with high specific angular momentum of opposite signs. With a three-dimensional extension of the axisymmetric code of Hawley et al. (1984a, b), Hawley (1991) studied the global hydrodynamic non-axisymmetric instabilities in thick, constant angular momentum accretion gas tori, orbiting around a Schwarzschild black hole. Matsuda et al. (1992) were the first to show that 2D adiabatic flows are unstable to 'flip-flop' instability even in the case of accretion from a homogeneous medium so that the density or velocity gradients merely provide an initial perturbation. Ishii et al. (1993) presented the results of two- and three-dimensional numerical hydrodynamical calculations of accretion flows of an isothermal gas past a gravitating compact object. They found that 2D isothermal flows exhibit 'flip-flop' instability both in homogeneous and non-homogeneous cases. In contrast to the finite difference method, Lin and Pringle (1976) and Hensler (1982) performed calculations with a particle method, the former in particular using the sticky particle method, which can be called a predecessor of the Smoothed Particle Hydrodynamics (SPH) method. All these calculations, having incorporated an artificial viscosity to stabilise the calculation, could not reveal the detailed structure of the inside of an accretion disc. The SPH discretization approach satisfies that the available finite number of computational nodes or grid points follow the fluid (Lagrangian description). So, it (SPH) had become a useful computational tool for complex two- and three-dimensional problems (Benz 1990), and it owes its popularity mostly to its computational simplicity. Monaghan (1988) derived SPH equations for relativistic fluids moving in a static metric. Kheyfets and Zurek (1990) devloped a formulation of SPH compatible with the principles of general relativity in which the contact interactions are modelled by spatial smoothing functions constructed explicitly in the local frame co-moving with fluid. Laguna et al. (1993) took a logical step in the progression and applied the SPH techniques in developing a computational tool to study the three-dimensional dynamics of a relativistic ideal fluid in a static curved space-time geometry. Steinmetz and Mueller (1993) compared one-dimensional plane-parallel hydrodynamic shock solutions and spherical cloud collapse and suggested some improvements in the SPH technique to minimise dissipation. Davis et al. (1993) compared the collisions of a

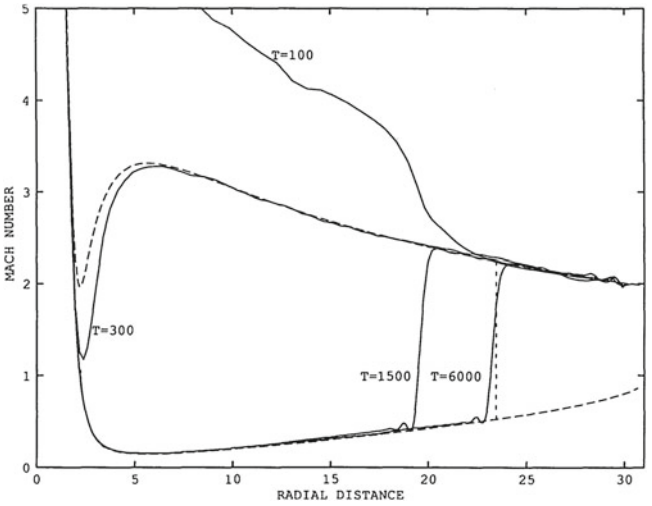

Fig. 2.1 An example of the simulation of a thin accretion disc which includes a standing shock wave. Mach number of the flow is plotted against the radial distance. Results at different times are shown as *solid curves*. Analytical solution is shown as a *dashed curve* with vertical shock transition. The flow forms the shock at the predicted location. This figure has been taken from Chakrabarti and Molteni (1993)

main-sequence star with a white dwarf and showed satisfactory performance of SPH as well as finite difference code. Laguna et al. (1994) compared a general relativistic SPH code for one-dimensional plane-parallel shock solutions and spherical inflows with and without pressure. They found good agreement with the analytical solution. Several numerical works were done by various authors using SPH code written in axisymmetric coordinate system using Pseudo-Newtonian potential. Chakrabarti and Molteni (1993) presented the results of numerical simulations of thin accretion discs and winds. They showed that their simulation agrees very well with the theoretical work (Chakrabarti 1990a) on shock formation. The most significant conclusion was that shocks in an inviscid flow were extremely stable. Figure 2.1 shows an example of the simulation of a thin accretion disc which includes standing shock waves (Chakrabarti and Molteni 1993). Mach number of the flow is plotted against the radial distance (in units of Schwarzschild radius of the central black hole). Solid curves are simulation results and dashed curves are the supersonic and subsonic branches, respectively. Two vertical dashed lines indicate locations of analytically predicted shock transitions, the outer one being stable. After a transient phase, a shock forms near the inner edge which then travels outward till it reaches the outer stable shock. Molteni et al. (1994) simulated the formation of a thick disc. For a large number of cases they also found the formation of strong winds which are hot and subsonic when originating from the disc surface very close to the black hole, but become supersonic within a few tens of Schwarzschild radii of the black hole. They also showed that in the case of higher angular momentum, the black hole accretes very less amount of

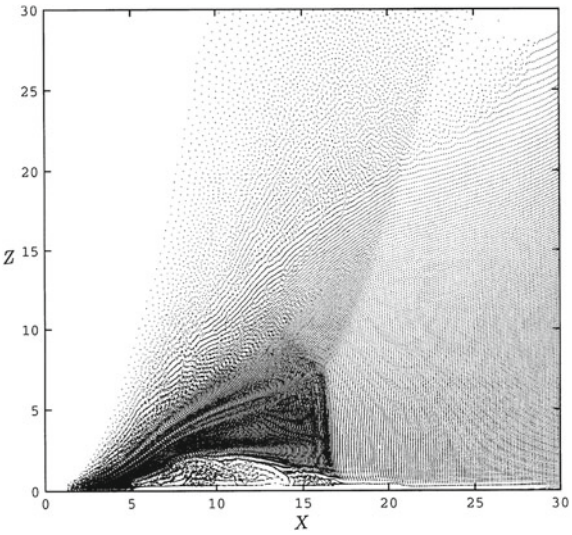

Fig. 2.2 Pseudo-particles in a smoothed particle hydrodynamic simulation of a two-dimensional sub-Keplerian angular momentum flow. The figure has been taken from Molteni et al. (1994)

matter and most of the matter is driven outwards as a strong wind. Figure 2.2 shows the particle distribution in which the standing shock at X 16 is clearly visible. The presence of oblique shock is also visible.

Sponholz and Molteni (1994) studied the shock formation around a Kerr black hole and found differing shock locations in co-rotating and contra-rotating flows. Molteni et al. (1996) extended their earlier numerical simulation (MLC96) of accretion discs with shock waves when cooling effect are also included. They considered bremsstrahlung and other power-law processes to mimic cooling in the simulation. They observed that for a given angular momentum of the flow, the shock wave undergoes a steady, radial oscillation with the period roughly equal to the cooling time. As a result of oscillations, the energy output from the disc also varies quasi-periodically.

In 1982, Ami Harten published a groundbreaking paper that became the basis of Computational Fluid Dynamics (CFD) research for many years to come. Under the title 'High Resolution Schemes for Hyperbolic Conservation Laws', Harten introduced the term total variation non-increasing (TVNI), which was later shortened by other researchers to TVD. The details of the TVD scheme are discussed in the next chapter. A series of numerical simulations of accretion flows around compact objects have been done using TVD scheme. Ryu et al. (1993) described an explicit second-order finite difference code based on a TVD scheme for self-gravitating cosmological hydrodynamics systems. This code was developed to follow correctly the adiabatic changes of extremely supersonic pre-shock flows with Mach number larger than 100 as well as very strong shocks. Various numerical experiments proved that the code could handle the expanding low density regions very well as well as conserve the total energy accurately. The details of the original TVD scheme are described in detail in that paper. In continuation of the previous work, Ryu et al. (1995) analysed the steady-state flow structure around a central object obtained from numerical sim-

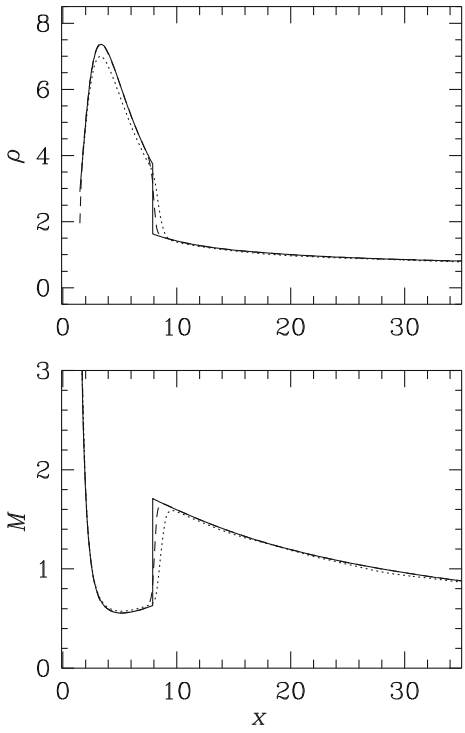

Fig. 2.3 Comparison of analytical and numerical results for 1D. Here, $\mathcal{E} = 0.036$ and $\lambda = 1.80$. The *long-* and *short-dashed curves* are the results of the TVD and SPH simulations, respectively. The *solid curve* is the analytical result for the same parameters. *Upper panel* is the mass density in arbitrary units, and the *lower panel* is the Mach number of the flow. Here the flow passes through the outer sonic point (at $x_o = 27.9$), then through a shock (at 7.89) and finally through the inner sonic point (at 2.563). This figure has been taken from Molteni et al. (1996)

ulations in the case with finite flow thickness. The calculation discussed in that paper showed good qualitative agreement with similar calculations done previously in Molteni et al. (1994). They suggested a possible explanation for the unstable behaviour of the thin accretion flow with vanishing thickness based on 1.5D model.

A comparative study between the results of TVD method and SPH method was made by Molteni et al. (1996). They compared the results of numerical simulations of thin and quasi-spherical accretion with existing analytical solutions. They showed that in one-dimensional thin flows, the result of both simulations (with or without shock) agrees well with each other and also with analytical solutions. Comparisons of analytical and numerical solutions in one-dimensional case are given in Fig. 2.3. See the caption for details. However, for two-dimensional thick flows, there was some variation between the two results. With the confidence that their codes were reasonably good to study time-dependent flows, they presented more complex behaviour of time-dependent accretion flows in their next paper (Ryu et al. 1997). In that paper Ryu et al. (1997), they characterised the nature of thin, axisymmetric, inviscid accretion flows of cold adiabatic gas with zero-specific energy in the vicinity of a black hole by the specific angular momentum. They showed that when the flow has small angular momentum ($\lambda \leq \lambda_{\rm mb}$, where $\lambda_{\rm mb}$ is marginally bound value), most of the material is accreted into the black hole and when the flow has large angular momentum ($\lambda > \lambda_{\rm mb}$) almost no accretion into the black hole occurs. Igumenshchev

and Beloborodov (1997) performed two-dimensional relativistic hydrodynamical simulations of inviscid transonic disc accretion onto a rotating (Kerr) black hole. In the next section, we discuss only the recent progress on simulations of viscous flows.

2.3 Simulation of Viscous Flows

The simulation of viscous accretion discs around black holes in astrophysics is currently an active field of research. The question of the two-dimensional structure of flow patterns in accretion discs was first raised nearly three decades ago. On the theoretical side, since the pioneering work on SS73 thin disc models, parameterized by the so-called α-viscosity in which the gas rotates with Keplerian angular momentum and transported radially by viscous stress, have been applied successfully to many models. All black hole accretion flow models require that angular momentum be removed from the flow in some way so that the material can flow inward. It has long been suspected that diffusion of angular momentum through an accretion flow is driven by turbulence. The α-model (Shakura and Sunyaev 1973) introduced a phenomenological shear stress into the equations of motion to model the effects of this turbulence. Pringle (1981) pointed out that in presence of viscosity, most of the matter of the disc accretes into the black hole while most of the angular momentum is taken farther away by very little matter. Using α viscosity Urpin (1984) obtained the flow structure by applying first- and second-order corrections to the standard one-dimensional approximations of the equations of hydrodynamics.

Full two-dimensional simulations reported by Robertson and Frank (1986) followed the viscous evolution of an accretion disc around a white dwarf. The first two-dimensional hydrodynamical calculations with radiation transport for an accretion disc around black holes was apparently those of Eggum et al. (1987). Meanwhile, work had begun with turbulent viscosity by convection in accretion discs in various approaches. Papaloizou and Lin (1988) and Ryu and Goodman (1992) studied convective instabilities in thin gaseous discs and confirmed that angular momentum transport can be supported by convective turbulence. Goldman and Wandel (1995) investigated accretion discs where viscosity is solely given by convection and where the energy transport is maintained by radiation and convection. They found the resulting viscosity too low by a factor of 10 to 100.

It has been shown by Chakrabarti (1989) that low angular momentum, non-dissipative flows produce axisymmetric standing shock waves in tens of Schwarzschild radii, but the presence of a large viscosity (Chakrabarti 1990b) will remove the shock wave since the Rankine-Hugoniot relation is not satisfied in highly dissipative flow. The general conclusion was that the stable shock (X_{s3} in the notation of Chakrabarti 1990b) is weaker and forms farther away as the viscosity parameter is increased. When the viscosity is very high, shocks do not form at all. A confirmation of such an assertion, originally made in the context of isothermal flows, came through both numerical simulations (Chakrabarti and Molteni 1995) and theoretical studies of flows with more general equation of states (Chakrabarti 1996; Chakrabarti and Das 2004; Das and Chakrabarti 2004).

Chakrabarti and Molteni (1995) studied on numerical evolution of viscous isothermal discs, with particular emphasis on the nature of shocks in flows close to a black hole. They showed that, if the transport of angular momentum follows Shakura and Sunyaev (1973) α-viscosity prescription, a shock must form where a jump of angular momentum takes place. When the viscosity is very small, they show that the transport rates of angular momentum on both sides of the shock could match and the shock can remain steady. In this case, the shock is weaker and forms farther away from the black hole. When the viscosity parameter is increased, the shock wave is driven outwards and the disc in the post-shock flow becomes Keplerian. They also find that for high viscosity, the shock disappears and the disc becomes almost Keplerian except very close to the inner edge of the disc. In Fig. 2.4a, b, the Mach number and angular momentum variations in viscous (solid) and inviscid (dashed) flows are shown. Igumenshchev et al. (1996) studied two-dimensional flows but concentrated only on the inner region of the disc, namely the region less than $20r_g$. The main

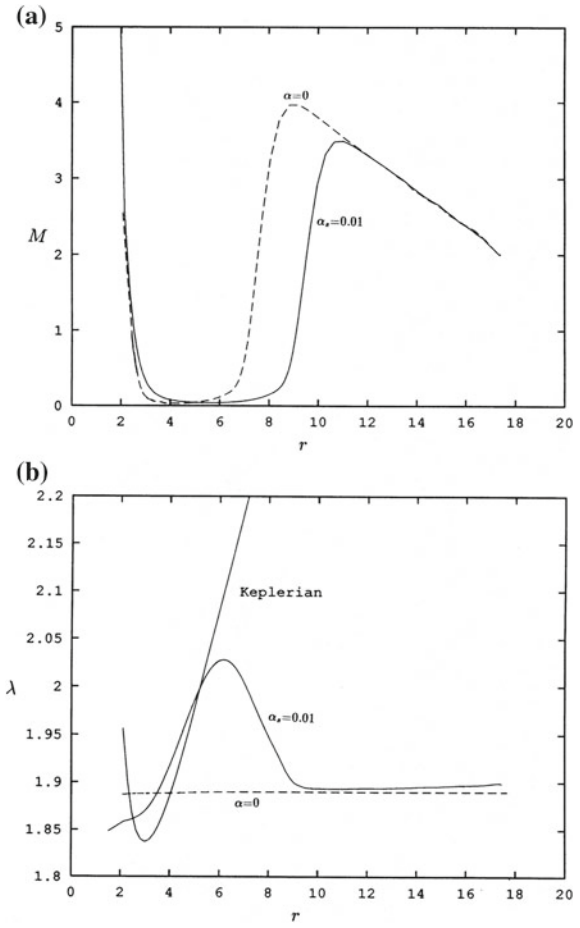

Fig. 2.4 Comparison of **a** Mach number and **b** angular momentum variations in viscous (*solid*) and inviscid (*dashed*) isothermal thin accretion discs. The viscosity parameter $\alpha_s = 0.01$ is chosen everywhere in the simulation. Note that the shock in the viscous disc forms farther out and is weaker and wider. The *solid curve* in (**b**) marked 'Keplerian' is the Keplerian distribution plotted for comparison. Due to the inefficiency of transfer of angular momentum in the pre-shock flow, a mixed-shock forms with higher angular momentum in the post-shock flow (Chakrabarti and Molteni 1993)

interest was to study the transonic nature of the flow just before the matter enters into the horizon. They find that a torus-like structure forms close to the black hole and the angular momentum increases outward. Igumenshchev and Beloborodov (1997) used the finite difference method and allowed the heat generated by viscosity heating to be radiated away or absorbed totally. The computational box was up to $300r_g$, but the outer boundary condition was that of a near-Keplerian flow having no radial velocity. The inner boundary was kept at $3r_g$. Thus, the possibility of having a shock or the inner sonic point was excluded. The disc was found to be stable for very high viscosity parameter and less stable for lower α. Igumenshchev and Abramowicz (2000) extended the earlier work by studying dependence on the polytropic index γ which varied from 4/3 to 5/3 as well as viscosity parameter and again found that the stability of the solutions depends on these parameters.

Using SPH code (Lanzafame et al. 1998), studied the behaviour of sub-Keplerian viscous transonic flows when flow is neither isothermal nor restricted only to the equatorial plane as in CM95. They found that even two-dimensional thick discs, shocks form and the steady shock location increase with viscosity as in one-dimensional study of CM95. They also showed that beyond the critical viscosity when a steady shock was not expected, the flow forms an unsteady shock which periodically evacuates the discs. Figure 2.5a–d show the drifting of steady shock location in a two-

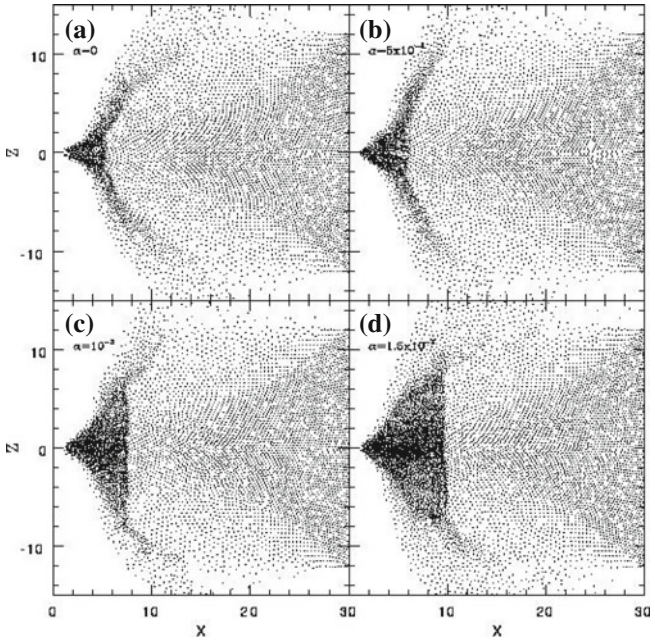

Fig. 2.5 Drifting of the steady shock location in a two-dimensional, axisymmetric accretion flows as the viscosity parameters. Here, the specific angular momentum $\lambda = 1.6$ and energy $\mathcal{E} = 0.001955219$. (**a**) is for the inviscid flow. **b–d** shows the effect of the introduction of viscosity in the flow. The viscosity parameter α is 5×10^{-4} in (**b**), 10^{-3} in (**c**) and 1.5×10^{-3}, respectively. This figure has been taken from Lanzafame et al. (1998)

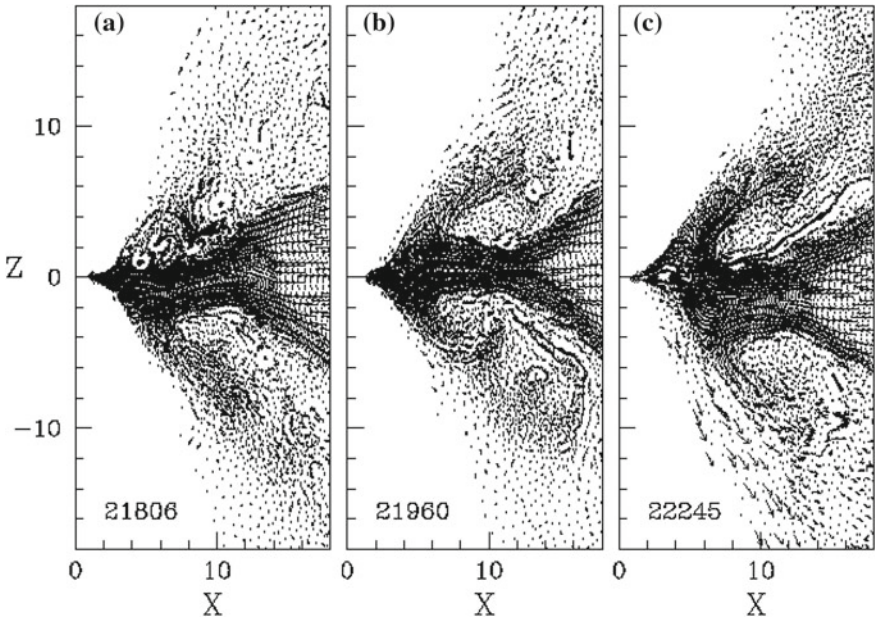

Fig. 2.6 Snapshots of simulations of accretion discs around a $10^8 M_\odot$ black hole by Smoothed Particle Hydrodynamics for three different times in (**a**), (**b**) and (**c**). The *dots* are the particle locations and *arrows* are drawn for every fifth particle for clarity. In (**a**), (**b**) and (**c**) times (in units of r_g/c) is marked in each box. Note the vertical as well as radial oscillation of the accretion shock wave located at $\sim 13 r_g$ (from Chakrabarti et al. 2004)

dimensional, axisymmetric accretion flow as the viscosity parameter is increased towards the critical value. Clearly, as in the one-dimensional case, higher viscosity causes higher differential angular momentum transport between the pre-shock and post-shock solutions and as a result the shock is drifted away in the radial direction until the momentum balance is reached.

Chakrabarti et al. (2004) presented the results of several numerical simulations of two-dimensional axisymmetric accretion flows around black holes using Smoothed Particle Hydrodynamics (SPH) in the presence of cooling effects. They consider both stellar black holes and supermassive black holes. They showed examples of shock formation which exhibit radial and/or vertical oscillations. The result of their simulation is shown in Fig. 2.6. In recent times, a few simulations of disc-outflow coupling have been done (Nishikawa et al. 2007; McKinney and Narayan 2007). However, the results are strongly dependent on the initial conditions (Ustyugova et al. 1999) and it is difficult to simultaneously simulate the disc and the outflow regions because the timescales of the accretion and outflow are in general very different. Moreover, in these simulations, how the matter gets deflected from the equatorial plane has been studied largely in the context of Keplerian disc regime.

2.4 Goals of the Thesis

There exist a few dominating factors that determine the morphology of an accretion flow. A significant factor is how fast the angular momentum of accreting matter can be eliminated. The accreting matter invariably can have too much angular momentum if the matter is supplied through Roche lobe overflow, which prohibits itself to fall directly onto the black hole. Therefore, there must be a mechanism by which accreting matter can rapidly transport a large amount of angular momentum. Most of the time, some kind of effective viscosity is generally adopted for the purpose, but the physical cause is not fully understood. On the other hand, if accretion is through winds, the problem of transport of angular momentum is not so accurate. In this case, the opposite problem, namely how to produce a Keplerian disc through transport of angular momentum from a low angular momentum flow is more relevant. In our work, viscosity in accreting matter is described as in the Shakura and Sunyaev (1973) prescription. Viscosity is also an important parameter that controls the ability of the accreting disc to produce dissipative heat from kinetic energy. Besides, the processes of radiative cooling and optical thickness are significant. They determine whether the disc will be stable as a single component or behave differently at different regions as, for example, in two component advective flows (Chakrabarti and Titarchuk 1995).

In this thesis work, we extend the numerical work of Chakrabarti and Molteni (1995), Molteni et al. (1996) and Lanzafame et al. (1998) and provide a model that closely resembles realistic astrophysical accretion discs around black holes, while being restricted to two dimensions. In particular, the hydrodynamic evolution of the disc is followed with a grid-based Total Variation Diminishing (TVD) code, which approximates a gas with a finite difference method (Harten 1983). The evolution in phase space of this gas is determined by the Eulerian form of the hydrodynamic equations. We start our work by studying the time variation of the evolution of the inviscid accretion discs around black holes, and their properties. We also study the change in the pattern of the flows when the strength of the shear viscosity is varied. However, for a given set of incident flow parameters (e.g. specific energy, specific angular momentum and viscosity), the flow may possess multiple critical points (Chakrabarti 1989, 1990a, b). This suggests the possible existence of global solutions in one dimension with standing and oscillating shocks located between two critical points. Our objective is to verify these theoretical predictions through numerical simulations under different input parameters. For a two-dimensional flow, a completely self-consistent theoretical solution is not possible. Thus, a numerical simulation is necessary to reveal the queries. The classifications were made using three different models of the flow, namely a disc of constant thickness, a disc with conical wedge cross section and a disc in vertical equilibrium (Chakrabarti and Das 2001). Our motivation was to study whether a simulated result reproduces theoretical models or not. It has been shown by C89 that low angular momentum, non-dissipative flows produce axisymmetric standing shock waves in tens of Schwarzschild radii, but the presence of a large viscosity in Chakrabarti (1990b) will remove the shock wave since the Rankine-Hugoniot relation is not satisfied in highly dissipative flow.

Our aim is to verify these theoretical results through numerical simulations in two-dimensional system. However, the viscous flow must also be cooled in order that not only the flow has Keplerian angular momentum distribution but also its temperature is cold enough so that a standard (Shakura and Sunyaev 1973) disc is produced. Thus, our goal is also to form a Keplerian disc using numerical simulations that include viscosity and cooling. In my thesis, the effect of the shear viscosity on the evolution of non-self-gravitating discs is investigated when a simple power-law cooling takes place inside the flow.

2.5 Some Remarks on Units and Dimensions

The radius of a non-rotating black hole $r_g = 2GM/c^2$ is only 3.0 km if $M = M_\odot$. A stellar mass black hole generally has $M > 3M_\odot$. Hence, the radius is around 9 km. For a supermassive black hole, one can scale these numbers depending on the mass of the black hole. However, the physical processes in accretion flows generally have length scales of the order of the Schwarzschild radius and thus, it is convenient to choose this as the unit of length. Similarly, it is well known that the velocity of in-falling matter through the horizon is equal to the velocity of light (Chakrabarti 1996). Thus, it is expected that matter and sound velocities would be of this order and thus the units may be chosen accordingly.

Keeping these in mind, we choose, $2G = c = M = 1$. In this case, the unit of velocity would be c, the unit of distance would be $2GM/c^2$ (the Schwarzschild radius), the unit of time would be $2GM/c^3$ and the unit of angular momentum would be $2GM/c$. In this unit system, the pseudo-Newtonian potential is written as $-\frac{1}{2(r-1)}$.

References

Benz, W. (1990). *Proceedings of the NATO Advanced Research Workshop* (p. 269). Les Arcs, France
Biermann, P. (1971). *Astronomy and Astrophysics*, *10*, 205.
Chakrabarti, S. K. (1989). *Astrophysical Journal*, *347*, 365.
Chakrabarti, S. K. (1990a). *MNRAS*, *243*, 610.
Chakrabarti, S. K. (1990b). *Theory of Transonic Astrophysical Flows*. Singapore: World Scientific.
Chakrabarti, S. K. (1996). *Physics Reports*, *266*, 229.
Chakrabarti, S. K., & Das, S. (2001). *MNRAS*, *327*, 808.
Chakrabarti, S. K., & Das, S. (2004). *MNRAS*, *349*, 649.
Chakrabarti, S. K., & Molteni, D. (1995). *MNRAS*, *272*, 80.
Chakrabarti, S. K., & Titarchuk, L. G. (1995). *Astrophysical Journal*, *455*, 623.
Chakrabarti, S. K., Acharyya, K., & Molteni, D. (2004). *Astronomy and Astrophysics*, *421*, 1.
Chakrabarti, S. K., & Molteni, D. (1993). *Astrophysical Journal*, *417*, 671.
Chanmugam, G., Langer, S. H., & Shaviv, G. (1985). *Astrophysical Journal*, *299*, 87.
Das, S., & Chakrabarti, S. K. (2004). *IJMPD*, *13*(9), 1955.
Davis, D. R., Ryan, E. V., & Farinella, P. (1993). *LPICo*, *810*, 84.
Eggum, G. E., Coroniti, F. V., & Katz, J. I. (1987). *Astrophysical Journal*, *323*, 634.
Fryxell, B. A., & Taam, Ronald E. (1987). *Astrophysical Journal*, *315*, 536.
Godon, P. (1997). *Astrophysical Journal*, *480*, 329.

Goldman, I., & Wandel, A. (1995). *Astrophysical Journal*, *443*, 187.
Harten, A. (1983). *Journal of Computational Physics*, *49*, 357.
Hawley, J. F. Smarr, L. (1983). *Bulletin of the American Astronomical Society*, *15*, 963.
Hawley, J. F., Smarr, L. L., & Wilson, J. R. (1984a). *Astrophysical Journal*, *277*, 296.
Hawley, J. F., Smarr, L. L., & Wilson, J. R. (1984b). *Astrophysical Journal*, *55*, 211.
Hawley, J. F. (1991). *Astrophysical Journal*, *381*, 496.
Hensler, G. (1982). *Astronomy and Astrophysics*, *114*, 309.
Huang, S. S. (1965). *Astrophysical Journal*, *141*, 201.
Huang, S. S. (1966). *Astrophysical Journal*, *146*, 25.
Igumenshchev I. V., & Abramowicz M. A. 2000. *Astrophys. J.*, **130**, 463.
Igumenshchev, I. V., Chen, X., & Abramowicz, M. A. (1996). *MNRAS*, *278*, 236.
Igumenshchev, I. V., & Beloborodov, A. M. (1997). *MNRAS*, *284*, 767.
Ishii, T., Matsuda, T., Shima, E., Livio, M., Anzer, U., & Boerner, G. (1993). *Astrophysical Journal*, *404*, 706.
Kheyfets, A. M., Miller, W. A., & Zurek, W. H. (1990). *Physical Review D*, *41*, 451.
Kylafis, N. D., Lamb, D. Q. (1979). *Astrophyscial Jornal*, *228*, 105.
Laguna, P., Miller, W. A., & Zurrek, W. H. (1993). *Astrophysical Journal*, *404*, 678.
Laguna, P., Miller, W. A., & Zurrek, W. H. (1994). *MdSAI*, *65*, 129.
Lanzafame, G., Molteni, D., & Chakrabarti, S. K. (1998). *MNRAS*, *299*, 799.
Lin, D. N. C., & Pringle, J. E. (1976). *BAASI*, *8*, 450.
Livio, M., Soker, N., Matsuda, T., & Anzer, U. (1991). *MNRAS*, *253*, 633.
Matsuda, T., Sekino, N., Shima, E., Sawada, K., & Spruit, H. (1990). *Astronomy and Astrophysics*, *235*, 211.
Matsuda, T., Ishii, T., Sekino, N., Sawada, K., Shima, E., Livio, M., et al. (1992). *MNRAS*, *225*, 183.
McKinney, J. C., & Narayan, R. (2007). *MNRAS*, *375*, 513.
Molteni, D., Sponholz, H., & Chakrabarti, S. K. (1996). *Astrophysical Journal*, *457*, 805.
Molteni, D., Lanzafame, G., & Chakrabarti, S. K. (1994). *Astrophysical Journal*, *425*, 161.
Molteni, D., Ryu, D., & Chakrabarti, S. K. (1996). *Astrophysical Journal*, *470*, 460.
Monaghan, J. J. (1988). *Computer Physics Communications*, *48*, 88.
Nishikawa, K.-I., Hartmann, D. H., Hardee, P., Hededal, C., Mizunno, Y., & Fishman, G. J. (2007). *ESASP*, *622*, 223.
Papaloizou, J. C. B., Lin, D. N. C. (1988). *Astrophyscial Journal*, *331*, 838.
Prendergast, K. H. (1960). *Astrophysical Journal*, *132*, 162.
Prendergast, K. H., & Taam, R. E. (1974). *Astrophysical Journal*, *189*, 125.
Pringle, J. E. (1981). *ARAA*, *19*, 137.
Robertson, J. A., & Frank, J. (1986). *MNRAS*, *221*, 279.
Rozyczka, M., & Spruit, H. C. (1989). *Kluwer Academic Publishers*, *290*, 341.
Ryu, D., Chakrabarti, S. K., & Molteni, D. (1997). *Astrophysical Journal*, *474*, 378.
Ryu, D., & Goodman, J. (1992). *Astrophysical Journal*, *388*, 438.
Ryu, D., Ostriker, J. P., Kang, H., & Cen, R. (1993). *Astrophysical Journal*, *414*, 1.
Ryu, D., Brown, G. L., Ostriker, J. P., & Loeb, A. (1995). *Astrophysical Journal*, *452*, 364.
Savonije, G. J., Papaloizou, J. C. B., & Lin, D. N. C. (1994). *MNRAS*, *268*, 13.
Sawada, K., Matsuda, T., & Hachisu, I. (1986a). *MNRAS*, *219*, 75.
Sawada, K., Matsuda, T., & Hachisu, I. (1986b). *MNRAS*, *221*, 679.
Shakura, N. I., & Sunyaev, R. A. (1973). *Astronomy and Astrophysics*, *24*, 337.
Sorensen, S., Matsuda, T., & Sakurai, T. (1974). *Progress of Theoretical Physics*, *52*, 333.
Sorensen, S., Matsuda, T., & Sakurai, T. (1975). *Astronomy and Space Science*, *33*, 465.
Sorenson, S.A., Matsuda, T., Fujimoto, M. (1976). *Astrophy Space Science*, *43*, 491.
Sponholz, H., & Molteni, D. (1994). *MNRAS*, *271*, 233.
Spruit, H. C., Matsuda, T., Inoue, M., & Sawada, K. (1987). *MNRAS*, *229*, 517.
Steinmetz, M., & Mueller, E. (1993). *Astronomy and Astrophysics*, *268*, 391.
Urpin, V. A. (1984). *Soviet Astronomy*, *28*, 50.

Ustyugova, G. V., Koldoba, A. V., Romanova, M. M., Chechetkin, V. M., & Lovelace, R. V. E. (1999). *Astrophysical Journal*, *516*, 221.
Wada, T., Shimizu, A., Suzuki, M., Kato, M., & Hoshi, R. (1980). *Progress of Theoretical Physics*, *64*, 1986
Wilson, J. R. (1978). *Proceedings of the Workshop* (p. 423). Seattle, Washington
Wilson, J. R. (1972). *Astrophysical Journal*, *173*, 431.

Chapter 3
Governing Equations and Computational Methods

Abstract We describe the numerical methods employed to model accretion flows and their implementation in a FORTRAN code. We present all the governing equations for both non-viscous and viscous flows. We discuss the solution technique for a non-viscous system. Subsequently, we give all the schemes to incorporate turbulent viscosity in the non-viscous system. Finally, we add a power-law cooling in our viscous system and study the properties.

In this chapter, we present the equations describing our accretion flows as well as the rationale behind the numerical method and numerical code we use to solve them. We show that numerical simulations can be tractable only if one defines a physically acceptable and realistic initial and boundary condition.

In fact, in an accretion disc close to a black hole, all matter is composed of discrete particles, especially the free electrons and ions. So, it is expected that both in the interstellar medium and in the plasma transferred between binary stars, the accretion flow onto compact objects will be hydrodynamical in nature. So, the accretion flow problems considered herein are assumed to be governed by the *Navier-Stokes equations*, hereafter *NS equations*. This set of equations is simply a recasting of the following conservation laws:

Conservation of Mass
Conservation of Momentum
Conservation of Energy

The equation of the application of the 'Conservation of Mass' law to a fluid flow is called a continuity equation. Similarly, when the law of 'Conservation of Momentum' (i.e. Newton's second law) is applied to a fluid flow, the resulting equations are referred to as the momentum equations. Finally, the application of the 'Conservation of Energy' law to a fluid flow yields an energy equation. Black holes have no hard surfaces or magnetic fields like stars. However, the centrifugal barrier becomes strong closer to the hole and matter stops virtually at the barrier. This barrier behaves like a boundary layer (Chakrabarti 1990). Matter enters through an imaginary one-way wall called the event horizon. The self-gravity and the slow increase in the central mass are generally ignored. In the first chapter, we have discussed the fluid dynamical aspects of an accretion flow. In this chapter, we present all the governing equations that come from fluid dynamics to formulate the accretion flow problem in our system.

K. Giri, *Numerical Simulation of Viscous Shocked Accretion Flows Around Black Holes*,
Springer Theses, DOI 10.1007/978-3-319-09540-0_3

3.1 Equations for Inviscid Flows

The conservation equations for inviscid flow, commonly referred to as the *Euler equations*, are derived from the *NS equations* by ignoring the viscous stress tensor and heat flux vector. This can be accomplished by simply setting the dynamic viscosity equal to zero and thus the model is *inviscid*. Assuming the pseudo-Newtonian potential (Paczyński and Wiita 1980), from Eq. 1.23, the *Euler equations* are given as (Landau and Lifshitz 1959):

$$\rho\left[\frac{\partial \mathbf{v}}{\partial t} + \mathbf{v}.\nabla\mathbf{v}\right] = \nabla P + \rho\mathbf{G}, \tag{3.1}$$

where,

$$\mathbf{G} = -\frac{1}{2(R-1)^2 R}\frac{\mathbf{R}}{R}, \tag{3.2}$$

with the components,

$$G_r = -\frac{1}{2(R-1)^2 R}\frac{r}{R}, \tag{3.3}$$

$$G_z = -\frac{1}{2(R-1)^2 R}\frac{z}{R}. \tag{3.4}$$

Here, $R = \sqrt{r^2 + z^2}$ in cylindrical coordinate system (r, θ, z) which has been chosen in our system. It is noted that in cylindrical coordinates, the components of the velocity vector are given as $\mathbf{v} = (v_r, v_\phi, v_z)$.

3.1.1 Ideal Gas Equation of State

For an ideal gas,

$$p = \rho R T, \tag{3.5}$$

where $R = R_u/M_w$ is the specific gas constant with R_u, the universal gas constant and M_w the molecular weight of the gas. For an ideal gas the following relation is valid:

$$c_p - c_v = R, \tag{3.6}$$

where c_p is the specific heat at constant pressure and c_v is the specific heat at constant volume. γ is the ratio of specific heats, which is also called the adiabatic index and is defined as

$$\gamma = c_p/c_v. \tag{3.7}$$

For an ideal gas, one can write

$$de = c_v dT, \tag{3.8}$$

and assuming that c_v does not depend on temperature, the integration yields

$$e = e_0 + c_v T, \tag{3.9}$$

where e_0 is not uniquely determined, and one could choose any value for e at 0K. We take $e_0 = 0$ arbitrarily for simplicity. It is noted that

$$p = \rho RT = \frac{R}{c_v}\rho e = \frac{c_p - c_v}{c_v}\rho e = \rho(\gamma - 1)e = (\gamma - 1)\rho e. \tag{3.10}$$

So, our equation of state is

$$p = (\gamma - 1)\rho e,$$

or

$$p = \left(\gamma - 1\right)\left(E - \frac{\rho \mathbf{v}^2}{2}\right), \tag{3.11}$$

where, E is the energy density function.

3.1.2 Equations for Inviscid Flows in Conservative Form

For the subsequent eigensystem analysis, it is advantageous to write the Euler equations in a column vector format, where each column represents the full set of conserved properties—mass, momentum and energy. Note that all the column vectors, being five dimensional, are denoted by half arrows and are thus distinguishable from three-dimensional physical vectors. So, in case of axisymmetric, non-magnetic flow without viscosity, combining Eqs. 1.22, 3.1 and 1.24, the mass, momentum and energy conservation equations are written in compact column format using non-dimensional units as (Molteni et al. 1996, LMC97):

$$\frac{\partial q}{\partial t} + \frac{1}{r}\frac{\partial (r F_1)}{\partial r} + \frac{\partial F_2}{\partial r} + \frac{\partial G}{\partial z} = S, \tag{3.12}$$

where, the state vector is

$$q = \begin{pmatrix} \rho \\ \rho v_r \\ \rho v_\theta \\ \rho v_z \\ E \end{pmatrix}, \tag{3.13}$$

the flux functions are

$$F_1 = \begin{pmatrix} \rho v_r \\ \rho v_r^2 \\ \rho v_\theta v_r \\ \rho v_z v_r \\ (E+p)v_r \end{pmatrix} \quad F_2 = \begin{pmatrix} 0 \\ p \\ 0 \\ 0 \\ 0 \end{pmatrix} \quad G = \begin{pmatrix} \rho v_z \\ \rho v_r v_z \\ \rho v_\theta v_z \\ \rho v_z^2 + p \\ (E+p)v_z \end{pmatrix}, \tag{3.14}$$

and the source function is,

$$S = \begin{pmatrix} 0 \\ \frac{\rho v_\theta 2}{r} - \frac{\rho r}{2\left(\sqrt{r^2+z^2}-1\right)^2\sqrt{r^2+z^2}} \\ -\frac{\rho v_r v_\theta}{r} \\ -\frac{\rho z}{2\left(\sqrt{r^2+z^2}-1\right)^2\sqrt{r^2+z^2}} \\ -\frac{\rho(r v_r + z v_z)}{2\left(\sqrt{r^2+z^2}-1\right)^2\sqrt{r^2+z^2}} \end{pmatrix}. \tag{3.15}$$

Here, energy density E (without the potential energy) is defined as $E = p/(\gamma - 1) + \rho(v_r^2 + v_\theta^2 + v_z^2)/2$, ρ is the mass density, γ is the adiabatic index, p is the pressure, v_r, v_θ and v_z are the radial, azimuthal and vertical components of velocity respectively. In the case of axisymmetric flow without viscosity, the equation for azimuthal momentum states simply the conservation of specific angular momentum λ

$$d\lambda/dt = 0. \tag{3.16}$$

3.2 Numerical Approach to Solving Equations

One of the important methods to solve numerically the partial differential equations is known as the finite difference method. We briefly discuss the basics of this method.

3.2.1 Finite Difference Methods

Finite difference methods are based on approximations in which the continuous flow variables (e.g. density ρ, velocity v, etc.) are discretized. A finite set of discretized values ρ_i and v_i is defined at N distinct points in space called grid points. The advantages of this method are richness and simplicity. Next, we discuss the discretization process.

3.2.2 Discretization

We are interested in constructing a discretization for the hyperbolic system of conservation laws

$$\mathbf{U_t} + \mathbf{F}(\mathbf{U})_\mathbf{x} = 0. \tag{3.17}$$

Assuming that the system has N equations, the Jacobian,

$$\mathbf{J} = \frac{\partial \mathbf{F}}{\partial \mathbf{U}}, \tag{3.18}$$

will be an $N \times N$ matrix. Furthermore, we know that $\mathbf{J}$ is diagnosable, since the system is hyperbolic. Let us denote the eigenvalues, left eigenvectors and right eigenvectors of $\mathbf{J}$ as λ^p, L^p, R^p, respectively, for $p = 1, \ldots, N$. Thus, one can choose the left and right eigenvectors so that for,

$$L = (L^1 L^2 .....L^N),\ R = (R^1 R^2 ....R^N), \tag{3.19}$$

the relation $RL = LR = I$ holds. That is, R and L are chosen to be inverses. In case of a linear, constant coefficient system, the Jacobian is a constant matrix. In general, the Jacobian, and hence its eigenstate, will be spatially varying.

As in the scalar case, the discretization is of the form

$$(\mathbf{U}_i)_t + \frac{\mathbf{F}_{i+\frac{1}{2}} - \mathbf{F}_{i-\frac{1}{2}}}{\Delta t} = 0. \tag{3.20}$$

For the grid point k, we need to compute the numerical flux functions at $x_{k+\frac{1}{2}}$ and $x_{k-\frac{1}{2}}$. Later, we discuss computing of $\mathbf{F}_{k+\frac{1}{2}}$.

Based on the coordinate systems, finite difference method is classified into two types of methods, Lagrangian and Eulerian methods. In practice, one can solve the system of hyperbolic equations by advocating them on the mesh. Of course, there is no ideal and universally acceptable method and some problems require entirely different methods than others.

3.2.3 Lagrangian Method

In a Lagrangian method, the location of the grid points is allowed to move along with fluid. The advantage of this method is that it ensures conservative properties by definition. The disadvantage of this method is that sometimes it has trouble to move the mesh and the mesh could be distorted in a complicated way for incompressible flows in two or higher dimensions and so the accuracy is lost in a significant manner. There is also another disadvantage to this method: the method has to rely on artificial viscosity for supplying the necessary entropy injection in shocks. The shocks are unavoidably broadened over the smoothing scale and can no longer be resolved as discontinuities.

3.2.4 Eulerian Method

On the other hand, the Eulerian method keeps the grid points fixed in positions, so that distortion of the grid points is not required. In traditional Eulerian methods, the space is discretized and the gas variables are represented on a mesh: $x \rightarrow x_i$ and $t \rightarrow t^n$. The numerical solution is obtained on these discrete mesh points. Thus, the functions such as $q(x, t)$ are replaced by their discrete counterparts $q(x_i, t^n) = {q_i}^n$. The equations must be formulated in a way that ${q_i}^{n+1}$ can be derived from q_i. The difficulty is then to formulate the discretized form of the differential equations, such that the solutions for the ${q_i}^{n+1}$ are numerically stable and as close as possible to the true $q(x, t)$.

Though there are some truncation errors in this method, after a long run, the accuracy and positivity come back. In spite of this, the Eulerian method has the powerful advantage of general application to two- and three-dimensional problems, compared with Lagrangian methods. Actual applications of the Eulerian method to astrophysics are extensive. There are decades of experience with Eulerian methods and for various problems accurate schemes exist, which offer high-order spatial accuracy, have negligible post-shock oscillations and low numerical diffusivity. Moreover, the mesh-based codes offer superior resolving power for shocks, with some methods able to capture shocks without artificial viscosity and with very low residual numerical viscosity.

3.3 Stability of Finite Difference Methods

To model an accretion flow around black holes in astrophysics, we simulate it by numerical hydrodynamic calculations. We select a Eulerian grid-based finite difference method called the Total Variation Diminishing (TVD) scheme. In the course of calculations, three important things are: the time step (δt), the grid size (δr or δz) and the boundary and initial conditions.

3.3.1 Time Step

The *Courant condition* for the time step δt given as

$$\delta t \leq \frac{\delta x}{(a + |v|)},$$

should be satisfied everywhere. This is a necessary but not a sufficient condition.

3.3.2 Grid size

Grid sizes δr or δz are decided by consideration of space resolution for the difference equations. Too coarse δr results in unjustifiable solutions due to its resolution and too small δr or δz accumulates truncation errors in a long run of the simulation. So, appropriate grid sizes are important. It is obvious that the grid size is related to time step through the Courant condition.

3.3.3 Initial and Boundary Conditions

It is important to impose appropriate initial conditions. Unless this is done carefully, the simulation may lead to non-physical or unexpected results. Boundary conditions also play a significant role in obtaining the right solutions. In our case, the accretion flows onto black holes, the inner boundary conditions must be specified at the position of the last stable orbit of the black hole. But since for all the cases we do not know the details at the boundary, the boundary conditions are eventually given approximately or speculatively.

3.4 Flux Jacobians for Equations for Inviscid Flows

The first step in determining the eigensystem of the above conservation, Eqs. 3.12, is to derive the corresponding Jacobian or transformation matrix that can be found by taking partial derivatives of the flux vector components F_i with respect to the flow vector components q_j after expressing the flux vector solely in terms of the flow vector. So, we take the following transformations (Chung 2002):

$$q = \begin{pmatrix} \rho \\ \rho v_r \\ \rho v_\theta \\ \rho v_z \\ E \end{pmatrix} = \begin{pmatrix} \rho \\ l \\ m \\ n \\ e \end{pmatrix} = \begin{pmatrix} q_1 \\ q_2 \\ q_3 \\ q_4 \\ q_5 \end{pmatrix} \text{(say)} \tag{3.21}$$

Now, after some simple algebra, the sum of the two flux functions is given as

$$F = \begin{pmatrix} \rho v_r \\ \rho v_r^2 + p \\ \rho v_\theta v_r \\ \rho v_z v_r \\ (E+p)v_r \end{pmatrix} = \begin{pmatrix} l \\ l^2 + p \\ \frac{lm}{\rho} \\ \frac{ln}{\rho} \\ \frac{(p+e)l}{\rho} \end{pmatrix} = \begin{pmatrix} F_1 \\ F_2 \\ F_3 \\ F_4 \\ F_5 \end{pmatrix} \text{(say)}. \tag{3.22}$$

Hence, the Jacobian Matrix is given as

$$\begin{pmatrix} \frac{\partial F_1}{\partial q_1} & \frac{\partial F_1}{\partial q_2} & \frac{\partial F_1}{\partial q_3} & \frac{\partial F_1}{\partial q_4} & \frac{\partial F_1}{\partial q_5} \\ \frac{\partial F_2}{\partial q_1} & \frac{\partial F_2}{\partial q_2} & \frac{\partial F_2}{\partial q_3} & \frac{\partial F_2}{\partial q_4} & \frac{\partial F_2}{\partial q_5} \\ \frac{\partial F_3}{\partial q_1} & \frac{\partial F_3}{\partial q_2} & \frac{\partial F_3}{\partial q_3} & \frac{\partial F_3}{\partial q_4} & \frac{\partial F_3}{\partial q_5} \\ \frac{\partial F_4}{\partial q_1} & \frac{\partial F_4}{\partial q_2} & \frac{\partial F_4}{\partial q_3} & \frac{\partial F_4}{\partial q_4} & \frac{\partial F_4}{\partial q_5} \\ \frac{\partial F_5}{\partial q_1} & \frac{\partial F_5}{\partial q_2} & \frac{\partial F_5}{\partial q_3} & \frac{\partial F_5}{\partial q_4} & \frac{\partial F_5}{\partial q_5} \end{pmatrix}.$$

After calculating all the partial derivatives and transformation of variables, the final Jacobian Matrix is given as

$$\begin{pmatrix} 0 & 1 & 0 & 0 & 0 \\ \frac{(\gamma-3)}{2}{v_r}^2 + \frac{(\gamma-1)}{2}({v_\theta}^2 + {v_z}^2) & (3-\gamma)v_r & (1-\gamma)v_\theta & ((1-\gamma)v_z & (\gamma-1) \\ -v_r v_\theta & v_y & v_r & 0 & 0 \\ -v_r v_z & v_z & 0 & v_r & 0 \\ K_1 & K_2 & (1-\gamma)v_r v_\theta & (1-\gamma)v_r v_z & \gamma v_r \end{pmatrix},$$

where,

$$K_1 = -\frac{\gamma p v_r}{\rho(\gamma-1)} - \frac{\gamma v_r}{2}(v_r^2 + v_\theta^2 + v_z^2) + (\gamma-1)v_r(v_r^2 + v_\theta^2 + v_z^2),$$

and

$$K_2 = \frac{\gamma p}{\rho(\gamma - 1)} + \frac{\gamma}{2}(v_r^2 + v_\theta^2 + v_z^2) + \frac{(1-\gamma)}{2}(v_r^2 + v_\theta^2 + v_z^2).$$

This is a nonlinear hyperbolic system of conservation laws as the determinant of the Jacobian matrix has a positive real value. As soon as we get the Jacobian matrix for the system, our problem becomes an eigenvalue problem. In the following section, we give the details of our solution procedure.

The system of equations presented previously can be solved numerically by replacing the partial derivatives by finite differences on a discrete numerical grid, and then advancing the solution in time via some time-marching algorithm. The following sections describe the numerical schemes, mainly those based on finite differences, specifically designed to solve nonlinear hyperbolic systems of conservation laws.

3.4.1 Eigenvalues and Eigenvectors of the Jacobian matrix

The eigenvalues of the transformation matrix $[A]$(say) are the roots λ_i of the characteristic equation

$$\det([A] - [\lambda I]) = 0, \tag{3.23}$$

where $[I]$ is the identity matrix. It turns out that three eigenvalues are distinct and two are repeated :

$$\begin{aligned}
\lambda_1 &= v_r - \sqrt{\frac{\gamma p}{\rho}},\\
\lambda_2 &= v_r,\\
\lambda_3 &= v_r,\\
\lambda_4 &= v_r,\\
\lambda_5 &= v_r + \sqrt{\frac{\gamma p}{\rho}}.
\end{aligned}$$

Here, sound speed $a = \sqrt{\frac{\gamma p}{\rho}}$.

Each right eigenvector $\mathbf{R_i}$, corresponding to eigenvalue λ_i, must satisfy the following matrix equation:

$$[A]\mathbf{R_i} = \lambda_i \mathbf{R_i}. \tag{3.24}$$

Thus, the corresponding right eigenvectors are

$$\mathbf{R_1} = \begin{pmatrix} 1 \\ v_r - a \\ v_\theta \\ v_z \\ H - v_r a \end{pmatrix},$$

$$\mathbf{R_2} = \begin{pmatrix} 0 \\ 0 \\ 1 \\ 0 \\ v_\theta \end{pmatrix},$$

$$\mathbf{R_3} = \begin{pmatrix} 1 \\ v_r \\ v_\theta \\ v_z \\ \frac{(v_r^2+v_\theta^2+v_z^2)}{2} \end{pmatrix},$$

$$\mathbf{R_4} = \begin{pmatrix} 0 \\ 0 \\ 0 \\ 1 \\ v_z \end{pmatrix},$$

$$\mathbf{R_5} = \begin{pmatrix} 1 \\ v_r + a \\ v_\theta \\ v_z \\ H + v_r a \end{pmatrix},$$

where, $H = \frac{(E+p)}{\rho}$ is the enthalpy.

The left eigenvectors which are orthonormal to the right eigenvectors are obtained by the relation:

$$\mathbf{L_i}.[A] = \lambda_i \mathbf{L_i}. \tag{3.25}$$

Thus, the set of left eigenvectors can be determined from the inverse of the right eigenvector matrix, $[L] = [R]^{-1}$. So, the left eigenvectors are as follows:

$$\mathbf{L_1} = \begin{pmatrix} \frac{\frac{(\gamma-1)\ominus}{2} + a v_r}{2a^2} \\ -\frac{(\gamma-1)v_r + a}{2a^2} \\ -\frac{(\gamma-1)v_\theta}{2a^2} \\ -\frac{(\gamma-1)v_z}{2a^2} \\ \frac{(\gamma-1)}{2a^2} \end{pmatrix},$$

$$\mathbf{L_2} = \begin{pmatrix} -v_\theta \\ 0 \\ 1 \\ 0 \\ 0 \end{pmatrix},$$

$$\mathbf{L_3} = \begin{pmatrix} 1 - \frac{(\gamma-1)\ominus}{2a^2} \\ \frac{(\gamma-1)v_r}{a^2} \\ \frac{(\gamma-1)v_\theta}{a^2} \\ \frac{(\gamma-1)v_z}{a^2} \\ -\frac{\gamma-1}{a^2} \end{pmatrix},$$

$$\mathbf{L_4} = \begin{pmatrix} -v_z \\ 0 \\ 0 \\ 1 \\ 0 \end{pmatrix},$$

$$\mathbf{L_5} = \begin{pmatrix} \frac{(\gamma-1)\ominus}{2} - a v_r \\ \hline 2a^2 \\ -\frac{(\gamma-1)v_r - a}{2a^2} \\ -\frac{(\gamma-1)v_\theta}{2a^2} \\ -\frac{(\gamma-1)v_z}{2a^2} \\ \frac{(\gamma-1)}{2a^2} \end{pmatrix},$$

where, $\ominus = (v_r^2 + v_\theta^2 + v_z^2)$. So, we calculated the eigenvalues and the corresponding eigenvectors (left and right) of the Jacobian Matrix. The details of the numerical method to solve the eigensystem is given in the following section. For this purpose, we have used a Eulerian grid-based finite difference method known as the TVD method. We discuss the TVD now.

3.4.2 Total Variation Diminishing Scheme

In the applied numerical formulation, the *NS equations* are discretized and solved in time using first-order accurate explicit time marching. The physical fluxes **F** are summed over all finite volume elements at each time level. A set of corrective eigenfluxes, closely tied to the eigensystem of the inviscid *Euler equations*, is further added to the discretized equations to assure the stability of the numerical scheme. One of the important methods to solve numerically the partial differential equations is the finite difference method. It is noted that their presence renders the overall discretization TVD.

Ami Harten (1983) published an important paper which became the basis of research in CFD. Under the title High Resolution Schemes for Hyperbolic Conservation Laws, Harten introduced the term total variation non-increasing (TVNI), which was later shortened by other researchers to TVD. In systems described by partial differential equations, such as the following hyperbolic advection equation:

$$\frac{\partial u}{\partial t} + k\frac{\partial u}{\partial x} = 0, \tag{3.26}$$

the total variation (TV) is given as

$$TV = \int |\frac{\partial u}{\partial x}| dx, \tag{3.27}$$

and the TV for the discrete case is

$$TV = \sum |(u_{j+1} - u_j)|. \tag{3.28}$$

A numerical method is said to be TVD if

$$TV(u^{n+1}) \leq TV(u^n), \tag{3.29}$$

where, n is the notation for time iteration scheme.

The TVD property implies, both physically and numerically, that the amount of variation present within a solution at any time is limited by its initial and boundary conditions. Harten (1983) described the application of his scheme to the set of one-dimensional hydrodynamic equations in Cartesian geometry and presented some tests including shock capturing. It is an explicit, second-order accurate scheme which is designed to solve a hyperbolic system of the conservation equations, like the system of the hydrodynamic conservation equations. It is a nonlinear scheme obtained by first modifying the flux function and then applying a non-oscillatory first-order accurate scheme to get a resulting second-order accuracy. The key merit of this scheme is to achieve high resolution of a second-order accuracy, while preserving the robustness of a non-oscillatory first-order scheme.

3.4.3 Characteristics of TVD

We now describe a nonlinear second-order accurate TVD scheme which builds upon the first-order monotone upwind scheme described in the previous section. The second-order accurate fluxes $F^t_{n+1/2}$ at cell boundaries are obtained by taking first-order fluxes $F^{(1),t}_{n+1/2}$ from the upwind scheme and modifying it with a second-order correction. First, consider the case where the advection velocity is positive. The first-order upwind flux $F^{(1),t}_{n+1/2}$ comes from the averaged flux F^t_n in cell n. We can define two second-order flux corrections

$$\Delta F^{L,t}_{n+1/2} = \frac{F^t_n - F^t_{n-1}}{2}, \Delta F^{R,t}_{n+1/2} = \frac{F^t_{n+1} - F^t_n}{2}, \tag{3.30}$$

using three local cell-centred fluxes. We use cell n and the cells immediately left and right of it. If the advection velocity is negative, the first-order upwind flux comes from the averaged flux F^t_{n+1} in cell $n + 1$. In this case, the second-order flux corrections

$$\Delta F^{L,t}_{n+1/2} = -\frac{F^t_{n+1} - F^t_n}{2}\,,\ \Delta F^{R,t}_{n+1/2} = -\frac{F^t_{n+2} - F^t_{n+1}}{2}\,, \tag{3.31}$$

are based on cell $n+1$ and the cells directly adjacent to it. Near extrema where the corrections have opposite signs, we impose no second-order correction and the flux assignment scheme reduces to first-order. A flux limiter ϕ is then used to determine the appropriate second-order correction

$$\Delta F^t_{n+1/2} = \phi\left(\Delta F^{L,t}_{n+1/2}, \Delta F^{R,t}_{n+1/2}\right), \tag{3.32}$$

which still maintains the TVD condition. The second-order correction is added to the first-order fluxes to get second-order fluxes. The first-order upwind scheme and second-order TVD scheme are referred to as *monotone upwind schemes for conservation laws* (MUSCL).

Time integration is performed using a second-order Runge-Kutta scheme. So, first do a half-time step,

$$u^{t+\Delta t/2}_n = u^t_n - \left(\frac{F^t_{n+1/2} - F^t_{n-1/2}}{\Delta x}\right)\frac{\Delta t}{2}\,, \tag{3.33}$$

using the first-order upwind scheme to obtain the half-step values $u^{t+\Delta t/2}$. A full time step is then computed as

$$u^{t+\Delta t}_n = u^t_n - \left(\frac{F^{t+\Delta t/2}_{n+1/2} - F^{t+\Delta t/2}_{n-1/2}}{\Delta x}\right)\Delta t\,, \tag{3.34}$$

using the TVD scheme on the half-step fluxes $F^{t+\Delta t/2}$.

3.4.4 Linearization of the Nonlinear Problem

Instead of solving the nonlinear problem, Roes approximate Riemann solver (Roe 1981) solves a linearized version of the problem. The Roes solver is one of the most widely used methods because of its proven accuracy and low numerical dissipation. The latter property of Roes method is known to play an important role in resolving the boundary layer, for which excessive numerical dissipation can ruin the solution accuracy. In the TVD scheme which is based on the Eulerian grid, the flux is computed on the grid boundary, while the physical quantity is defined in the grid centre. We use the Roe approximation Riemann solution to get the averaged values of the physical quantities at the grid boundary:

$$v_{r,i+\frac{1}{2}} = \frac{\sqrt{\rho}_i v_{r,i} + \sqrt{\rho}_{i+1} v_{r,i+1}}{\sqrt{\rho}_i + \sqrt{\rho}_{i+1}}, \tag{3.35}$$

$$v_{\theta,i+\frac{1}{2}} = \frac{\sqrt{\rho}_i v_{\theta,i} + \sqrt{\rho}_{i+1} v_{\theta,i+1}}{\sqrt{\rho}_i + \sqrt{\rho}_{i+1}}, \tag{3.36}$$

$$v_{z,i+\frac{1}{2}} = \frac{\sqrt{\rho}_i v_{z,i} + \sqrt{\rho}_{i+1} v_{z,i+1}}{\sqrt{\rho}_i + \sqrt{\rho}_{i+1}}, \tag{3.37}$$

$$H_{i+\frac{1}{2}} = \frac{\sqrt{\rho}_i H_i + \sqrt{\rho}_{i+1} H_{i+1}}{\sqrt{\rho}_i + \sqrt{\rho}_{i+1}}, \tag{3.38}$$

$$a_{i+\frac{1}{2}} = \left\{ (\gamma - 1) \left[H_{i+\frac{1}{2}} - \frac{1}{2} \left(v^2_{r,i+1} + v^2_{\theta,i+1} + v^2_{z,i+1} \right) \right] \right\}^{\frac{1}{2}}. \tag{3.39}$$

3.5 Viscous Accretion Flows

Until now, we have ignored viscosity. The most common astrophysical application of viscosity is the accretion disc, so we introduce viscosity specifically to study viscous evolution of accretion discs. We show how we introduce viscosity into the grid-based finite difference method (Molteni et al. 1996). It has been found experimentally that the magnitude of the shear stress in viscous flows is often proportional to the symmetric components of the velocity gradient. This is analogous to Hookes law. The component of the stress tensor due to viscosity is written as (Landau and Lifshitz 1959)

$$\tau_{visc} = -\zeta \theta \mathbf{g} - 2\eta\sigma,$$

and there is no force if the fluid is simply rotating, so no dependence on r. The first coefficient, ζ, is known as the bulk viscosity and is important in compressible flows. The second term, η, is sometimes called the shear viscosity. Bulk viscosity is often neglected in astrophysical flows except when considering the structure of shocks. Both bulk and shear viscosities are often assumed to be independent of position and temperature.

In an inertial frame of reference, revisiting Eq. 1.23, the general form of the equations of the flow (Batchelor 1967) is

$$\rho \left[\frac{\partial \mathbf{v}}{\partial t} + \mathbf{v}.\nabla \mathbf{v} \right] = -\nabla P + \mathbf{F_b} + \nabla.\tau, \tag{3.40}$$

where, $\mathbf{v}$ is the flow velocity, ρ is the fluid density, P is the pressure, τ is the stress tensor and $\mathbf{F_b}$ represents body forces (per unit volume) acting on the fluid and ∇ is

the Del operator. Typically, the body forces consist of only gravity forces, but may include other types (such as electromagnetic forces). Here τ is the viscous stress (or shear stress) having six mutually independent components. The six independent components of the viscous stress tensor (Landau and Lifshitz 1959) are listed here in cylindrical coordinates, τ_{rr}, $\tau_{r\phi}$, τ_{rz}, $\tau_{\phi\phi}$, $\tau_{\phi z}$ and τ_{zz}.

3.6 Comparison Between Non-viscous and Viscous Equations

3.6.1 Non-viscous Equations in General Form

It is our interest to re-split the equations written in compact form in Eq. 3.5. The second, third and fourth rows of the matrix give us the v_r, v_ϕ and v_z components of momentum equations, respectively. Hence, re-splitting the v_ϕ component, we have

$$\frac{\partial}{\partial t}(\rho v_\phi) + \frac{1}{r}\frac{\partial}{\partial r}(r\rho v_\phi v_r) = -\frac{\rho v_\phi v_r}{r},$$

$$\Rightarrow \rho\frac{\partial v_\phi}{\partial t} + v_\phi\frac{\partial \rho}{\partial t} + \frac{\rho}{r}\left[r\frac{\partial}{\partial r}(v_\phi v_r) + v_\phi v_r\right] = -\frac{\rho v_\phi v_r}{r},$$

$$\Rightarrow \rho\frac{\partial v_\phi}{\partial t} + v_\phi\frac{\partial \rho}{\partial t} + \frac{\rho}{r}\left[r v_r\frac{\partial v_\phi}{\partial r} + r v_\phi\frac{\partial v_r}{\partial r} + v_\phi v_r\right] = -\frac{\rho v_\phi v_r}{r},$$

$$\Rightarrow \rho\frac{\partial v_\phi}{\partial t} + \rho v_r\frac{\partial v_\phi}{\partial r} + \left[v_\phi\frac{\partial \rho}{\partial t} + \rho v_\phi\frac{\partial v_r}{\partial r} + \frac{\rho v_\phi v_r}{r}\right] = -\frac{\rho v_\phi v_r}{r}. \tag{3.41}$$

Meanwhile, re-splitting the first row of Eq. 3.12 (i.e. the continuity equation) it becomes

$$\frac{\partial \rho}{\partial t} + \frac{1}{r}\frac{\partial}{\partial r}(r\rho v_r) = 0,$$

$$\Rightarrow \frac{\partial \rho}{\partial t} + \frac{\rho}{r}r\frac{\partial v_r}{\partial r} + \frac{\rho}{r}v_r = 0. \tag{3.42}$$

Multiplying by v_ϕ both sides of Eq. 3.42, we have

$$v_\phi\frac{\partial \rho}{\partial t} + \rho v_\phi\frac{\partial v_r}{\partial r} + \frac{\rho v_\phi v_r}{r} = 0. \tag{3.43}$$

Hence from Eqs. 3.41 and 3.43 we get

$$\rho\frac{\partial v_\phi}{\partial t} + \rho v_r\frac{\partial v_\phi}{\partial r} = -\frac{\rho v_\phi v_r}{r}. \tag{3.44}$$

3.6.2 Viscous Equations in General Form

If we split all the viscous stress tensors, three components of Eq. 3.40 take the following forms (Landau and Lifshitz 1959 and Acheson 1990). The v_r component of *NS equations* is given as

$$\rho\left[\frac{\partial v_r}{\partial t}+v_r\frac{\partial v_r}{\partial r}+\frac{v_\phi^2}{r}+\frac{v_\phi}{r}\frac{\partial v_r}{\partial \phi}+v_z\frac{\partial v_r}{\partial z}\right]=-\frac{\partial P}{\partial r}+\mu\left[\frac{\partial^2 v_r}{\partial r^2}+\frac{1}{r}\frac{\partial v_r}{\partial r}-\frac{v_r}{r^2}+\frac{1}{r^2}\frac{\partial^2 v_r}{\partial \phi^2}+\frac{\partial^2 v_r}{\partial z^2}-\frac{2}{r^2}\frac{\partial v_\phi}{\partial \phi}\right]+F_r. \tag{3.45}$$

Again, the v_ϕ component is given as

$$\rho\left[\frac{\partial v_\phi}{\partial t}+v_r\frac{\partial v_\phi}{\partial r}+\frac{v_\phi v_r}{r}+\frac{v_\phi}{r}\frac{\partial v_\phi}{\partial \phi}+v_z\frac{\partial v_\phi}{\partial z}\right]=-\frac{1}{r}\frac{\partial P}{\partial \phi}+\mu\left[\frac{\partial^2 v_\phi}{\partial r^2}+\frac{1}{r}\frac{\partial v_\phi}{\partial r}-\frac{v_\phi}{r^2}+\frac{1}{r^2}\frac{\partial^2 v_\phi}{\partial \phi^2}+\frac{\partial^2 v_\phi}{\partial z^2}+\frac{2}{r^2}\frac{\partial v_\phi}{\partial \phi}\right]+F_\phi. \tag{3.46}$$

Finally, the v_z component is given as

$$\rho\left[\frac{\partial v_z}{\partial t}+v_r\frac{\partial v_z}{\partial r}+\frac{v_\phi}{r}\frac{\partial v_z}{\partial \phi}+v_z\frac{\partial v_z}{\partial z}\right]=-\frac{\partial P}{\partial z}+\mu\left[\frac{\partial^2 v_z}{\partial r^2}+\frac{1}{r}\frac{\partial v_z}{\partial r}+\frac{1}{r^2}\frac{\partial^2 v_z}{\partial \phi^2}+\frac{\partial^2 v_z}{\partial z^2}\right]+F_z, \tag{3.47}$$

where μ is the dynamic viscosity defined as $\mu=\eta\rho$ and η is called the kinematic viscosity. Here, F_r, F_ϕ & F_z are the so-called body forces. The only body force present in our system is gravitational force. Thus, $F_\phi=\rho G_\phi$, $F_r=\rho G_r$ and $F_z=\rho G_z$, where G_ϕ, G_r and G_z are the components of acceleration due to gravity, namely

$$G_r=-\frac{1}{2(R-1)^2}\frac{r}{R},$$

and

$$G_z=-\frac{1}{2(R-1)^2}\frac{z}{R},$$

where, $R=\sqrt{r^2+z^2}$. For the axisymmetric case, $G_\phi=0$ and thus, $F_\phi=0$. As we have chosen the axisymmetric case, we have neglected $\frac{\partial}{\partial \phi}$ added terms. So the above equations reduce as follows:

Equation 3.45 reduces to

$$\rho\left[\frac{\partial v_r}{\partial t}+v_r\frac{\partial v_r}{\partial r}+v_z\frac{\partial v_r}{\partial z}\right]=-\frac{\partial P}{\partial r}-\frac{v_\phi^2}{r}+\mu\left[\frac{\partial^2 v_r}{\partial r^2}+\frac{1}{r}\frac{\partial v_r}{\partial r}-\frac{v_r}{r^2}+\frac{\partial^2 v_r}{\partial z^2}\right]+\rho G_r. \tag{3.48}$$

Equation 3.46 takes the form

$$\rho\left[\frac{\partial v_\phi}{\partial t}+v_r\frac{\partial v_\phi}{\partial r}+v_z\frac{\partial v_\phi}{\partial z}\right]=-\frac{v_\phi v_r}{r}+\mu\left[\frac{\partial^2 v_\phi}{\partial r^2}+\frac{1}{r}\frac{\partial v_\phi}{\partial r}-\frac{v_\phi}{r^2}+\frac{\partial^2 v_\phi}{\partial z^2}\right]. \tag{3.49}$$

Equation 3.47 reduces to

$$\rho\left[\frac{\partial v_z}{\partial t}+v_r\frac{\partial v_z}{\partial r}+v_z\frac{\partial v_z}{\partial z}\right]=-\frac{\partial P}{\partial z}+\mu\left[\frac{\partial^2 v_z}{\partial r^2}+\frac{1}{r}\frac{\partial v_z}{\partial r}+\frac{\partial^2 v_z}{\partial z^2}\right]+\rho G_z. \tag{3.50}$$

3.6.3 The Viscous Term

In case of a thin accretion flow, it is customary to use only $\tau_{r\phi}$ component since it is the dominant contributor to the viscous stress (Shakura and Sunyaev 1973). This is responsible for transporting angular momentum along the radial direction. The other components are assumed negligible. Thus, considering only $\tau_{r\phi}$, the only viscous term which goes into Eq. 3.49 is

$$\mu\left[\frac{\partial^2 v_\phi}{\partial r^2}+\frac{1}{r}\frac{\partial v_\phi}{\partial r}-\frac{v_\phi}{r^2}\right]=\frac{1}{r^2}\frac{\partial}{\partial r}(r^2\tau_{r\phi}), \tag{3.51}$$

where,

$$\tau_{r\phi}=\mu r\frac{\partial\Omega}{\partial r}.$$

Here, Ω is angular velocity and defined as

$$\Omega=\frac{v_\phi}{r}.$$

The difference between Eqs. 3.44 and 3.49 is that the latter has an extra term

$$\mu\left[\frac{\partial^2 v_\phi}{\partial r^2}+\frac{1}{r}\frac{\partial v_\phi}{\partial r}-\frac{v_\phi}{r^2}\right] \tag{3.52}$$

which is the viscous term of tangential momentum component of *NS equations*. To obtain viscous disc solution, this term is included into the inviscid system.

3.6.4 The Viscous Term in Various Forms

We can express the viscous term in different ways. We can write this term as

$$\frac{1}{r^2}\frac{\partial}{\partial r}(r^2\tau_{r\phi}), \tag{3.53}$$

where,

$$\tau_{r\phi} = \mu r\frac{\partial \Omega}{\partial r}. \tag{3.54}$$

Here, Ω is angular velocity and is defined as

$$\Omega = \frac{v_\phi}{r}. \tag{3.55}$$

Hence, in the usual form

$$\frac{1}{r^2}\frac{\partial}{\partial r}(r^2\tau_{r\phi}) = \frac{1}{r^2}\frac{\partial}{\partial r}\left[\mu r^3\frac{\partial}{\partial r}\left(\frac{v_\phi}{r}\right)\right]. \tag{3.56}$$

Hence, if we consider μ as a constant term throughout, Eq. 3.53 reduces to

$$\begin{aligned}\frac{\mu}{r^2}\frac{\partial}{\partial r}\left[r^2\frac{\partial v_\phi}{\partial r} - rv_\phi\right] &= \frac{\mu}{r^2}\left[r^2\frac{\partial^2 v_\phi}{\partial r} + 2r\frac{\partial v_\phi}{\partial r} - r\frac{\partial v_\phi}{\partial r} - v_\phi\right],\\ &= \mu\left[\frac{\partial^2 v_\phi}{\partial r^2} + \frac{1}{r}\frac{\partial v_\phi}{\partial r} - \frac{v_\phi}{r^2}\right],\end{aligned} \tag{3.57}$$

which is the same as Eq. 3.52. As the second-order term $\frac{\partial^2 v_\phi}{\partial r^2}$ is very small, one could neglect the term. Then, the viscous term reduces to

$$\mu\left(\frac{1}{r}\frac{\partial v_\phi}{\partial r} - \frac{v_\phi}{r^2}\right) = \mu\frac{\partial \Omega}{\partial r}. \tag{3.58}$$

The expression in 3.58 is basically a good approximation of 3.57. Now, we turn our focus on how to calculate the value of μ, the dynamic (kinematic) viscosity coefficient.

3.6.5 Effects of Molecular Viscosity in Accretion Flows

The kinematic viscosity η has a dimension of L^2/T, where L = length, T = time. Diffusion at the molecular level generates viscosity and is called the molecular

viscosity. Evidently, the molecular viscosity is microscopic in nature and is caused by frictious and dragging interactions of individual neighbouring particles. For molecular viscosity, the appropriate length scale, L, is the mean free path and the appropriate velocity, v, is the sound speed a (since this is the characteristic velocity of molecules in a gas). Molecular viscosity acts because the molecules in a gas have random motions that allow them to diffuse across shearing interfaces in a fluid. The effect of this is to generate friction between adjacent regions of the fluid that move relative to one another. It turns out, however, that the molecular viscosity is too small to explain the evolutionary timescales of accretion discs. We therefore need to identify possible instabilities that can cause a turbulence larger than that caused by the molecular viscosity. So, it is clear that some kind of macroscopic turbulent viscosity must be present. Although some astrophysical winds may carry away some angular momentum, it is not likely to be dominating.

3.6.6 Various Approaches to Quantify Turbulent Viscosity Based on the α Prescription

Before we go into this discussion, we present here a very successful idea of parameterizing the viscosity without identifying its source. The idea goes back to Shakura & Sunyaev (citealtbib12) who first proposed the so-called α- parameter to measure the efficiency of angular momentum transport. It has long been suspected that the diffusion of angular momentum through an accretion flow is driven by turbulence. The $SS\alpha$-model (Shakura and Sunyaev 1973) introduced a phenomenological shear stress into the equations of motion to model the effects of this turbulence. This shear stress is proportional to P. More specifically, it is assumed to be $-\alpha P$, where α is a dimensionless constant and P is the (gas or gas+radiation) pressure. This shear stress permits an exchange of angular momentum between neighbouring. We must also choose a viscosity coefficient. There are several tricks to find the value of dynamic viscosity coefficient in $SS\alpha$ prescription. Some are discussed below.

Numerically, we used the viscous term in Eq. 3.44 and it is assumed that the dynamic viscosity coefficient μ is not constant throughout the flow. For this case, generally, the standard formula for μ is given as

$$\mu = \frac{2}{3}\frac{\alpha\rho a^2}{\Omega} = \frac{2}{3}\frac{\alpha\rho a^2 r}{v_\phi}, \tag{3.59}$$

where, α is a constant of order 1 and a is adiabatic sound speed. We know $a^2 = \frac{\gamma p}{\rho}$, which implies that $\rho a^2 = \gamma p$, where γ is the adiabatic index. From Eq. 3.59, we have

$$\mu = \frac{2}{3}\frac{\alpha\gamma p r}{v_\phi}. \tag{3.60}$$

Using Eq. 3.60, the viscous term in Eq. 3.56 reduces to

$$\frac{1}{r^2}\frac{\partial}{\partial r}\left[\frac{2}{3}\frac{\alpha\gamma pr}{v_\phi}r^3\frac{\partial}{\partial r}\left(\frac{v_\phi}{r}\right)\right],$$

$$= \frac{2}{3}\frac{\alpha\gamma}{r}\left[\frac{\partial}{\partial r}\left(\frac{pr^3}{v_\phi}\frac{\partial v_\phi}{\partial r}\right) - \frac{\partial}{\partial r}(pr^2)\right],$$

$$= \frac{2}{3}\frac{\alpha\gamma}{r^2}\left[\frac{pr^3}{v_\phi}\frac{\partial^2 v_\phi}{\partial r^2} - \frac{pr^3}{v_\phi^2}\left(\frac{\partial v_\phi}{\partial r}\right)^2 + \frac{\partial v_\phi}{\partial r}\left(\frac{3r^2 p}{v_\phi} + \frac{r^3}{v_\phi}\frac{\partial p}{\partial r}\right) - \left(2rp + r^2\frac{\partial p}{\partial r}\right)\right],$$

$$= \frac{2\alpha\gamma}{3}\left[\frac{pr}{v_\phi}\frac{\partial^2 v_\phi}{\partial r^2} - \frac{pr}{v_\phi^2}\left(\frac{\partial v_\phi}{\partial r}\right)^2 + \frac{\partial v_\phi}{\partial r}\left(\frac{3p}{v_\phi} + \frac{r}{v_\phi}\frac{\partial p}{\partial r}\right) - \left(\frac{2p}{r} + \frac{\partial p}{\partial r}\right)\right]. \quad (3.61)$$

The expression in 3.61 is the viscous term for this method. It is easy to include this term in our non-viscous TVD scheme. This is a direct method.

Let, μ be constant throughout the flow. Then, one may use the viscous term Eq. in 3.53 as in Lanzafame et al. (1998). In that case, the Shakura-Sunyaev turbulent viscosity can be described by the following formula:

$$\mu = \alpha\rho a Z_{\text{disc}}, \quad (3.62)$$

where, the vertical thickness Z_{disc} is estimated from the assumption of the vertical equilibrium condition and α is a parameter of order 1.

$${Z_{\text{disc}}}^2 = \frac{2}{\gamma}ar(r-1)^2. \quad (3.63)$$

So, using Eqs. 3.62 and 3.63, we can calculate the value of μ. Replacing this value of μ into Eq. 3.52 (same as Eq. 3.57), we get the total amount of viscosity.

Let, μ be not a constant throughout the flow. Then, we can use the viscous form in 3.53. Using $SS\alpha$ prescription, we can directly put the value of $\tau_{r\phi}$ equal to $-\alpha p$ (Chakrabarti and Molteni 1995; Chakrabarti 1996). First, we can calculate the value of μ in the following way:

$$\tau_{r\phi} = -\alpha p,$$

$$\Rightarrow \mu r\frac{\partial\Omega}{\partial r} = -\frac{\alpha a^2\rho}{\gamma},$$

$$\Rightarrow \mu r\left(\frac{1}{r}\frac{\partial v_\phi}{\partial r} - \frac{v_\phi}{r^2}\right) = -\frac{\alpha a^2\rho}{\gamma},$$

$$\Rightarrow \mu = -\frac{\frac{\alpha a^2 \rho}{\gamma}}{\left(\frac{\partial v_\phi}{\partial r} - \frac{v_\phi}{r^2}\right)}. \tag{3.64}$$

Replacing this value of μ in Eq. 3.52 (as well as in Eq. 3.57), we get the viscous solution. This method could be implemented in a direct and simplified way. In Eq. 3.53 we can directly put $-\alpha p$ in the place of $\tau_{r\phi}$. In that case, the viscous term reduces to

$$\frac{1}{r^2}\frac{\partial}{\partial r}(-r^2 \alpha p)$$

$$= -\alpha\left(\frac{2p}{r} + \frac{\partial p}{\partial r}\right). \tag{3.65}$$

The expression Eq. 3.53 characterises the tangential stress between adjacent layers by a single parameter, α. This parameter carries all the uncertainties involved within it. Naturally, α is a multi-variable dependent, $\alpha = \alpha(v, r, \Omega, \Omega_K, a)$ and its physics is not known.

We can approximate Eq. 3.52 by Eq. 3.65 and it is a good estimation. Now, if we ignore $\frac{\partial^2 v_\phi}{\partial r^2}$ and $\frac{\partial v_\phi}{\partial r}$ from (3.61), we have the reduced viscous term as

$$-\frac{2\alpha\gamma}{3}\left(\frac{2p}{r} + \frac{\partial p}{\partial r}\right), \tag{3.66}$$

which can be compared to Eq. 3.65. The expression for μ in Eq. 3.65 is used throughout our simulations in this thesis when we assume that the accretion disc is thin.

3.6.7 Description of Viscosity for Thick Accretion Flows

In case of thick accretion flow, all viscous stress could be significant in flow dynamics. To perform dynamical calculation, one needs to fix a prescription for viscosity. Assuming that the flow is thick $h \sim r$, the α-prescription could be written as

$$\mu = \alpha_s \rho \frac{a^2}{\Omega_k}, \tag{3.67}$$

where, α_s is constant of order 1, a is the adiabatic sound speed and

$$\Omega_k = [\frac{1}{r}\frac{\partial \Phi}{\partial r}]^{\frac{1}{2}}. \tag{3.68}$$

is the Keplerian angular velocity. This kind of formulation has been used before (Igumenshchev et al. 1996). Using the value of μ from Eq. 3.68 in Eq. 3.57, we also get the viscous solution for thin discs. Note that for a thick disc, all the viscous stress components can have a significant contribution to transport the angular momentum of the flow in both horizontal and vertical directions. So, one can easily use the value for μ in Eq. 3.68 and it can be replaced in Eqs. 3.48, 3.49 and 3.50 and all the viscous stress components are considered.

It is to be noted that the heat generated by the viscous dissipation is assumed to be radiated away instantly. Thus, we do not consider any effect of the heating on the dynamics of the flow in the present thesis.

In the literature, viscosity prescriptions other than those discussed here have also been tried out, especially when the shock is present. We followed also the prescription MacFadyen and Woosley (1999), where α was assumed to be constant when $v_\phi > v_r$, while it is assumed to be scaled as v_ϕ / v_r in the pre-shock flow to reduce the shear. The result remains similar to our present result. This is because the pre-shock flow, where $v_\phi > v_r$ is cooler with a lower thermal pressure, and thus the angular momentum transport rate is weaker. In the post-shock flow, due to high thermal pressure, the angular momentum transport rate is higher and our disc becomes similar to Keplerian. Thus, a constant α prescription plays a role similar to that in a Keplerian disc.

3.7 Implementation of Viscosity in the Numerical Scheme

If one could find the Jacobian matrix for viscous cases, then it is easy to derive the eigenvalue values and corresponding eigenvectors. But unfortunately, it is impossible to derive the Jacobian matrix for compressible viscous flow, i.e. the *NS equations*. Also, there is no need for it. Only the inviscid part of the *NS equations* have wave character and will show instability if not modelled properly. Physical viscosity helps in that regard. We saw that the components of the viscous stress tensor, based on a cylindrical frame of reference, are determined through local velocity gradients. The local gradients of velocity and temperature are difficult to calculate unless we use a simple finite difference method. We have done this. We have implemented the viscous terms as source functions of a non-viscous system.

3.8 Energy Equation with Power-Law Cooling

Radiative processes very often play an important role in momentum and energy conservation equations. Generally, flow equations are coupled to radiative transfer equations and the stability conditions become more complicated. As far as the cooling process goes, ideally one should use Comptonization, the dominant mechanism of cooling in stellar systems. However, the process is highly nonlinear and non-local. On the other hand, the bremsstrahlung cooling which could be computed from the

local density and temperature is too weak to have any significant effect. Therefore, we choose a power-law cooling in the energy equation having a temperature dependence as T^{β}. Hence the cooling rate is $\Lambda_{\text{powcool}} \propto \rho^2 T^{\beta}$, where $\beta > 0$ is the cooling index. The energy equation becomes:

$$\frac{\partial(\rho\epsilon)}{\partial t} + \nabla.(\rho\epsilon\mathbf{v}) + \Lambda_{\text{powcool}} = 0, \tag{3.69}$$

where, $\epsilon = \frac{p\gamma}{(\gamma-1)} + (v_r^2 + v_\theta^2 + v_z^2)/2 + g$, is the specific energy, γ is the adiabatic index, ρ is the mass density. Here, Λ_{cool} is the expression for power-law cooling. So, the energy conservation equation of the last row of Eq. 3.5 becomes

$$\frac{\partial E}{\partial t} + \frac{1}{r}\frac{\partial(E+p)rv_r}{\partial r} + \frac{\partial(E+p)v_z}{\partial z} = -\frac{\rho\,(rv_r + zv_z)}{2\left(\sqrt{r^2+z^2}-1\right)^2\sqrt{r^2+z^2}} - \Lambda_{\text{powcool}}. \tag{3.70}$$

Here, energy density E (without the potential energy) is defined as $E = p/(\gamma-1) + \rho(v_r^2+v_\theta^2+v_z^2)/2$, ρ is the mass density, γ is the adiabatic index, p is the pressure, v_r, v_θ and v_z are the radial, azimuthal and vertical components of velocity, respectively. The normal bremsstrahlung cooling is obtained by taking cooling index $\beta = \frac{1}{2}$. In an electron-proton plasma, the expression for bremsstrahlung cooling process (Lang 1980) is given as

$$\Lambda_{\text{brems}} = 1.43 \times 10^{-27} N_e N_i T^{\frac{1}{2}} Z^2 g_f \text{ergcm}^{-3}\text{s}^{-1}, \tag{3.71}$$

where,

$$N_i Z = \frac{\rho}{(m_p + m_e)} \approx \frac{\rho}{m_p}, \tag{3.72}$$

i.e.

$$\Lambda_{\text{brems}} = 1.43 \times 10^{-27} \rho^2 T^{\frac{1}{2}} g_f, \tag{3.73}$$

where, m_p is the mass of proton, T is the temperature, g_f is the Gaunt factor. In our work, to increase the cooling efficiency, we have taken the cooling index $\beta = 1$. Other constants are as in Eq. 3.60. So the cooling term in Eq. 3.59 reduces to

$$\Lambda_{\text{powcool}} = 1.43 \times 10^{-27} \rho^2 T g_f, \tag{3.74}$$

where, everything is expressed in the CGS units and g_f is the Gaunt factor which is assumed to be 1.0 in our work. The temperature T can be easily obtained from the density (ρ) and pressure (p) calculated in our simulation. Using the ideal gas equation, we get for temperature T

$$T = \frac{p}{\rho}\frac{\mu m_p}{k_b}, \tag{3.75}$$

where, k_b is the Boltzmann constant. We assume $\mu = 0.5$ for purely hydrogen gas.

References

Acheson, D. J. (1990). *Elementary fluid dynamics. Oxford appliedmMathematics and computing science series*. Oxford: Oxford University Press.
Batchelor, G. K. (1967). *An introduction to fluid dynamics*. Cambridge: Cambridge University Press.
Chakrabarti, S. K. (1990). *Theory of transonic astrophysical flows*. Singapore: World Scientific.
Chakrabarti, S. K. (1996). *Physics Reports*, *266*, 229.
Chakrabarti, S. K., & Molteni, D. (1995). *MNRAS*, *80*, 272.
Chung, T. J. (2002). *Computational fluid dynamics*. Cambridge: Cambridge University Press.
Harten, A. (1983). *Journal of Computational Physics*, *49*, 357.
Igumenshchev, I. V., Chen, X., & Abramowicz, M. A. (1996). *MNRAS*, *278*, 236.
Landau, L. D., & Lifshitz, E. M. (1959). *Fluid Mechanics*. Oxford: Pergamon Press.
Lanzafame, G., Molteni, D., & Chakrabarti, S. K. (1998). *MNRAS*, *299*, 799.
MacFadyen, A. I., & Woosley, S. E. (1999). *Astrophysics Journal*, *524*, 262.
Molteni, D., Ryu, D., & Chakrabarti, S. K. (1996). *Astrophysics Journal*, *470*, 460.
Paczyński, B., & Wiita, P. J. (1980). *Astronomy and Astrophysics*, *88*, 23.
Roe, P. L., & Roe, P. L. (1981). *Journal of Computational Physics*, *43*, 357.
Shakura, N. I., & Sunyaev, R. A. (1973). *Astronomy and Astrophysics*, *24*, 337.

Chapter 4
Simulation Procedure and the Test of the Code

Abstract We point out the procedure of simulation and computational box in detail. We study the accretion processes on a black hole by numerical simulation. We use a grid-based finite difference code for this purpose. Tests of the code are made using the flow without angular momentum, namely the Bondi flow.

A true accretion disc is indeed a complex, three-dimensional and time-dependent flow which also contains viscous and radiative effects. However, we start with the most simple case and slowly add more physics to make it realistic. However, we always assume an axisymmetric flow and consider the behaviour in the meridional plane (x–z plane). Thus essentially the flow is two-dimensional. We first ignore viscous and radiative effects and the system reduces to a time-dependent inviscid flow; the set of equations for this system are given in Eq. (3.12) in a dimensionless compact form. Subsequently, we also include viscosity and cooling in our code. Once a simulation procedure is built up for the non-viscous part, it is easy to modify this for viscous and radiative parts. In this chapter, we discuss the simulation procedure and check the validity of our code with a test case.

4.1 Simulation Procedure

We numerically solve the set of hydrodynamic equations shown in Eq. (3.12) using an explicit–implicit finite difference scheme on the Eulerian grids. Our methods and boundary conditions are similar to those of Molteni et al. (1996) and Ryu et al. (1997), but we adopt a different injection and boundary conditions and carry out long-time calculations to examine a quasi-steady structure of the accretion disc. We calculate the flow dynamics in two dimensions using a finite difference method which uses the principle of Total Variation Diminishing (TVD) described in Chap. 3 to carry out hydrodynamic simulations.

4.1.1 Geometry Used for Our Simulations

To model the initial injection of matter, we consider an axisymmetric flow of gas in the Pseudo-Newtonian gravitational field of a black hole of mass M_{bh} located at

K. Giri, *Numerical Simulation of Viscous Shocked Accretion Flows Around Black Holes*,
Springer Theses, DOI 10.1007/978-3-319-09540-0_4

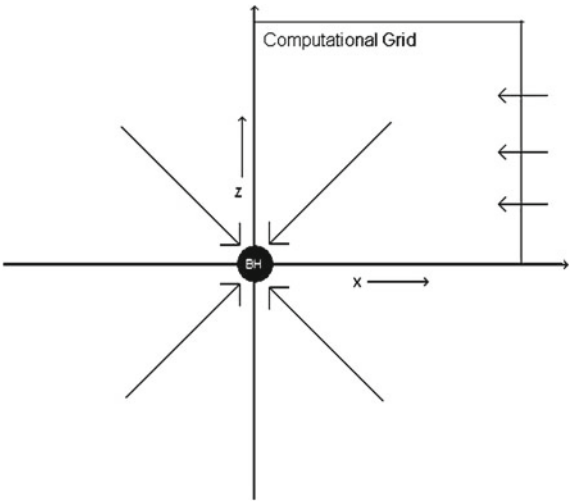

Fig. 4.1 Schematic diagram of our computational *box*

the centre in the cylindrical coordinates $[r, \theta, z]$. We assume that at infinity, the gas pressure is negligible and the energy per unit mass vanishes. As mentioned before, the gravitational field of the black hole can be described by Paczyński and Wiita (1980) potential. The ambient matter which is falling towards a black hole can come from any direction towards a black hole. But for simplicity, we simulate the accretion flow in only the first quadrant of the box. Taking the reflection symmetry along r and z directions, we can obtain the flows in the other three quadrants. In Fig. 4.1, the computation box is shown. The center of the black hole coincides with the origin. The matter that enters (denoted with arrow sign) into the computational box is the incoming matter at the outer boundary.

4.1.2 Computational Box and Initial Conditions

The computational box occupies one quadrant of the $r-z$ plane with $0 \leq r \leq r_o$ and $0 \leq z \leq r_o$, where r_o is assumed as the radius of the outer boundary where matter is being injected. We mimic the horizon ($r = 1$) by placing an absorbing boundary at a sphere of radius r_i inside which all the material is completely absorbed. In our simulations, r_i varies from 1.5 to $2.5\, r_g$ depending on the number of grids employed and the resolution of the simulation. To begin the simulation, we fill in the black hole surroundings with a very tenuous plasma of density $\rho_{bg} = 10^{-6}$ and the temperature as that of the incoming material. The incoming gas of density $\rho_{in} = 1$ enters the box through the outer boundary located at $r = r_o$. We have chosen the density of the incoming gas $\rho_{in} = 1$ for convenience since, in the absence of self-gravity and cooling, the density is scaled out, rendering the simulation results to be valid for any accretion rate. Of course, this initial condition is totally washed out and replaced

by the incoming matter in a dynamical timescale. Initially, the values of radial (v_r), rotational (v_ϕ) and azimuthal (v_z) components are all chosen as zero for all the grids except those on the outer boundary. Thus, the Mach number is zero everywhere at the beginning of the simulation except at the outer boundary.

The adiabatic index $\gamma = 4/3$ is chosen. In the absence of self-gravity and cooling, the density is scaled out, and thus the simulation results remain valid for any accretion rate. All the calculations have been done with $N_r \times N_z$ cells. Here, N_r is the number of grids we have chosen in radial direction while N_z represent the same in vertical direction. In all our cases, we have chosen $N_r = N_z$. Thus, each grid size is $\Delta r = \Delta z = r_o/N_r = r_o/N_z$.

4.1.3 Comments on Parameters and Assumptions

The black hole mass M_{bh}, the speed of light c and the Schwarzschild radius r_g are assumed to be the units of the mass, velocity and length, respectively. We use $r = R/r_g$, and $z = Z/r_g$ as the dimensionless distances along r-axis and z-axis in the rest of the chapter. We also assume a polytropic equation of state for the accreting (or, outflowing) matter, $P = K\rho^\gamma$, where P and ρ are the isotropic pressure and the matter density, respectively, γ is the adiabatic index (assumed in this paper to be constant throughout the flow, and is related to the polytropic index n by $\gamma = 1+1/n$) and K is related to the specific entropy of the flow. Since we ignore dissipation, the specific angular momentum $\lambda \equiv r v_\theta$ is constant everywhere.

4.1.4 Boundary Conditions

We use a simple continuous condition at the outer boundary for outflows in which all the derivatives of fluid quantities were set to be zero at the boundaries. We found that even with the simple continuous condition, reflection at the boundary was kept at a minimum and did not affect the structure formed along the equatorial plane. Along the symmetry axis ($r = 0$) and the equatorial plane ($z = 0$), the reflecting condition was used.

As we consider only constant energy flows while keeping the boundary of the numerical grid at a finite distance, we need the radial velocity v_r, sound speed a (i.e. temperature) of the flow and the incoming velocity at the boundary points. This assumption implies that for a given specific angular momentum, v_r and a are not independent but are related by the following condition:

$$\mathcal{E} = \frac{v_r^2}{2} + \frac{a^2}{\gamma - 1} + \frac{\lambda^2}{2r^2} + g(r) = 0, \tag{4.1}$$

with negligible v_z. Here, $g(r)$ is radial force potential, which in the pseudo-Newtonian model takes the form:

$$g(r) = -\frac{1}{2}(r-1)^{-1}, \tag{4.2}$$

where, v_r and a are the dimensionless radial and sound velocities and r is non-dimensional radial distance.

4.1.5 Comments on Timescales

Keeping these in mind, we choose $2G = c = M = 1$, where, M is the solar mass, c the velocity of light and G the gravitational constant. In this case, the unit of velocity would be c, the unit of distance would be $2\,GM/c^2$ (the Schwarzschild radius), the unit of time would be $2\,GM/c^3$ and the unit of angular momentum would be $2\,GM/c$. All the simulations are carried out assuming a stellar mass black hole ($M = 10M_{\odot}$). The results remain equally valid for massive/supermassive black holes, only the time and length are to be scaled with the central mass. We carry out the simulations till several thousands of dynamical timescales are passed. In reality, this corresponds to a few seconds in physical units. Once the system relaxes to an approximate steady-state, the overall structure remains unchanged although there are still changes in the detailed structure.

4.2 Comments on Code Parameters

While the model parameters discussed above describe the physical state of the initial conditions, another set of parameters which may affect the simulations is that of code parameters, which determine the details of the numerical simulation method. These parameters are included into the code with their nominal values. Ideally, if the values chosen for the code parameters are sufficient to yield accurate simulations, the resulting simulations will be insensitive to variations in the code parameters. To test whether the simulations are accurate, several test models have been numerically evolved, each with the value of a single code parameter changed from its nominal value, so as to yield a more numerically accurate simulation. If the nominal value is in the correct range, then the test simulation will show little or no change from the model run with nominal code parameters. A number of such tests are done with simple accretion flow model and in the following section we point out some of these.

4.3 Tests: A Flow Without Angular Momentum

To validate the accuracy of the hydrodynamics code, or at least to increase confidence in its results, a variety of test models were run which can be compared to analytical solutions. So, as a test case, we run a model where the injected matter has no specific angular momentum $\lambda = 0$ and follow the evolution. After long-time evolution, all of our models achieved a quasi-steady state. In this study of accretion flows without angular momentum around black holes, we used a Bondi flow to model a test case and started with the solution at the injection boundary.

4.3.1 Bondi Flow Simulation

A Bondi flow is a spherical accretion of gas attracted by a point mass of Newtonian gravity. As a test of the code, the Bondi flow was simulated. The numerical calculation for the two-dimensional flow has been carried out with $r_o = 200\, r_g$ and $N_r = N_z = 900$. Our computational box occupies one quadrant of the rz plane with $0 \leq r \leq 200$ and $0 \leq z \leq 200$. The incoming gas enters the box through the outer boundary, located at $r_o = 200$. Hence, the grid size is $0.22\, r_g$. We chose the units in such a way that the outer boundary (r_o) is chosen as unity and the matter density is normalized to become unity. We assume the black hole to be non-rotating and we use the pseudo-Newtonian potential $-\frac{1}{2(r-1)}$ (Paczyński and Wiita 1980) to calculate the flow geometry around a black hole (Here, r is in the unit of Schwarzschild radius $r_g = 2\,GM/c^2$). Velocities and angular momenta are measured in units of c, the velocity of light and $r_g c$, respectively. For the Bondi accretion flow, we have taken the outer boundary values of v_rs and as from standard Bondi flow solution in Paczyński and Wiita (1980) potential. Instead of injecting matter from the outer boundary of z coordinate, we have injected from the outer boundary of both r and z coordinates. This has been done keeping in mind that the Bondi flow is spherically symmetric. We run our time-dependent simulation up to a certain time so that the solution is steady. The simulation lasted until a steady state was reached, and the result was compared with the analytic solution. So, after reaching this time, we compare the Mach number and the radial velocity distribution at the equatorial plane ($z = 0$) of our computational box. In Figs 4.2a–b, we plotted the Mach number at radial direction for both the (a) analytical solution and the (b) numerical simulation. In Figs. 4.2c–d, the radial velocity distribution is shown for both the (c) analytical and (d) numerical cases. It is interesting that our simulation results are identical to the steady-state analytical solution. So we find that our simulation agreed well with analytical solution for Bondi flows.

We draw the velocity vectors for our simulation quadrant (first quadrant). In Fig. 4.3, velocity distributions are shown for the first quadrant. In Figs. 4.4a–b, we show the snapshots of the density and temperature (in keV) profiles obtained in a steady state purely from our hydrodynamic simulation. The density contour levels

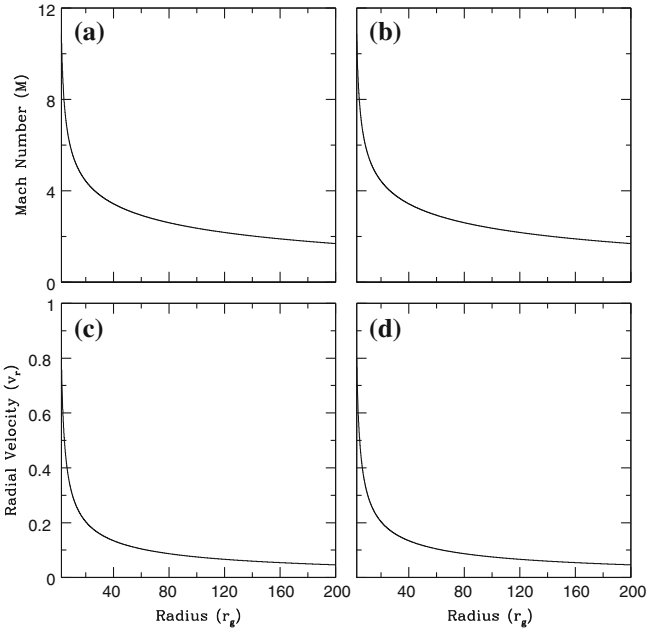

Fig. 4.2 **a**–**d** Comparison of the Mach number (**a**–**b**) and radial velocity distributions (**c**–**d**) of the analytical pseudo-Bondi solution (**a** and **c**) and the radial distribution (*at* $z = 0$) obtained from the time-dependent numerical simulations (**b** and **d**). In both the cases, the specific energy $\mathcal{E} = 0.0008$. We see that for both cases the analytical solution and time-dependent solution are identical

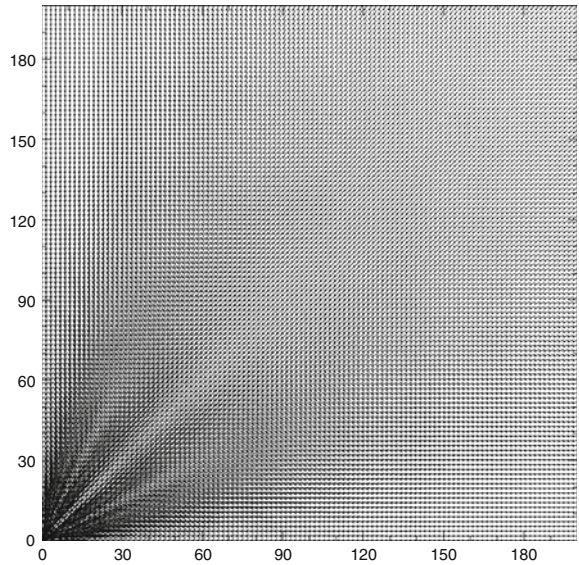

Fig. 4.3 The velocity vectors of matter obtained from the simulation for the Bondi Flow in Paczyński and Wiita (1980) potential

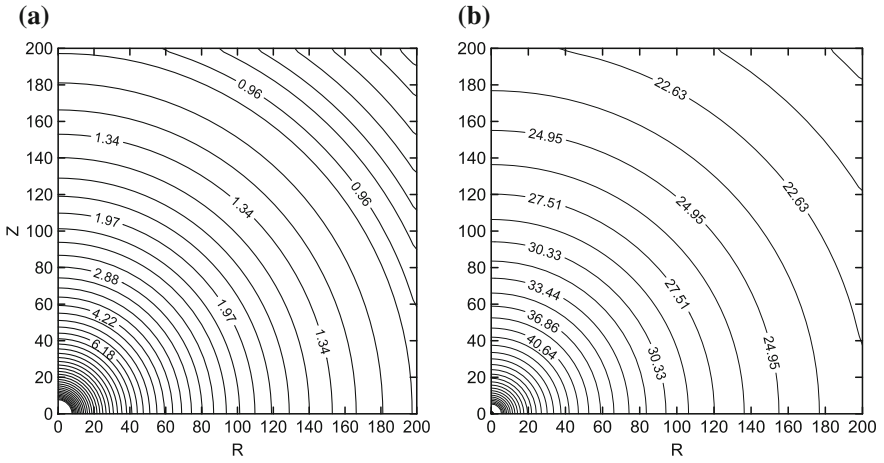

Fig. 4.4 Density (**a**) and temperature (**b**) contours inside a spherical halo. Here, the densities are in normalized units and temperatures are in keV. $\lambda = 0$ is chosen. See text for details

are drawn for $0.65 - 1.01$ (levels increasing by a factor of 1.05) and $1.01 - 66.93$ (successive level ratio is 1.1). The temperature contour levels are drawn for $16.88 - 107.8$ (successive level ratio is 1.05). Spherical symmetry of Bondi flow is clearly visible in our simulation result.

References

Molteni, D., Ryu, D., & Chakrabarti, S. K. (1996). *Astrophysical Journal, 470*, 460 (MRC96).
Ryu, D., Chakrabarti, S.K. & Molteni, D. (1997). *Astrophysics Journal, 474*, 378 (RCM97).
Paczyński, B., & Wiita, P.J. (1980). *Astrophysics and Astronomy, 88*, 23 (PW80).

Chapter 5
Simulation for Inviscid Sub-Keplerian Flows and Shocks

Abstract We scan the parameter space spanned by the specific energy and the angular momentum of the inflow and compare the time-dependent solutions with those obtained from theoretical considerations. We found several important results: (a) The time-dependent flow behaves close to a constant height model flow in the pre-shock region and a flow in vertical equilibrium in the post-shock region. (c) The infall timescale in the post-shock region is several times longer than the free-fall timescale. (b) There are two discontinuities in the flow, one being just outside of the inner sonic point. Turbulence plays a major role in determining the locations of these discontinuities. (d) The two discontinuities oscillate with two different frequencies and the post-shock flow behaves as a coupled harmonic oscillator. A Fourier analysis of the variation of the outer shock location indicates a higher power at the lower frequency and lower power at the higher frequency. The opposite is true when analysis of the inner shock is made. These behaviours will have implications in the spectral and timing properties of black hole candidates.

5.1 Introduction

In study of sub-Keplerian flows (i.e. accretion flows with angular velocity less that the Keplerian value at all radii), numerical works and analysis have been done (Chakrabarti and Molteni 1993; Molteni et al. 1994, 1996; Ryu et al. 1997). However, it is instructive to learn how the nature of the flows changes with the inflow parameters and whether the flow solution matches the analytical solution. Other unknowns include the question of stability of the flows. Pattern and stabilities of the sub-Keplerian flow with parameters space have been studied analytically (Chakrabarti 1989, 1990; Chakrabarti and Das 2001). It has been shown in Ryu et al. (1997) that if the Rankine-Hugoniot condition is not satisfied, the shock is likely to oscillate. The oscillating shocks were also observed in the presence of cooling (Chakrabarti et al. 2004) and this phenomenon is widely assumed to be the cause of quasi-periodic oscillations (QPOs) observed in radiations emitted by accretion flows around black holes. Since the generic physical processes which cause oscillations of the shocks, and therefore, the oscillations in the emitted radiation are the same in both the stellar

K. Giri, *Numerical Simulation of Viscous Shocked Accretion Flows Around Black Holes*,
Springer Theses, DOI 10.1007/978-3-319-09540-0_5

and the massive/supermassive black holes, a thorough study of the nature of shock oscillations and the dependence of the oscillation frequencies on flow parameters is essential.

Here, we present results (Giri et al. 2010) of a series of simulations in which we sample the entire region of the parameter space spanned by the specific energy and specific angular momentum (Chakrabarti 1989, 1990; Chakrabarti and Das 2001), i.e. the parameter space relevant for non-dissipative, non-magnetic and axisymmetric hydrodynamic accretion flows. We use the axisymmetric grid-based TVD code. We obtain a large number of important results. We investigate the effects of various ways of injection of gas at the outer boundary in the numerical simulations of non-viscous accretion flows. Our simulations show that an accretion shock formed and that the structure and location of the shock is dynamically unstable and oscillates for some cases. The instability could provide an explanation for quasi-periodic oscillations in the black hole candidates.

5.2 Simulation of Non-rotating Flows with Different Boundary Conditions Obtained from Standard Models

First, we run a model where the injected matter has no specific angular momentum $\lambda = 0$ and follow the evolution. Here, the specific energy is chosen to be $\mathcal{E} = 0.023$. In Fig. 5.1, we compare the numerical solution with three models which are respectively the flow with a constant height (CH), the flow with a wedge-shaped cross-section

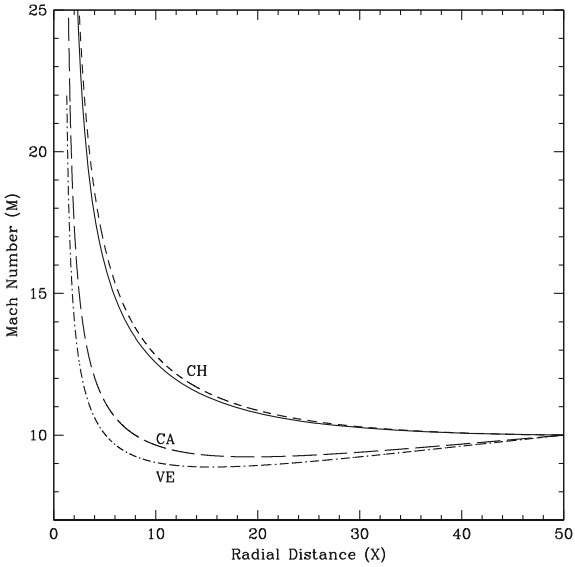

Fig. 5.1 The variation of the Mach number of a $\lambda = 0.0$, $\mathcal{E} = 0.023$ flow as a function of the radial distance from the black hole. The *solid curve* is the solution obtained from the simulation, while the other *curves* are the theoretical results for constant height (CH), constant angle (CA) and vertical equilibrium (VE) model. The time-dependent solution agrees well with that of a constant height model flow (Giri et al. 2010)

(constant angle: CA) and the flow which is in vertical equilibrium (VE). See CD01 for the definitions of these models. Here, we have taken $r_o = 50\, r_g$ and $N_r = N_z = 256$. Thus, our computational box occupies one quadrant of the $r-z$ plane with $0 \le r \le 50$ and $0 \le z \le 50$. The incoming gas enters the box through the outer boundary, located at $r_o = 50$. Hence, the grid size is $0.195\, r_g$. The flow approaches the black hole smoothly and supersonically. We find that the numerical solution on the equatorial plane agrees well with the theoretical results obtained with a constant height flow but not with the other two model solutions. As there is no angular momentum, there is no question of shock, and so naturally the time-dependent solution matches the analytical constant height model.

5.3 Simulation of Flows with Angular Momentum and Finite Inflow Thickness

In the next set of simulations, we include the angular momentum. This set of simulations has been carried out with $r_o = 50 r_g$ and $N_r = N_z = 256$. Thus, our computational box occupies one quadrant of the $r-z$ plane with $0 \le r \le 50$ and $0 \le z \le 50$. The incoming gas enters the box through the outer boundary, located at $r_o = 50$. Hence, the grid size is $0.195\, r_g$. We assume a fixed Mach number $M = v_r/a = 10$ at the outer boundary and $z_o/r_o = 0.1$, where z_o and r_o are the height and radial distance of the injected matter at the outer boundary. We also consider the incoming gas at the outer boundary which is cool and hence supersonic. We assume a fixed Mach number $M = v_r/a$ which is large ($M \gg 1$) at the outer boundary. We consider the inflow at the outer boundary which has a small thickness or a small arc angle $\theta = \arctan(h_{in}/r_b) \ll 1$. With these assumptions, we can fix three parameters, v_r, a and h, and we are effectively left with a single free parameter, the specific angular momentum λ, using which we classify the properties of accretion flows. In Fig. 5.2, we present the classification of the solutions in the parameter space spanned by the conserved energy and angular momentum (Chakrabarti 1989, 1990). In each region, the solution is qualitatively different. The classifications are made in all the three models, CH, CA and VE. For the detailed meaning of various divisions in the parameter space, see, C96. Briefly, for CH model, the curve *abc* denotes the boundary between one (saddle type, on the left of the curve) and two sonic points (one saddle type and one circle type) in the flow solution. The region *abd* contains flow parameters which produce two saddle type and one circle type sonic points, but no steady shock conditions are satisfied. The region *dae* has the same flow topologies as in *abd*, but the steady shocks can form in accretion flows. The flow with parameters from *eaf* can form steady shocks only in winds and outflows. The solution topology in the region *fag* is the same as that in *eaf*, but the steady shock condition is not satisfied. The points above *ag* has only one saddle type sonic point. The solutions from points in *bcedb* have one saddle type and one circle type sonic points, however, the solutions do not extend to infinity. Flows with parameters from other regions do

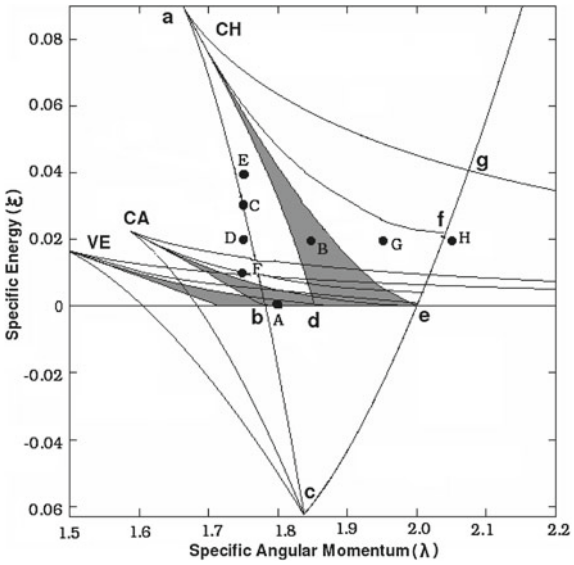

Fig. 5.2 The parameter pairs $(\mathcal{E}, \lambda)$ marked with filled circles on the classification diagram are used for numerical simulations (Cases A–H) in this chapter. See text for details

Table 5.1 Sonic points and shock locations (if any) obtained from three models for all the Model runs presented in this chapter

			Vertical equilibrium			Wedge shaped			Constant height		
Case	$\mathcal{E}$	λ	x_{in}	x_{out}	x_s	x_{in}	x_{out}	x_s	x_{in}	x_{out}	x_s
A	2.962e-04	1.80	2.321	1003.44	31.027	2.45	12.59	11.104	2.75	42.12	–
B	0.02	1.85	2.154	–	–	2.24	–	–	2.36	56.1	11.42
C	0.03	1.75	2.296	–	–	2.482	–	–	3.37	36.1	–
D	0.02	1.75	2.341	–	–	2.53	–	–	–	57.162	–
E	0.04	1.75	2.257	–	–	2.44	–	–	3.03	25.34	–
F	0.01	1.75	2.393	–	–	2.60	28.825	–	–	119.87	–
G	0.02	1.95	2.021	–	–	2.05	–	–	2.10	–	–
H	0.02	2.05	–	–	–	2.06	–	–	–	–	–

not have any kind of steady solution. Similar curves for the other two models, namely CA and VE, have similar meanings.

We have shaded one region which produces standing shocks in each model. The Cases (A–H) which were run are given in Table 5.1 where the values of the conserved energy and angular momentum $(\mathcal{E}, \lambda)$ are shown. These values are also marked inside Fig. 5.2 with filled circles to show that depending on the theoretical model, the same pair of flow parameters may or may not produce standing shocks. Our goal is to find out which model is vindicated by numerical simulation results. In Table 5.1, we also present the locations of the inner and outer sonic points, if any, and the stable shock locations, if any. The Cases (A–H) that have been run are given in Table 5.1 where the values of the conserved energy and angular momentum $(\mathcal{E}, \lambda)$ are shown. These

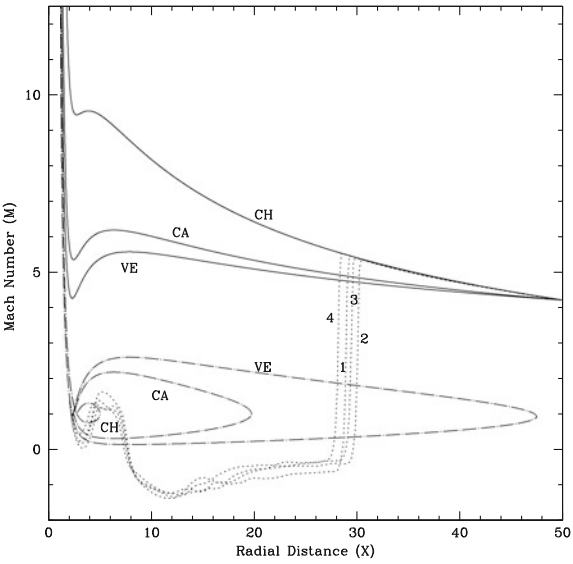

Fig. 5.3 A comparison of the theoretical results obtained from various models (*marked*) with those from numerical simulations (*dotted*) for the same outer boundary condition (Case A). *Solid curves* are for the branch passing through outer sonic point and *long-dashed curves* are for the branch passing through the inner sonic point. Mach number variation on the equatorial plane is shown. The pre-shock region matches that of a constant height flow, while the post-shock region is similar to the flow in vertical equilibrium. The presence of two shocks in the numerical solution may be noted (Giri et al. 2010)

values are also marked inside Fig. 5.2 with filled circles to show that depending on the theoretical model, the same pair of flow parameters may or may not produce standing shocks. Our goal is to find which theoretical model is vindicated by the numerical simulation results. In Table 5.1, we also present the locations of the inner and outer sonic points, if any, and the stable shock locations, if any. In Fig. 5.3, we show the results of Case A. The parameters used are $\lambda = 1.80$, $\mathcal{E} = 2.962 \times 10^{-4}$. The dotted curves give the variation of the Mach Number obtained from the numerical simulation (for the grid on the equatorial plane) at four consecutive times 1.90, 1.91, 1.92 and 1.93 s. They are marked as 1, 2, 3 and 4 respectively. Superposed on these curves are the theoretically obtained solutions for various models (marked) with the same outer boundary condition—solid curves for supersonic branch and long-dashed-dotted curves for subsonic branch. Theoretically, the steady shock is supposed to form at 31.027 in vertical equilibrium model (Table 5.1). Numerically, however, we find that the flow has formed a shock, but oscillates around a mean location. The flow Mach Number jumps and becomes subsonic at around ($x \sim 28$). However, the shock location oscillates. In some part of the post-shock region, the flow has a 'negative' Mach number. In this case, matter actually flows outward, bouncing back from the centrifugal barrier on the equatorial plane. At around ($x \sim 7$), the flow becomes supersonic and again forms a relatively weaker 'inner shock' at around ($x \sim 5$). This inner shock also oscillates. Several important facts arise out of this exercise: (a) The inject matter behaves like a flow of constant thickness in the pre-shock region, (b) the Mach number variation in the post-shock region is closer to that of the flow in vertical equilibrium. Of course, the back-flow due to the centrifugal barrier is a major factor

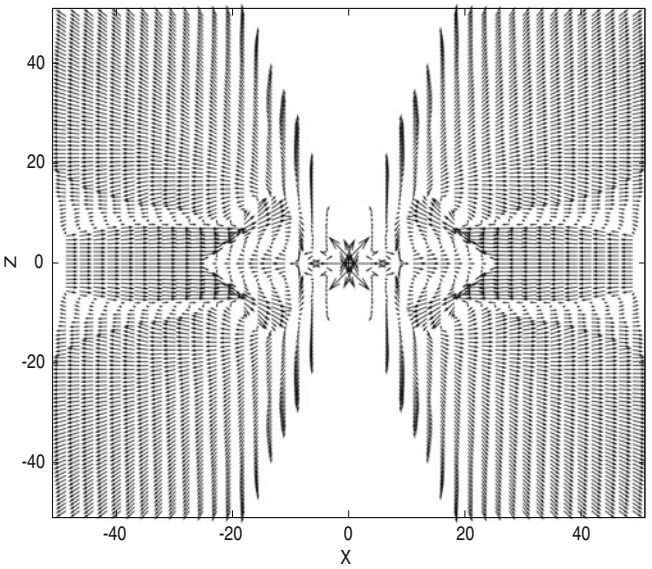

Fig. 5.4 The velocity vectors of matter obtained from the simulation for Case A. Due to centrifugal barrier, matter bounces backward and forms the shock. The injected flow in the post-shock region is deflected away from the equatorial region and enters into the black hole supersonically from higher elevation (Giri et al. 2010)

to influence the post-shock region. This is clearly seen in Fig. 5.4 where the velocity vectors are plotted. The back-flow diverts the matter from the post-shock region to regions away from the equatorial plane and produces jets and outflows. Some of this diverted matter enters into the black hole from a height and becomes supersonic at around 2.5. Though as per injection condition at the outer boundary, the pre-shock flow properties match the theoretical results of a constant height (CH) inflow, to our surprise, the post-shock flow properties match closely the theoretical results obtained assuming a hybrid-model inflow (Chakrabarti 1989). What this means is that the shock locations from simulations may be somewhat different from those of theoretical results that assume either the CH or vertical equilibrium (VE) condition on both sides of the shock. The behaviour of the time-dependent solution is evident in Fig. 5.5, where we plot the velocity vector field and the density contours at regular intervals at times t = 1.50, 2.0, 2.5 and 3.0 s. The density contours in the post-shock region resemble those of a thick accretion disc (Paczyński et al. 1980), though our results are more realistic since the radial velocity is included here. The shock clearly moves around and the outflow also shows corresponding fluctuations. The density contours are for 0.01(0.01)0.1(0.1)1(1)13, where the density inside a parenthesis gives the interval and left and right numbers are 'from' and 'to' density values. The lowest density contour is at the highest altitude. The presence of two oscillating shocks is clear from successive figures. Some matter could be seen deflected outwards as outflows. The region close to the Z-axis remains empty due to the centrifugal

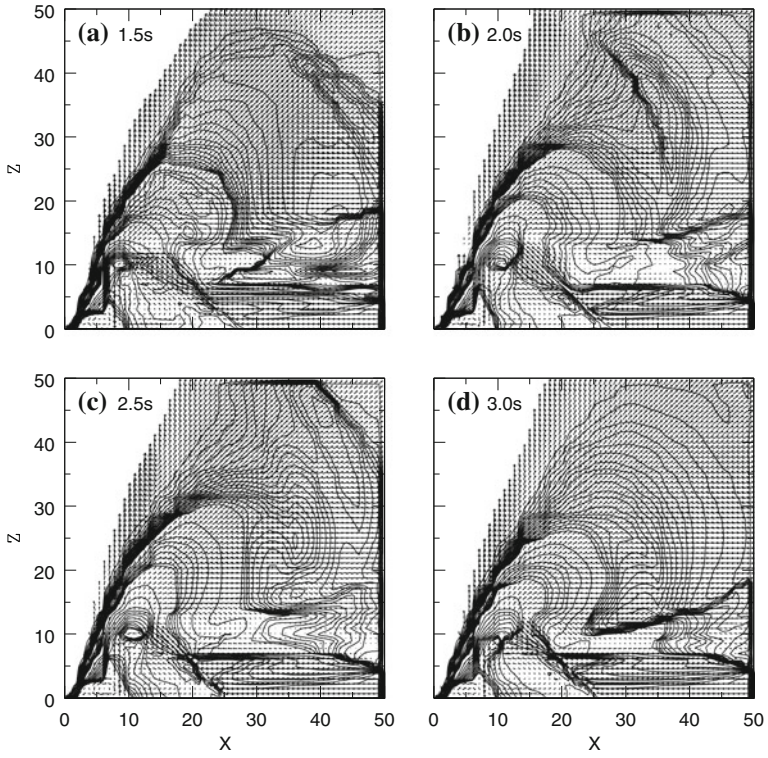

Fig. 5.5 Time-dependent behaviour is best seen in the density contours and velocity vector fields plotted at regular time intervals. Time in seconds is marked on each box. The flow is deflected at the shock and contributes to the jets and outflows. Both the shock locations can be seen (Giri et al. 2010)

barrier. Turbulence slows down the flow and consequently, the infall time $t_{inf} = \Sigma \frac{\delta r}{v_r}$, where δr is the grid size and v_r is the local radial velocity is longer than free-fall time $t_{ff} = r^{3/2}$ in the post-shock region. A detailed computation using the radial velocity averaged over 20 grids in the vertical direction and using radial coordinate from the outer shock to the event horizon shows that the ratio $R_t = t_{inf}/t_{ff}|_{post-shock} \sim 3.6$ in this case. In the pre-shock region, $R_t \sim 1$. The details related to infall and outfall timescales are discussed in a future section.

5.3.1 Time Variation of Shock Locations

We continue our detailed investigation of Case A. In Fig. 5.6, we show the variation of the outer (OS) and inner shock (IS) locations (dimensionless unit) with time (in seconds). The oscillating nature settles down after an initial transient phase of

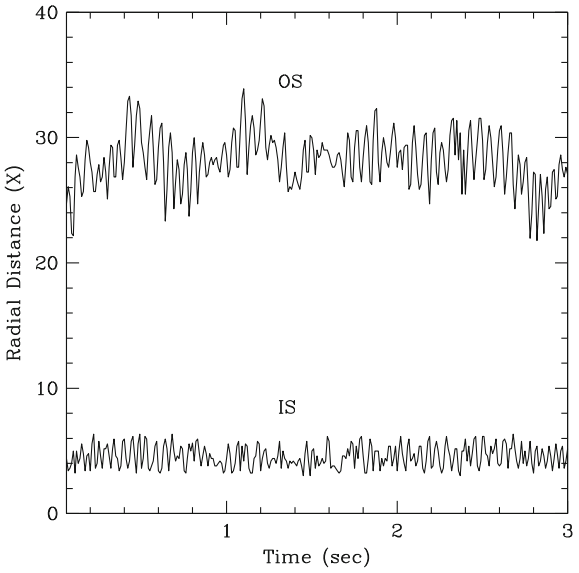

Fig. 5.6 Variation of the shock locations in dimensionless units with time (seconds). Case A parameters are chosen for simulation. A stellar mass $M = 10\,M_{\odot}$ black hole was chosen for the purpose of time computation. The time will scale with the mass of the black hole in this case since the dissipation of the flow and the radiative transfer were neglected (Giri et al. 2010)

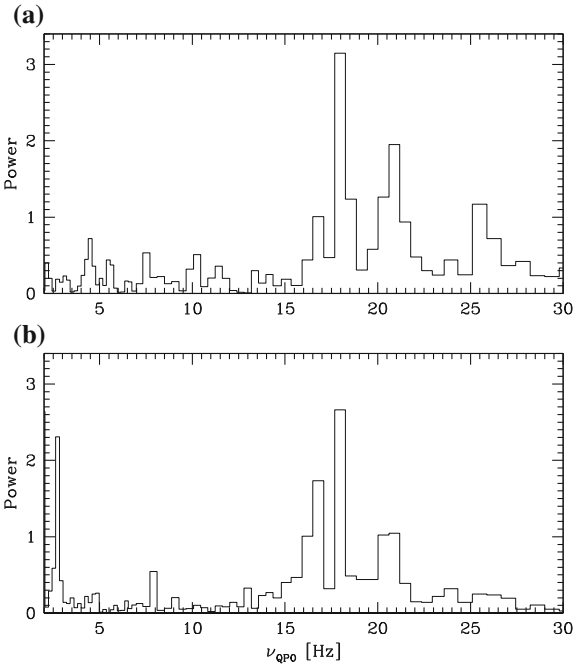

Fig. 5.7 **a**–**b** Power density spectra of the time variation of the **a** inner and the **b** outer shock locations. The frequencies are calculated assuming $M = 10\,M_{\odot}$. It will scale inversely with the mass of the black hole. The outer shock shows strong peaks at 1.56 and 17.97 Hz, while the inner shock peaks at 17.97 Hz only. Such an oscillation is thought to cause the quasi-periodic modulations in X-ray intensities from black hole candidates

$t \sim 0.06$. We clearly see the presence of oscillations in both the shocks, though the amplitudes are larger for the outer shock. The outer shock location oscillates between 26 and 32 and the inner shock oscillates between 3 and 5.

In Figs. 5.7a–b, we present the power density spectrum (PDS) of the time variation of the shock locations. In (a) and (b), the PDSs for the inner and outer shock locations are shown. The outer shock shows a peak at 1.56 Hz, but otherwise, both the PDSs show strong peaks at ∼18 Hz. In the subsonic flow of the post-shock region, the movement of inner shock also perturbs the outer shock location and thus the high frequencies are the same. Because of the strong turbulence close to a black hole which is formed due to the interaction of the incoming wave and the flow bounced back from the centrifugal barrier, a weak shock is formed closer to the black hole, though both the normal outer shock and the inner shock seem to oscillate with the same frequencies—the outer shock shows more power at lower oscillation frequency and the inner shock shows more power at higher oscillation frequencies. As will be discussed later, these oscillations can cause significant modulations in the

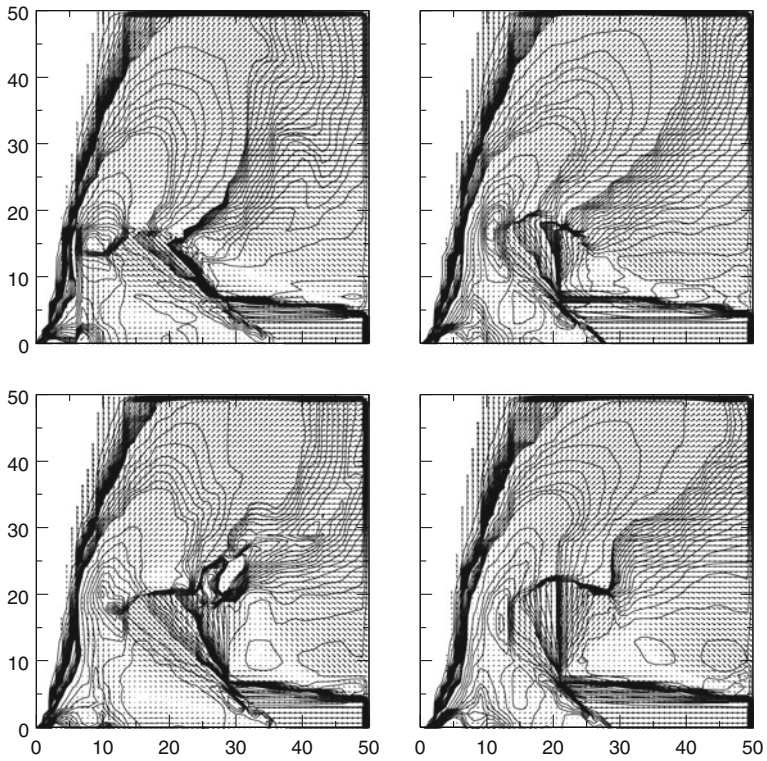

Fig. 5.8 The density contours (*solid curves*) and velocity vector fields (*arrows*) at four different λs ($\lambda_1 = 1.75$, *upper left*; $\lambda_2 = 1.85$ *lower left*; $\lambda_3 = 1.95$, *upper right*; $\lambda_4 = 2.05$, *lower right*) are shown

X-ray intensity and cause so-called QPOs in black hole candidates (Molteni et al. 1996; Chakrabarti et al. 2004). It is interesting to study how the density and velocity distributions change with the angular momentum (λ) of the flow keeping energy ($\mathcal{E}$) fixed. We again choose the flow parameters of Cases D, B, G and H (Table 5.1 and Fig. 5.2). We vary λ (1.75, 1.85, 1.95 and 2.05 respectively) while keeping the specific energy the same. In Fig. 5.8, the density contours (solid curves) and velocity vector fields (arrows) at four different λs (Case D, upper left; Case B, lower left; Case G, upper right; Case H, lower right) are shown. Density contours are drawn from the top solid lines to the bottom: 0.01, 0.02, . . ., 0.09, 0.1, 0.2, . . ., 0.9, 1, 2, 3, . . ., 12, 13 respectively.

5.4 Infall Timescales of Sub-Keplerian Flows

In this section, we wish to compare the infall timescale and free-fall timescale of matter which is accreted onto black holes. We took Case A for this experiment. In Fig. 5.9, we compared the averaged infall velocities at four different times with free-fall velocity. In the Fig. 5.9 1, 2, 3 and 4 represent infall velocities at 1.5, 2.0, 2.5 and 3.0 s respectively. Here, we have considered the infall velocity averaged over 20 grids above the equatorial plane. It is not necessary that it should be taken only for 20 grids. It could be taken for any reasonable number of grids. Comparing with the same solution at equatorial plane, we observed that in no part of the region does the average velocity become negative and this fact differs with the case of equatorial plane, where a part of the region belongs to the negative Mach number, i.e. negative velocity. We calculate the infall timescale in the following way as $\tau_{infall}=\Sigma\frac{\delta r}{v_r}$, where

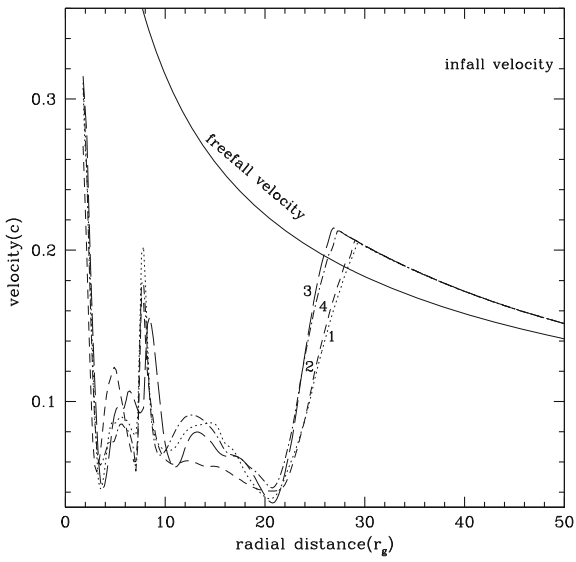

Fig. 5.9 Variation of average infall velocities at four different times with free-fall velocities. The parameters for the flow are $\mathcal{E} = 0.00029610$ and $\lambda = 1.80$. The notations 1, 2, 3 and 4 represent infall velocities at 1.5, 2.0, 2.5 and 3.0 s respectively. Here, we have considered the average infall velocity taking 20 grids above the equatorial plane

Table 5.2 Comparison of shock locations and timescales for simulation at different times (t) of the run

$\lambda = 1.80, \mathcal{E} = 0.00029610$				
Time	Shock location (r_g)	Infall time (t_i)	Free-fall time (t_f)	Ratio (t_i/t_f)
1.50	29.980469	0.0395	0.0109	3.63569
2.0	27.6367190	0.0306	0.0096	3.17509
2.50	29.7851560	0.0385	0.0107	3.61000
3.0	27.0507810	0.0317	0.0092	3.43383

δr is the grid width and v_r is the average velocity within the grid of the matter. The infall times and free-fall times and their ratios after shock for four different stages of accretion flow are given in Table 5.2. We calculate the infall time of the matter from the location of the outer shock to event horizon. We are only interested to calculate post-shock infall time and corresponding free-fall time. Here, it should be noted that this infall time which we calculate may not be equal to the actual infall time because we choose a particular number of grids for taking the average velocity. However, for sufficiently large number of grids, the result should be reasonable. Calculation of the infall timescale indicates that it is several times larger compared to the free-fall time. From the table, we see that the ratio of infall and free-fall time always changes implying that the infall time is influenced by the turbulence. This strong turbulence may be the cause of the inner shock or bump (Giri et al. 2010). A detailed computation using radial velocity, which is averaged over 20 grids in the vertical direction and using radial coordinate from the outer shock to the event horizon, shows that the ratio $R_t = t_{inf}/t_{ff}|_{post-shock} \sim 3.6$ in this case. In the pre-shock region $R_t \sim 1$.

We now focus our attention on the infall to free-fall time ratio by showing its dependence on the flow parameters.

5.4.1 *Infall Timescales for the Flows with Different Specific Angular Momenta (λ)*

We choose the flow parameters in such a way that we only vary λ (1.75, 1.85, 1.95 and 2.05 respectively) when the specific energies remain the same. We keep specific energy as $\mathcal{E} = 0.02$. In Fig. 5.10, we compare average infall velocities with respect to radial distances at a particular time for four cases. In this case, we keep energy fixed and vary the angular momenta λ_1, λ_2, λ_3 and λ_4 are 1.75, 1.85, 1.95 and 2.05 respectively. The infall and free-fall times are given in Table 5.3. We calculate the infall time of the matter from the location of the outer shock to the event horizon. We have ignored the pre-shock infall time as it nearly follows the free-fall time before shock. From the table, we see that the ratio increases when the angular momentum increases. The ratio R_t of the infall time and the free-fall time from the outer shock increases almost monotonically, which are 2.06, 3.06, 4.63 and 4.52 respectively.

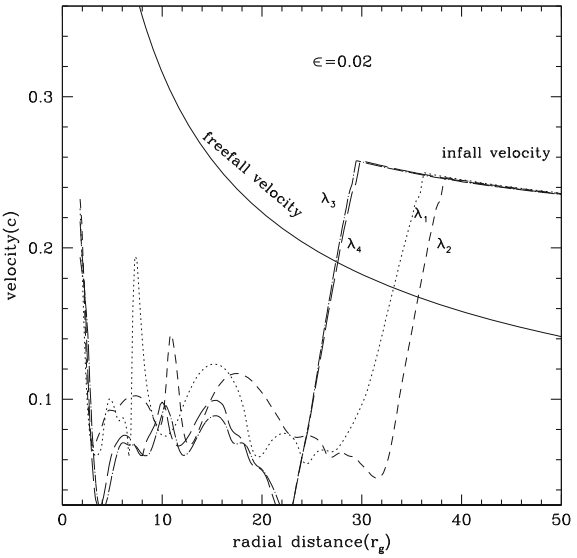

Fig. 5.10 Variation of average infall velocities with respect to radial distances at a particular time for four cases. In this case, we keep energy as fixed ($\mathcal{E} = 0.02$) and vary the angular momentum λ_1, λ_2, λ_3 and λ_4 are 1.75, 1.85, 1.95 and 2.05 respectively

Table 5.3 Comparison of shock locations and timescales for flows with different specific angular momenta (λ)

$\mathcal{E} = 0.02$				
λ	Shock location(r_g)	Infall time(t_i)	Free-fall time(t_f)	Ratio((t_i/t_f)
1.75	36.0351560	0.0293	0.0142	2.06120
1.85	38.1835900	0.0475	0.0155	3.06350
1.95	29.5898440	0.0494	0.0107	4.63119
2.05	29.1992200	0.0473	0.0105	4.52790

For all the cases, $\mathcal{E} = 0.02$

5.4.2 *Infall Timescales for the Flows with Different Specific Energies ($\mathcal{E}$)*

We turn our attention to the behaviour of the same where the specific energy of the flow is changed. The specific angular momentum is fixed. We took the angular momentum as $\lambda = 1.75$. In Fig. 5.11, we compare averaged infall velocities with respect to radial distances at a particular time for four cases. Here, we keep angular momentum as a fixed number and vary the energies, which are 0.01, 0.02, 0.03 and 0.04 respectively. The infall and free-fall times are given in Table 5.4. We calculate the infall time of the matter from the outer shock to the event horizon. We ignore the pre-shock infall time as it nearly follows the free-fall time before shock. From Table 5.4, we show no significant change in the ratios for different energies. So we can conclude that the average infall timescale from the post-shock region appears to be a few times longer than its free-fall timescale due to turbulence.

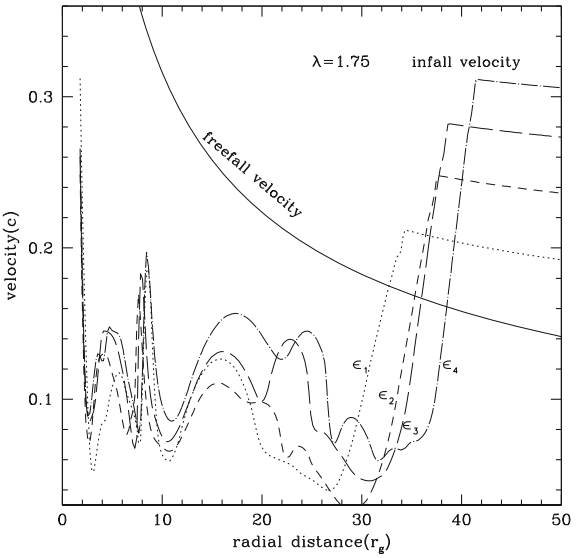

Fig. 5.11 Variation of average infall velocities with respect to radial distances at a particular time for four cases. In this case, we keep angular momentum as fixed ($\lambda = 1.75$) and vary the energies which are 0.01, 0.02, 0.03 and 0.04 respectively

Table 5.4 Comparison of shock locations and timescales for flows with different specific energies ($\mathcal{E}$)

$\lambda = 1.75$				
Energy	Shock location(r_g)	Infall time(t_i)	Free-fall time(t_f)	Ratio((t_i/t_f)
0.01	35.0585900	0.0398	0.0136	2.92000
0.02	36.0351560	0.0293	0.0142	2.06120
0.03	36.6210900	0.0305	0.0146	2.09526
0.04	37.9882800	0.0419	0.0154	2.7215

For all the cases, $\lambda = 1.75$

5.5 Ratio of the Outflowing and Incoming Matters

We now estimate the properties of outflow. Generally, all these quantities should be functions of z. Here, we consider the properties of the outflows when they are just launched or detached from the inflow. All their subsequent evolutions should be due to the outflow itself and does not affect the inflow any longer. We noted in Figs. 5.4 and 5.5 that a considerable amount of matter is ejected outwards after they are bounced from the centrifugal barrier. It would be interesting to compute the amount of matter that leaves the grid system due to outflows. In Figs. 5.12a–b, we show the ratio of the outflow rate (calculated by adding those matter leaving the grid) and inflow rate (calculated from the outer boundary condition) for these four Cases (Cases B, D, G and H) presented before. Here only λ is varied. For clarity, we present the results for $\lambda = 1.75$ and 1.85 in Fig. 5.12a and those for $\lambda = 1.95$ and 2.05 in Fig. 5.12b. We also calculate the averaged percentage of matter which

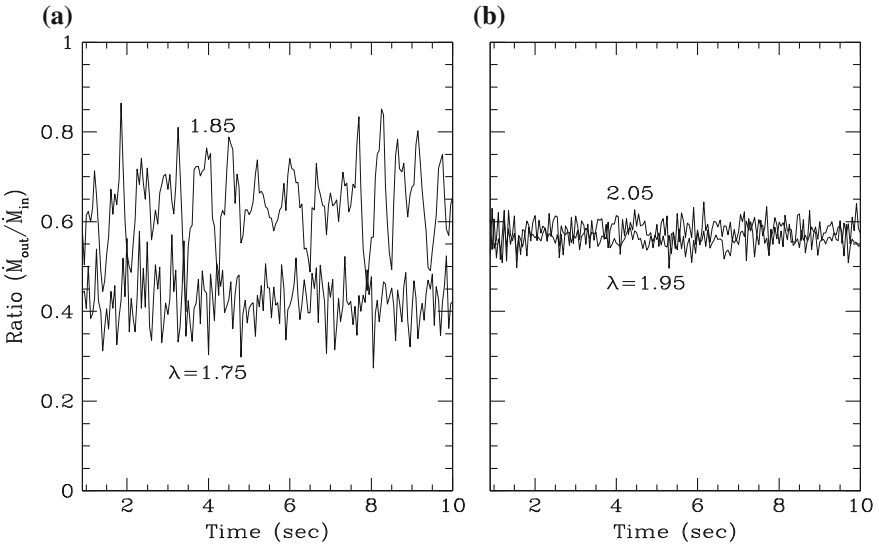

Fig. 5.12 Variation of ratio of outflowing matter to injected matter with time when the specific angular momentum is increased: **a** $\lambda = 1.75, 1.85$, **b** $\lambda = 1.95, 2.05$ (Giri et al. 2010)

is going with outflow for different angular momenta. The mean ratios for the above Cases are 0.42, 0.64, 0.56 and 0.58 respectively. From the above ratios, it is clear that the percentage of outflowing matter increases with the increase in λ from 1.75 to 1.85. In this case, we also find that the amplitude of the percentage oscillation is very high. However, in the case of high angular momentum, the amplitude of the percentage oscillation is low. So we see that for higher λ, the percentage of matter decreases. We notice that the amplitude and frequency of fluctuations in the outflow rate are mainly dictated by the fluctuations of the outer shock location, though the inner shock modulates it further.

References

Chakrabarti, S. K. (1989). *Astrophysics Journal*, *347*, 365.
Chakrabarti, S. K. (1990). *Theory of transonic astrophysical flows*. Singapore: World Scientific.
Chakrabarti, S. K., & Das, S. (2001). *MNRAS*, *327*, 808.
Chakrabarti, S. K., & Molteni, D. (1993). *Astrophysics Journal*, *417*, 671.
Chakrabarti, S. K., Acharyya, K., & Molteni, D. (2004). *Astronomy and Astrophysics*, *421*, 1.
Giri, K., Chakrabarti, S. K., Samanta, M. M., & Ryu, D. (2010). *MNRAS*, *403*, 516.
Molteni, D., Lanzafame, G., & Chakrabarti, S. K. (1994). *Astrophysics Journal*, *425*, 161.
Molteni, D., Ryu, D., & Chakrabarti, S. K. (1996). *Astrophys Journal*, *470*, 460.
Molteni, D., Sponholz, H., & Chakrabarti, S. K. (1996). *Astrophysics Journal*, *457*, 805.
Paczyński, B., & Wiita, P. J. (1980). *Astronomy and Astrophysics*, *88*, 23.
Ryu, D., Chakrabarti, S. K., & Molteni, D. (1997). *Astrophysics Journal*, *474*, 378.

Chapter 6
Simulation of Viscous Accretion Flows

Abstract We study the time evolution of a rotating, axisymmetric, viscous accretion flow around black holes using a grid-based finite difference method. We use the Shakura–Sunyaev viscosity prescription. However, we compare with the results obtained when all the three independent components of the viscous stress are kept. We show that the centrifugal pressure supported shocks become weaker with the inclusion of viscosity. The shock is formed farther out when the viscosity is increased. When the viscosity is above a critical value, the shock disappears altogether and the flow becomes subsonic and Keplerian everywhere except in a region close to the horizon, where it remains supersonic. We also find that as the viscosity is increased, the amount of outflowing matter in the wind is decreased to less than a percentage of the inflow matter. Since the post-shock region could act as a reservoir of hot electrons or the so-called Compton cloud, the size of which changes with viscosity, the spectral properties are expected to depend on viscosity strongly: the harder states are dominated by low angular momentum and the low-viscosity flow with significant outflows while the softer states are dominated by the high-viscosity Keplerian flow having very little outflows.

6.1 Introduction

In the previous chapter, the results of standing and oscillating shock formations in inviscid flows were presented. We now extend this study by adding viscosity. While the matter in accretion discs moves in nearly circular orbits, there is also a slow drift of material inward. For this to occur, gas must lose angular momentum if it is larger than the marginally stable value to begin with. This angular momentum can be exchanged with other gases, or can be lost through torques acting on the disc. Therefore, angular momentum transport occurs. It is this outward transport of angular momentum that allows matter to drift inward, and this transfer of material constitutes the accretion process. Without angular momentum transport, there would be no transfer of matter inward and therefore no accretion: the gas would remain in stable circular orbits. Of course, as shown by Chakrabarti (1989, 1990a), when matter starts with low angular momentum, there is no need to have viscosity for

K. Giri, *Numerical Simulation of Viscous Shocked Accretion Flows Around Black Holes*,
Springer Theses, DOI 10.1007/978-3-319-09540-0_6

the matter to accrete. In this case, the radiation emitted is also very low so that the energy remains constant throughout. In this chapter, we include the viscous effects responsible for angular momentum transfer in discs.

In the previous chapter, the oscillation phenomena in accretion flows around black holes related to the QPO were reported. The study of an inviscid accretion flow around black hole showed that the shock location changes with the change in specific angular momentum (λ) and specific energy ($\mathcal{E}$), both of which were constant. In the present situation of a viscous flow, none of these is constant. Recently, one-dimensional solution for quasi-spherical viscous flow was investigated by Lee et al. (2011) who found that there are oscillatory propagating shocks moving outward when the viscosity is large enough.

The theoretical work discussed in Chakrabarti (1989, 1996) were carried out for a one-dimensional flow since otherwise the sonic point analysis would be difficult. For a two-dimensional flow, a completely self-consistent theoretical solution is not possible. This is why a numerical simulation of viscous accretion flows is necessary to answer the following questions: (a) Do the conclusions based on theoretical considerations continue to remain valid for a two-dimensional flow? (b) Do the shocks survive for higher viscosity? (c) How does the outflow rate depend on viscosity? (d) Are all the components of the viscous stress important in a thick accretion flow? (e) Under what condition does the Keplerian flow form? In the previous chapter, the oscillation phenomena in accretion flows around black holes related to the QPO were reported. The study of an inviscid accretion flow around the black hole showed that the shock location changes with the change in specific angular momentum (λ) and specific energy ($\mathcal{E}$), both of which are constant. In the present situation of viscous flow, none of these is constant.

6.2 Computational Procedure

The set-up of our simulation is the same as that presented in the previous chapter. Instead of an inviscid flow, we consider a viscous, axisymmetric flow in the pseudo-Newtonian gravitational field of a point mass M_{bh} located at the centre in cylindrical coordinates $[x, \theta, z]$. All the governing equations for viscous accretion flow are given in detail in Chap. 2 and also in Giri and Chakrabarti (2012). We will not repeat them here. The numerical calculation for two-dimensional flow was carried out with $r_o = 50r_g$ and $N_r = N_z = 512$. The calculations were performed with 512×512 cells, so each grid has a size of 0.097 in units of the Schwarzschild radius. The timescale of matter from the outer boundary is about 0.07s as computed from the sum of $dr/ < v_r >$ over the entire radial grid, $< v_r >$ being averaged over 20 vertical grids. In order to mimic the horizon of the black hole at one Schwarzschild radius, we placed an absorbing inner boundary at $R = 1.1r_g$, inside which all materials are completely absorbed into the black hole. All the simulations were carried out assuming a stellar mass black hole ($M = 10M_{\odot}$). We carry out the simulations for several hundreds of dynamical timescales. In reality, our simulation time corresponds

to a few seconds in physical units. Now, we present the results for different cases and for different sets of parameters.

6.3 Results and Discussions

As mentioned earlier, we chose the outer boundary of the simulation grid at $r = 50$. We have run several simulations with different types of injection at the outer boundary. For each case, we got many significant results. In the next section, we discuss these results.

6.3.1 Isothermal Injection at the Outer Boundary

The specific angular momentum (λ) of the flow is chosen to be 1.66 (For comparison, we note that the marginally stable angular momentum is 1.83 in this unit.) and the specific energy ($\mathcal{E}$) of the flow at the equatorial plane ($z = 0$) is chosen to be 0.0035. The radial velocity pointing to the origin is chosen to be constant in all heights $v = ({v_r}^2 + {v_z}^2)^{\frac{1}{2}} = 0.072$. These injection parameters correspond to those of low angular momentum transonic flow solutions and are qualitatively different from those of earlier workers such as Igumenshchev et al. (1997, 2000) since they mainly inject near Keplerian flow with no radial velocity. From the energy of the flow, we obtain the sound speed at the equatorial plane to be 0.059. We employ an isothermal outer boundary condition (Molteni et al. 1996). In other words, we take the same sound speed at all heights at the outer boundary. We add the $SS\alpha$ viscous term in the non-viscous system as discussed earlier. We stop the simulation at $t = 24.75$ s. This is more than 300 times the dynamical time. Thus, the solution has most certainly come out of the transient regime and started exhibiting solutions characteristics of its flow parameters. The simulation results will be discussed now.

In Fig. 6.1a–b, we compare the Mach number and the density variations in the equatorial plane of flow for various α. To make the comparison meaningful, all the runs were carried out up to $t = 24.75$s. Each result is obtained starting with an inviscid flow $\alpha = 0$ (marked) and then gradually increasing α till the shock goes out of the grid and eventually disappears. The values of α for which the curves are drawn are (left to right in Fig. 6.1a and bottom to top in Fig. 6.1b): 0.0, 0.0175, 0.035, 0.0525, 0.06125, 0.07 and 0.0735 respectively. The shock location shifts outward with viscosity exactly as predicted in Chakrabarti (1990a, b, 1996). For inviscid flow ($\alpha = 0$), the matter bounces back from the centrifugal barrier and flows outward near the equatorial plane. As viscosity is enhanced, the angular momentum is transported outward and hence specific angular goes up. The velocity goes down and density goes up. This can be seen in Fig. 6.1b in the $3 - 30\ r_g$ region. In this particular example, the shock disappears above $\sim \alpha = 0.074$, which is the critical value

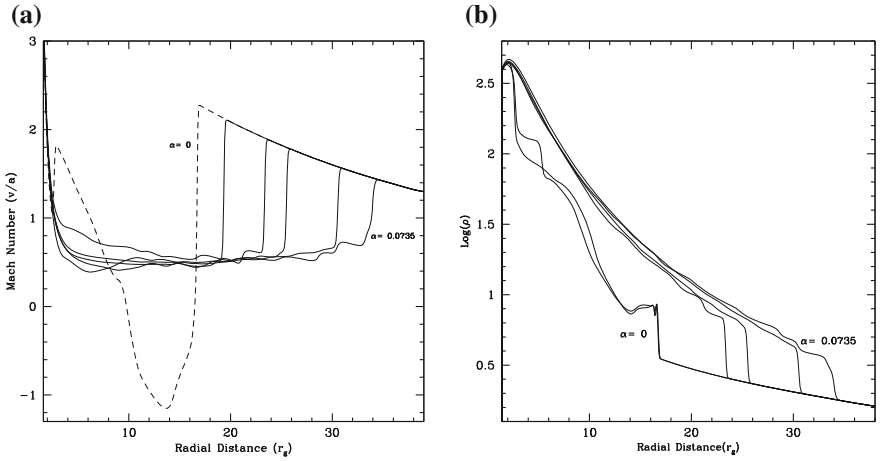

Fig. 6.1 Variation of **a** Mach number and **b** density with radial distance in a viscous transonic flow on the equatorial plane. As the viscosity parameter increases, the angular momentum is transported outward shifting along with it the centrifugal pressure supported shock wave. The α parameters are [*left* to *right* in **a** and *bottom* to *top* in **b**]: 0.0, 0.0175, 0.035, 0.0525, 0.06125, 0.07, 0.0735 respectively (Giri and Chakrabarti 2012)

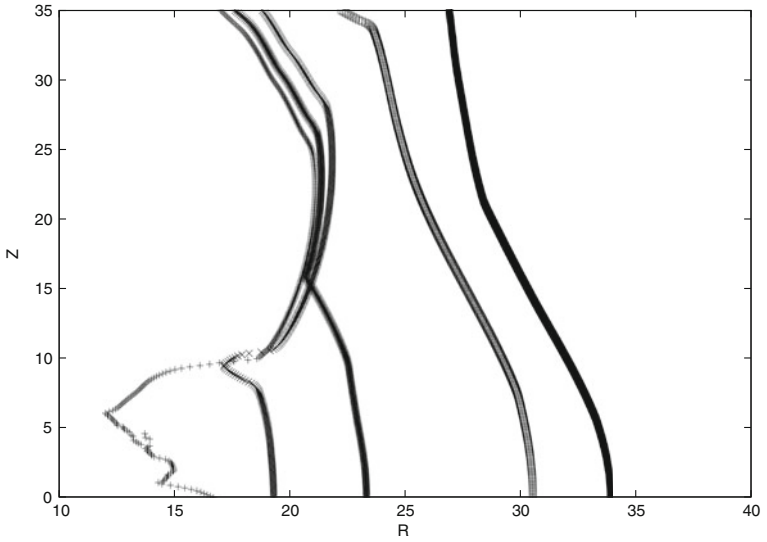

Fig. 6.2 Variation of shock locations through $r - z$ plane for different αs. See text for details

of α here. Since the grid boundary is at a finite distance in a numerical grid, it is difficult to show the disappearance of the shock since that would require changing the boundary condition dynamically to let the shock through when it reached the boundary. The results are indeed similar to the results of Chakrabarti and Molteni

(1995) where one-dimensional viscous isothermal flow was treated using smoothed particle hydrodynamics (SPH) code. As described in Chakrabarti (1990b), the critical α (α_c) is defined by that specific α for which the subsonic branch of the transonic flow solution passes through both the inner and outer sonic points. Thus, α_c clearly depends on the injected flow parameters. Hence, for a different choice of injected parameters, the critical value of α will be different. In Fig. 6.1a, we compared the shock locations in equatorial plane ($z = 0$) for different α. Now, we show how the nature of shock front changes in the entire $r - z$ plane. In Fig. 6.2, we have shown the shock locations through $r - z$ plane for different α. The results shown is at the

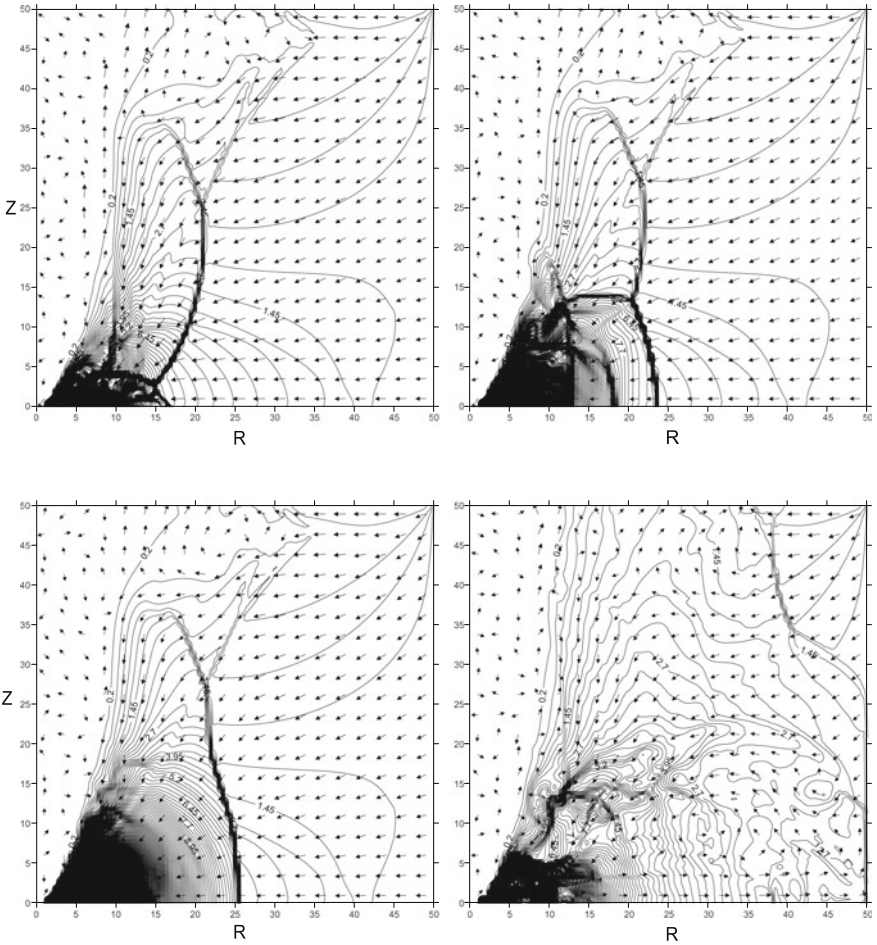

Fig. 6.3 Changes in the density and velocity distribution with the change in viscous parameter α at $t = 24.75$s. Here, densities are in normalised units, radius and velocity are in Schwarzschild units. Here, $\alpha = 0.0$ (*top left*), 0.0525 (*top right*), 0.0735 (*bottom left*), 0.074 (*bottom right*) respectively. For details see the text (Giri and Chakrabarti 2012)

time $T = 24.75$ s when the flow has achieved a steady state. Values of α for which the shock locations are shown (from left to right): 0.0, 0.035, 0.0525, 0.06125, 0.0735 respectively. Here it is noted that with the increment of α not only the shock location in equatorial plane but also the shock location along $r-z$ plane shifting outwards, i.e. both the one- and two-dimensional flows behave alike with the inclusion of viscosity. In Fig. 6.3, we show how the density of matter and the velocities vary with viscosity. We superpose contours of constant density and velocity. The length of the arrows are proportional to velocity, the longest being that of $v = 0.6$. The results are for $t = 24.75$s. $\alpha = 0.0$ (a: top left), 0.0525 (b: top right), 0.0735 (c: bottom left), 0.074 (d: bottom right) respectively. The contour having minimum density has $\rho_{\min} = 0.2$. The maximum density is (a) $\rho_{\max} = 450$, (b) $\rho_{\max} = 395$, (c) $\rho_{\max} = 354$ and (d) $\rho_{\max} = 286$. The contour interval is $\delta\rho = 0.25$. We observe that the standing shock is truly two-dimensional and oblique (Chakrabarti 1996). Here three shocks meet at a point. It is a good example of a prominent triple-shock which forms away from the equatorial plane. However, it is not a pure triple-shock, since the matter flows from right to the left for both the shocks facing the upstream. As the matter flows in from the right-hand side and passes through the shock, it becomes hot and puffs up as a thick accretion disc (see also, Molteni et al. 1994). The standing shock moves outwards as the viscosity parameter is increased. For $\alpha = 0.074$ which is larger than the critical α for this case and the shock disappears. In a numerical simulation with a finite injection radius, the shock, albeit very weak, stays very close to the outer boundary. The piled up angular momentum in the post-shock flow clearly drives the shock outwards. In Fig. 6.4, we plot the time variation of the shock location at the equatorial plane for various viscous parameter α. The values of α are (from bottom

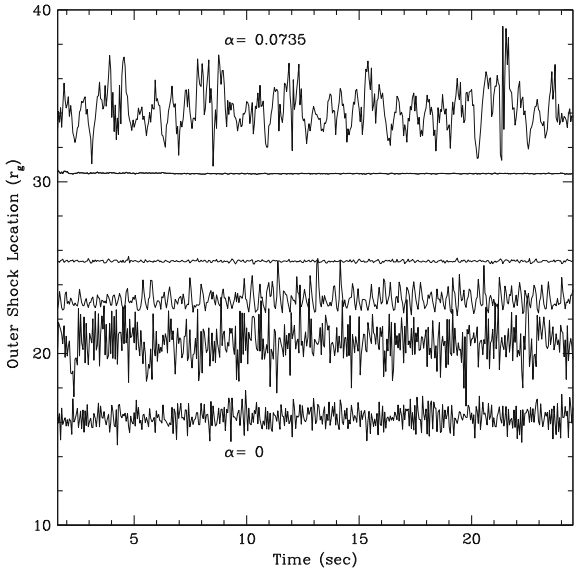

Fig. 6.4 Variation of the shock location at the equatorial plane with time for various viscous parameter α (from *bottom* to *top*: 0.0, 0.0175, 0.035, 0.0525, 0.06125, 0.0735 respectively)

to top): 0.0, 0.0175, 0.035, 0.0525, 0.06125, 0.0735 respectively. It is clear that the average shock locations shift outwards when the value of α increases. Shocks close to the black hole exhibit lower amplitude and higher frequency oscillations, while those farther out show opposite effects. This is mainly because the frequency is decided by the inverse of the infall time in the post-shock region. The compression wave in the post-shock region bounces back from the centrifugal barrier and pushes the shock outward. At some point the outward journey is stopped when post-shock pressure drops and the shock turns back. Most interestingly, for $\alpha = 0.0525$ and $\alpha = 0.06125$, the oscillation of the shock disappears and the standing shocks are formed, while for other αs there are oscillations. This is not surprising, since, as was shown for the inviscid flow (Chakrabarti 1990b) as well as the viscous flow (Chakrabarti and Das 2004), the Rankine-Hugoniot relations are satisfied only in a limited region of the parameter space, and beyond the critical viscosity the relation not satisfied at all. In this case, the flow has two sonic points and the high entropy solution must pass through the inner sonic point (Chakrabarti 1989). Hence, the flow generates entropy through a shock jump, but the location itself cannot be fixed because the Rankine-Hugoniot condition is not satisfied. This creates an unstable situation and

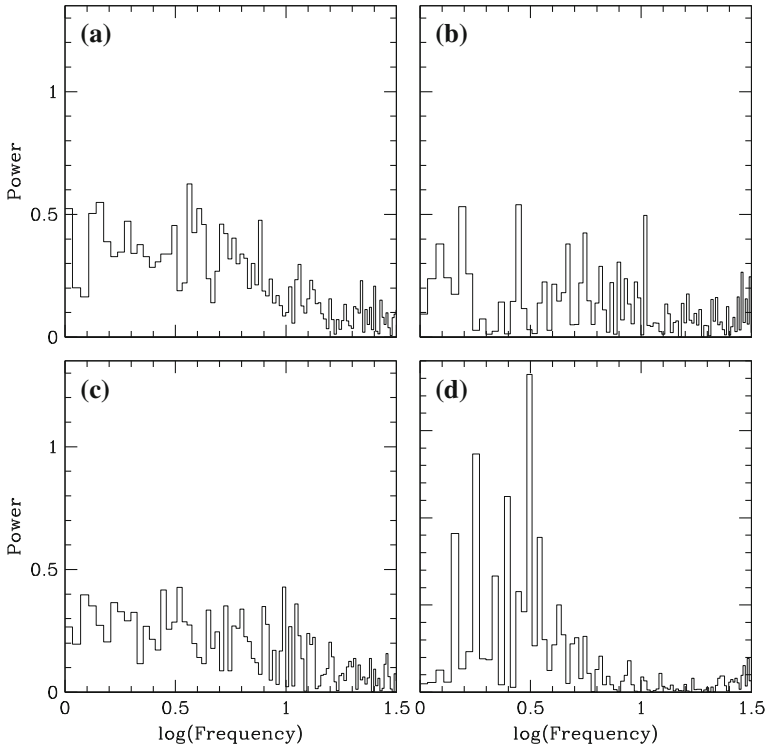

Fig. 6.5 Power density spectra of the time variation of the shock locations. The α parameters chosen for Figures a, b, c and d are 0.0, 0.0175, 0.035 and 0.0735 respectively

consequently, the shocks can oscillate (as shown in Chap. 5). It is easy to study the nature of the oscillation of the shock location when viscosity is increased. So, to fulfil our interest, we take the power density spectra of the same for four different αs. In Fig. 6.5a–d, we present the power density spectrum (PDS) of the time variation of shock locations. The α parameters chosen for Fig. 6.5a–d are 0.0, 0.0175, 0.035 and 0.0735 respectively. For $\alpha = 0.0735$, the oscillation is prominent with a certain frequency, while for the other cases no prominent oscillations are seen.

6.3.2 *Viscous Effects on Outflows*

Molteni et al. (1994) demonstrated that a large percentage of matter can leave the disc as an outflow. Thus, it is important to investigate their influence on the dynamics of inflow. It is interesting to study the effects of viscosity on the outflow rate since Molteni et al. (1994) performed the simulation for inviscid discs. We observed earlier that with viscosity, the shock recedes and becomes weaker. In Chakrabarti (1999), it was suggested that the ratio $R_{\dot{m}}$ of the outflow to the inflow rate would be guided by the compression ratio at the shock. In Fig. 6.6, we plot the time variation of the ratio of the outflow to inflow rate as the viscosity is enhanced. The values are the same as in Fig. 6.4 (from the top curve to the bottom curve). We clearly notice that although the ratios exhibit short timescale fluctuations, the average values decrease as viscosity is enhanced. This could have been guessed also from Figs. 6.3a–d, where

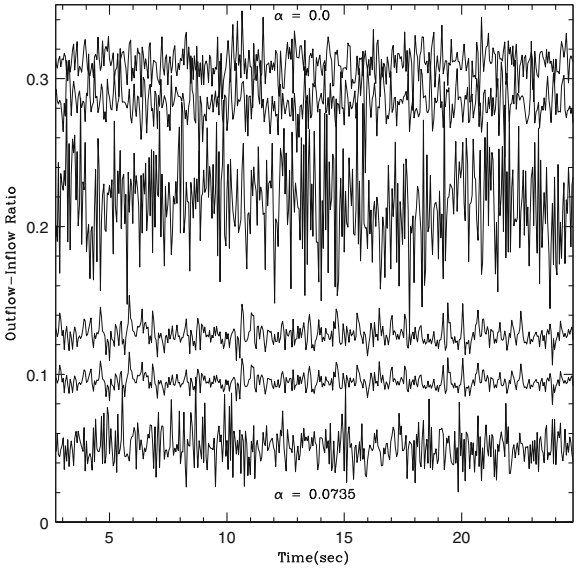

Fig. 6.6 Time variation of the ratio of the outflow to inflow rates as viscosity parameter is enhanced. Though there are short timescale fluctuations, the average values decrease as viscosity is increased showing a direct relation of the outflow rate with the strength of the shock. The viscosities are the same as in Fig. 6.4 (from the *top curve* to the *bottom curve*) (Giri and Chakrabarti 2012)

the lengths of the outgoing arrows in Fig. 6.3a–b are reduced in number and size in Fig. 6.3c–d. The longest arrow corresponds to $v \sim 0.6$.

6.3.3 Viscous Flow with a Constant Height Injection in Radial Direction

For the sake of comparison with the results of inviscid flows presented in Chap. 4, we simulate the case where the injection is purely in the $-X$ direction. The injected flow at the outer boundary has the same sound speed (temperature) as obtained from the theoretical 'constant height' model. The specific energy and specific angular momentum are $E = 0.003$ and $\lambda = 1.76$ respectively. The simulation was carried out up to $t = 7.63$s, or about 100 dynamical time (computed as a sum of $dr/ < v_r >$ over the whole radial grid, $< v_r >$ being averaged over 20 vertical grids). Figure 6.7 shows the distribution of Mach number along the equatorial plane for $\alpha = 0.0$ (dashed), 0.02 (solid), 0.035 (long dashed), 0.07 (dash-dotted) and 0.09 (log dash-dotted)

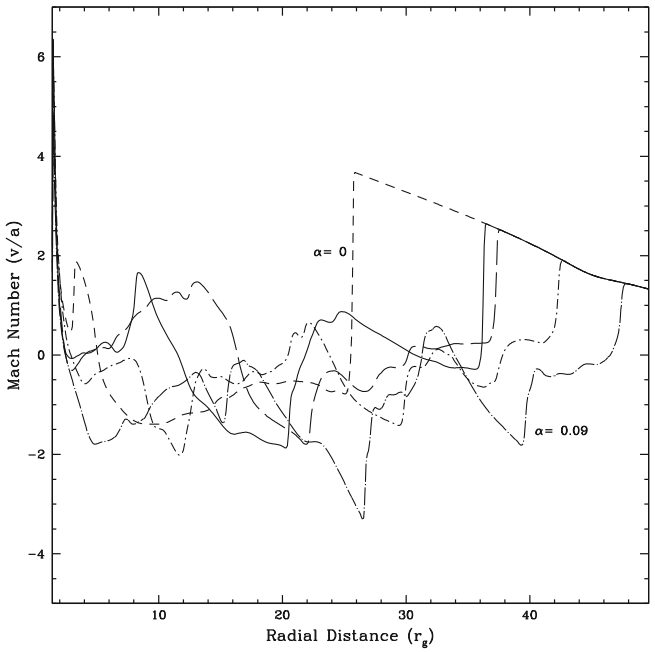

Fig. 6.7 Radial distribution of the Mach number on the equatorial plane for a flow with a constant height injection in the radial direction at the outer boundary. The viscosity parameters are: $\alpha = 0.0$ (*dashed*), 0.02 (*solid*), 0.035 (*long dashed*), 0.07 (*dash-dotted*) and 0.09 (*log dash-dotted*). The inner shock disappears at about $\alpha \sim 0.05$ and the outer shock disappears at $\alpha \sim 0.1$ (Giri and Chakrabarti 2012)

respectively. As in Chap. 3 for inviscid flow, we see the formation of a strong (outer) shock at ~ 25 and a weak (inner) shock at ~ 3 when the flow is inviscid. For $\alpha = 0.02$ and 0.035, both the shocks still form, albeit being farther out and weaker. For higher viscosity, the inner shock completely disappears. The outer shock disappears at even higher viscosity. This shows that the critical viscosity for the inner shock is much lower than that for the outer shock. Since theoretically only the outer shock was predicted, this is therefore a totally new result and could not have been anticipated without numerical simulations.

In Fig. 6.8, we show the density and velocity distributions for $\alpha = 0$ (top left) and 0.02 (top right) respectively at the end of the simulation. We zoom the inner region

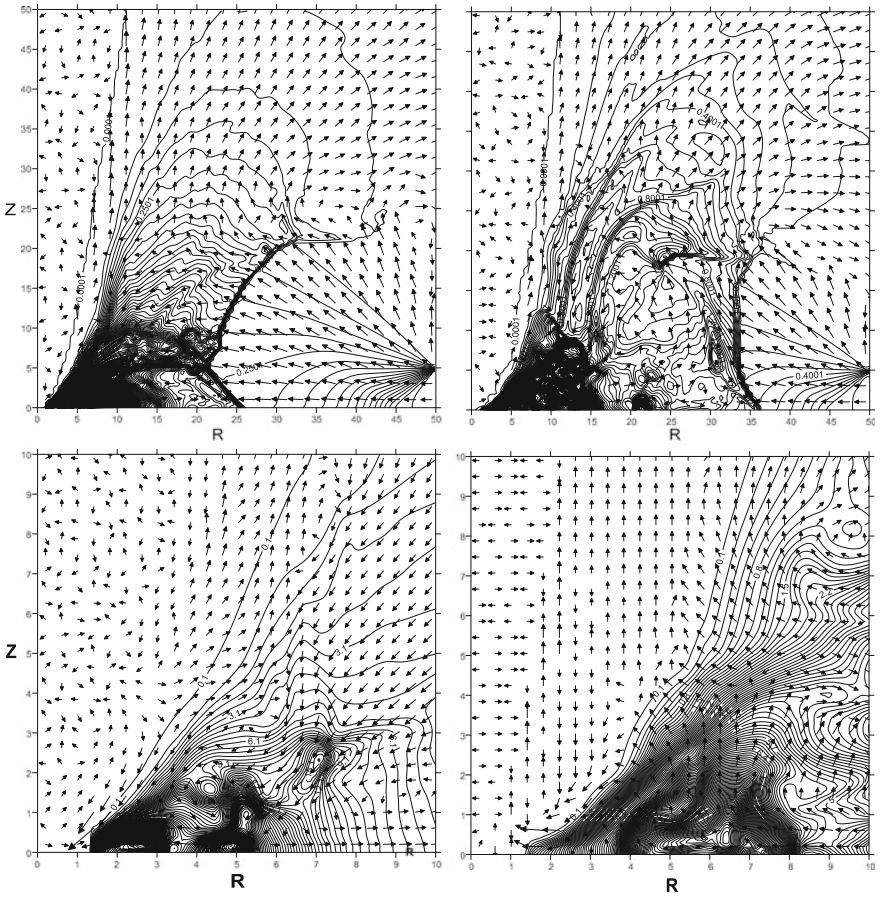

Fig. 6.8 The density and velocity distributions for $\alpha = 0$ (*top left*) and 0.02 (*top right*) respectively at the end of the simulation where the flow was injected with a constant height. We zoom the inner region to show the shifting of the inner shock from ~ 3 (*bottom left*) to ~ 8 (*bottom right*) when viscosity is increased (Giri and Chakrabarti 2012)

to show how the inner shock has shifted from ~ 3 (bottom left) to ~ 8 (bottom right) as viscosity is increased.

6.3.4 Vertical Equilibrium at the Outer Boundary

We now use a different model for injection in order to impress that the basic results remain the same even when we assume the flow to be in vertical equilibrium (Chakrabarti 1989) at the outer boundary. We inject through 50 grids out of 512 grids, i.e. the height of the disc at the injection is nearly 5 Schwarzschild radii. In this case, the injection rate of the momentum density is kept uniform throughout the injected height at the outer edge. The specific angular momentum (λ) and the specific energy ($\mathcal{E}$) at the outer boundary is chosen to be the same as in the isothermal injection case. Here too we stop the simulation at $t = 24.75$ s. The results of the simulation are discussed now. In Fig. 6.9a–b, we show the distribution of Mach number on the equatorial plane and that *averaged* over 15 grids from the equatorial plane when α is 0.0, 0.018, 0.0225, 0.0315, 0.05 and 0.09 respectively (from the leftmost curve to the rightmost curve). As the α parameter is increased, the flow behaviour changes dramatically. As in the previous case, the shock rapidly propagates outward due to the faster transport of angular momentum in the post-shock flow compared to the pre-shock flow. However, since in the vertical equilibrium model, the ram pressure of the injected flow is less, the turbulence and the back flow on the equatorial plane remains important even for high α. Figure 6.10a–d show the distribution of specific

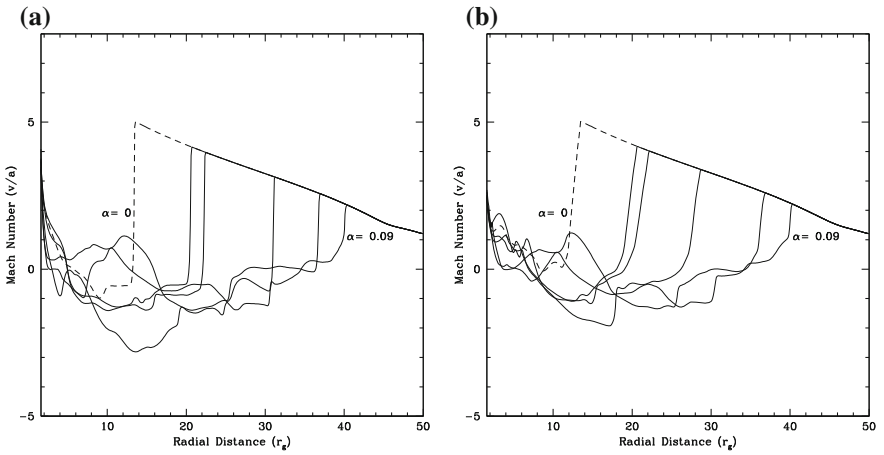

Fig. 6.9 Variation of the **a** Mach number on the equatorial plane and **b** the Mach number averaged over 15 vertical grids as a function of the radial distance on the equatorial plane as the α is increased from 0 (*leftmost curve*) to 0.09 (*rightmost curve*). See the text for details (Giri and Chakrabarti 2012)

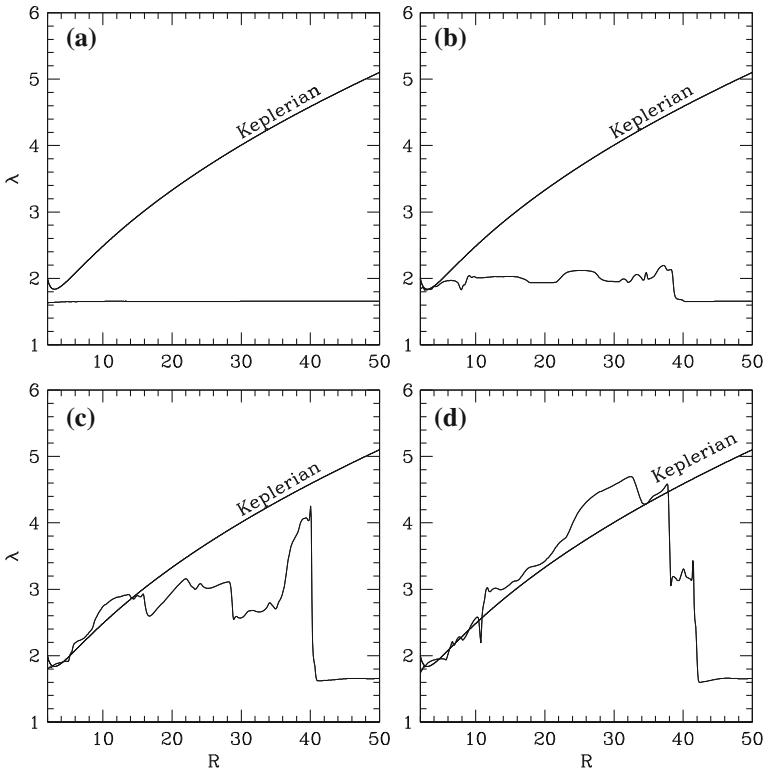

Fig. 6.10 Comparison of the specific angular momentum distributions (*thin curves*) at equatorial plane ($z = 0$) of an accretion flow as viscosity parameter α is varied. $\alpha =$ **a** 0.0, **b** 0.01, **c** 0.05 and **d** 0.09. For all the cases, the result is compared with the Keplerian angular momentum distribution (*thick curves*)

angular momentum at equatorial plane ($z = 0$) and Fig. 6.11a–d show the distribution of average specific angular momentum of the flow (density weighted average over 15 vertical grids from the equatorial plane) at the end of our simulation for different values of α (thin solid curve). For comparison, we plot the specific angular momentum distributions of a Keplerian orbit (thick upper curve). In Fig. 6.11a–d, We also plot a 'Keplerian' distribution (thick lower curve) at a height of 200 grids (~ 20 Schwarzschild radii) and compare the 15 vertical grid average angular momentum distribution that is obtained from the simulation at that height (dashed curve). The latter 'Keplerian' distribution was obtained by equating the horizontal component of the gravitational force at that height with the centrifugal force. All results are shown at $t = 24.75$s. The α parameters chosen for Fig. 6.10a,b,c and d (also for 6.11a,b,c and d) are 0.0, 0.01, 0.05, and 0.09 respectively. We note that as the viscosity is increased, the distribution in the post-shock region gradually becomes closer to the Keplerian distribution, although below $r = 3$, the distribution is always highly

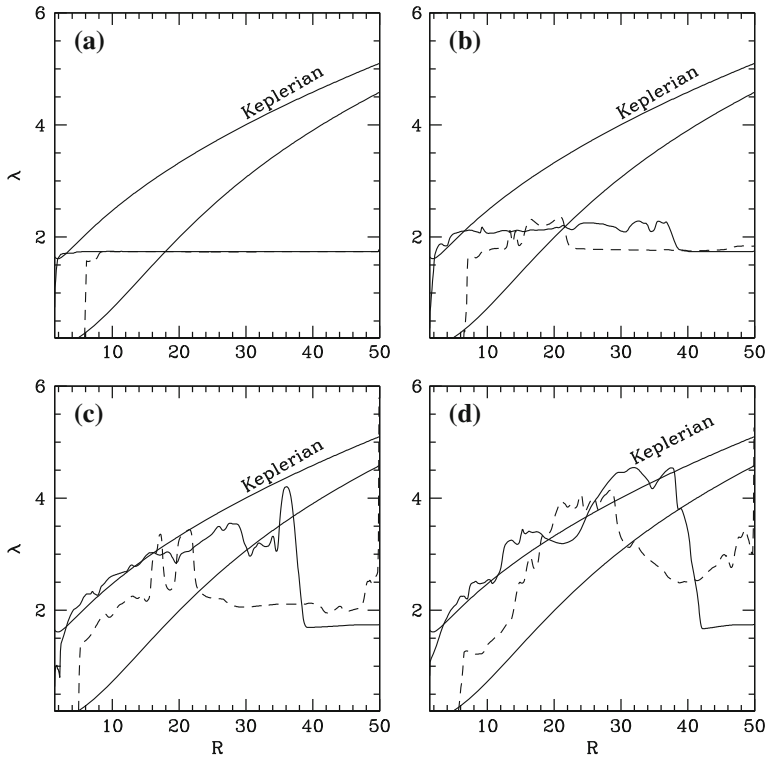

Fig. 6.11 Comparison of the specific angular momentum distributions (*thin curves*) of an accretion flow as viscosity parameter α is varied. $\alpha =$ **a** 0.0, **b** 0.01, **c** 0.05 and **d** 0.09. For all the cases, the result is compared with the Keplerian angular momentum distribution (*thick curves*) (from Giri and Chakrabarti 2012)

sub-Keplerian. At the shock, the distribution shows a jump. This is because for a given α, the transport rates in the pre- and post-shock flows are different, being very high in the post-shock region due to higher pressure. For high enough viscosity, when the shock reaches infinity (large distance), the angular momentum distribution becomes that of a Keplerian flow, which is what is expected. This is thus one scenario by which a Keplerian disc may form in a highly viscous flow. In Fig. 6.12a–b, (a) the time variation of shock locations at equatorial plane and (b) the average specific angular momentum of the system is plotted as a function of simulation time. For both the cases, the viscous effect ($\alpha = 0.05$) is compared with inviscid ($\alpha = 0$) flow. The average specific angular momentum ($\bar{\lambda}$) is obtained as

$$\bar{\lambda} = \frac{\int \lambda \rho \mathrm{d}r}{\int \rho \mathrm{d}r}$$

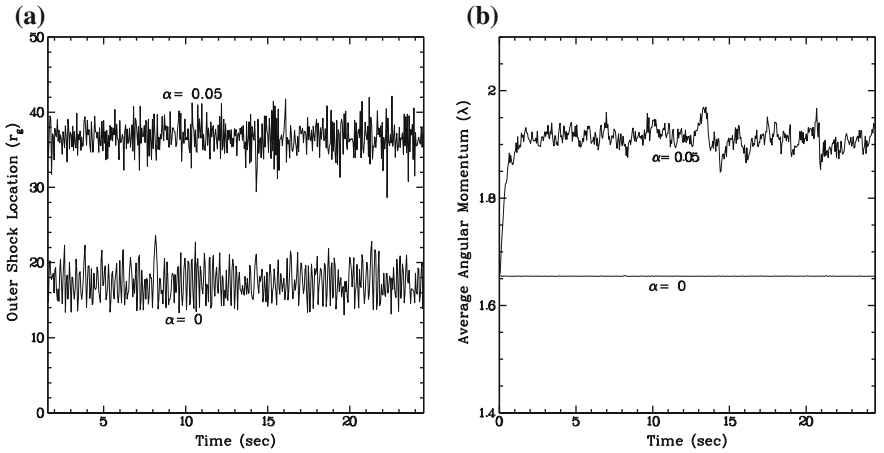

Fig. 6.12 **a** Time variation of outer shock locations (*left*) at equatorial plane and **b** averaged specific angular momentum (*right*) in the whole system at time 24.75 s. See text for details

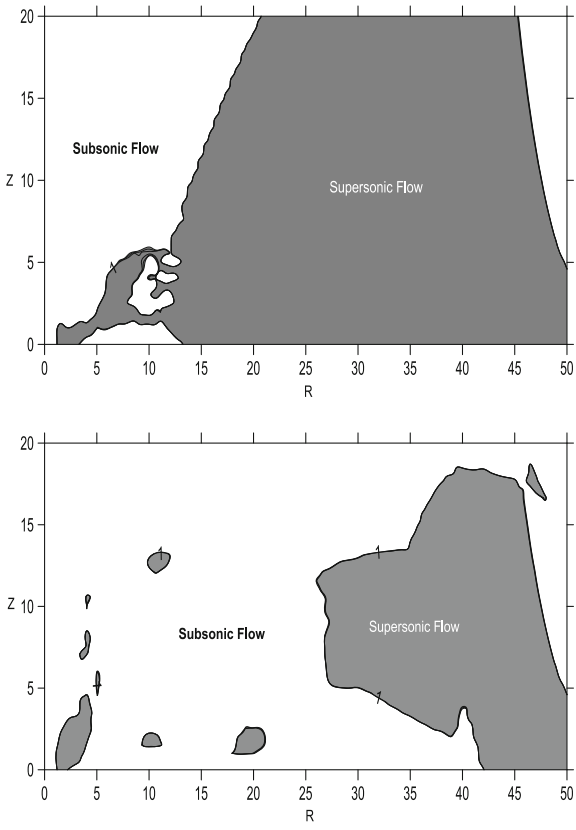

Fig. 6.13 Mach number distribution of inviscid (*top*) and viscous (*bottom*) flow at $r - z$ plane at the simulation time 24.75 s when the flow has achieved steady state

Like in previous cases, the shock locations shift outwards when viscosity is added. It is noted that when viscosity is absent in the flow, the average angular momentum of the system remains almost constant with injected value but increases when viscosity is incorporated in the system. Because of the transport of angular momentum, most of the matter being injected into the disc is not consumed by the black hole, which is indicated by the fact that $\bar{\lambda}$ is significantly higher than injected λ. We turn our focus on the time variation of temperature distribution of flow. So, one can easily perform the study with Mach number distribution of flows for different times of simulation.

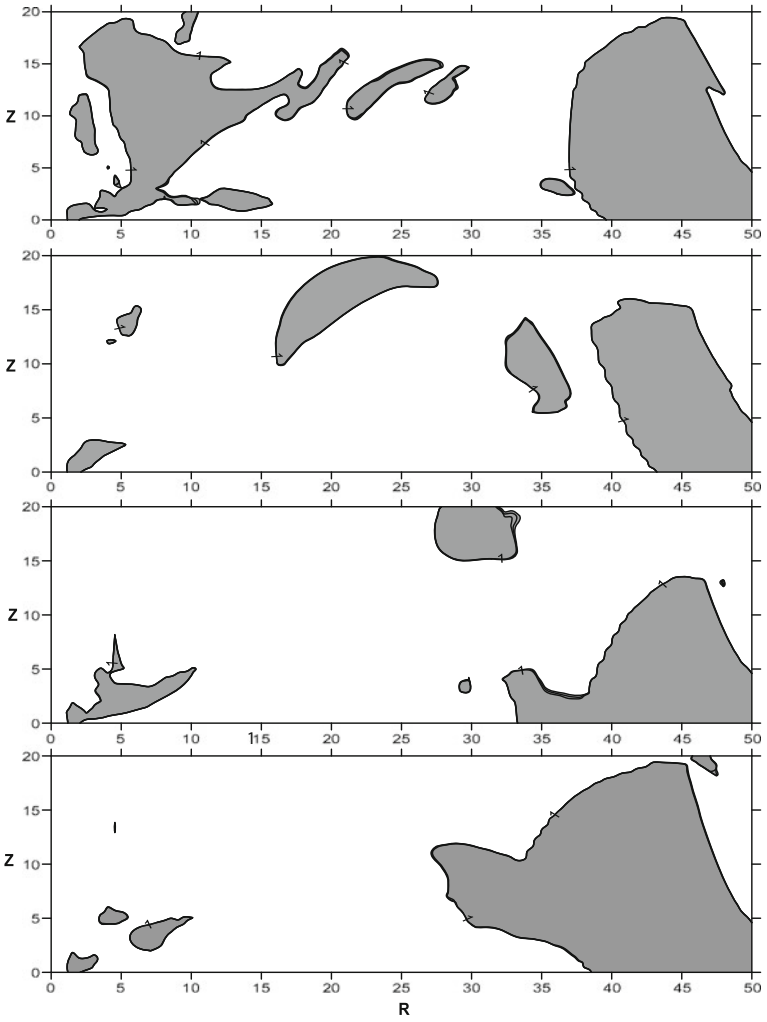

Fig. 6.14 Mach number distribution of a viscous flow on $r - z$ plane. From top to bottom, the successive maps are shown at different times of simulation. See text for details

The overall behaviour of Mach number is clear in Fig. 6.13 where the image map of the Mach numbers is plotted for both inviscid and viscous flows. We inject the matter supersonically at the outer boundary. At the top of Fig. 6.13, Mach numbers are shown on $r - z$ plane for inviscid flows, while the same for the viscous flow with $\alpha = 0.09$ are shown in the bottom of Fig. 6.13. Black-shaded regions represent the region where Mach number is greater than 1 (supersonic flow) and the white region is for Mach number less than 1 (subsonic flow). All the results are shown on the simulation time $T = 24.75$ s. The point of interest is that for viscous flows, the region nearer to the equatorial plane of the flow became subsonic from supersonic. The angular momentum of the system has been transported outwards with inclusion of viscous stress, and hence the flow nearer to a black hole as well as equatorial plane becomes subsonic. In the image map for viscous flows, we see that some isolated supersonic blobs are generated at the post-shock subsonic region. In case of higher viscosity, higher turbulences are also seen to form in the post-shock flow. This is because more matter from a higher elevation falls on the equatorial plane and converts the potential energy into heat and turbulent energy. We also tested that this kind of blob changes their nature, size and position with time evolution of the simulation. In Fig. 6.14, non-steady evolution of Mach number variation at $r - z$ plane of a viscous flow is shown. From the top to bottom, the image map of Mach numbers is plotted at the successive time $T = 9.90, 14.85, 19.8$ and 22.27 s respectively where $\alpha = 0.09$ for each cases. The black-shaded regions at each map stand for supersonic flow region, while the white-shaded regions represent subsonic flow. So it is evident that the isolated supersonic blobs change their location and size with time evolution. This kind of phenomena are expected to be reflected also in the spectral property of the flow.

6.4 Effects of Boundary Location

It may be noted that we have run the simulations above for viscosity parameters slightly below the critical viscosity, since the shock is approaching the outer boundary. As we have injection of matter at the outer boundary, it would prevent the shock from leaving the grid near the injection area. In order to prove that the shock actually runs away and disappears, one requires an infinitely large boundary which is impossible. However, that this must happen can be easily be shown by running a few cases using the viscosity parameter from both sides of the critical value. In Fig. 6.15a–b, we present two such cases with (a) $\mathcal{E} = 0.0035$, $\lambda = 1.66$, $x_b = 50$ and (b) $\mathcal{E} = 0.002$, $\lambda = 1.66$, $x_b = 100$. The viscosity parameters are marked on the curves. The critical viscosities are $\alpha_c \sim 0.0738$ and 0.0325 respectively. We clearly see that for $\alpha < \alpha_c$, the shock first goes out farther before returning and settling down at a certain finite distance with some small amplitude oscillation. However, for $\alpha > \alpha_c$, the shock never returns and continues to go outward. This behaviour is independent of the location of the boundary.

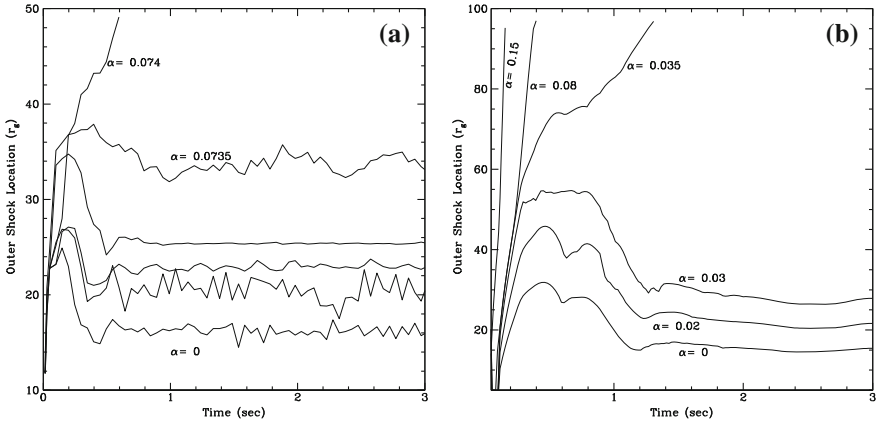

Fig. 6.15 Evolution of the shock location as the viscosity parameter α is changed for two different boundary conditions: **a** $x_b = 50$, $\mathcal{E} = 0.0035$, $\lambda = 1.66$; **b** $x_b = 100$, $\mathcal{E} = 0.002$, $\lambda = 1.66$. The critical viscosities are $\alpha_c = 0.0738$ and 0.0325 respectively in these cases. In both the cases, when $\alpha < \alpha_c$, the shock first goes out farther before returning and settling down, while for $\alpha > \alpha_c$, the shock never returns and continues to go outward (Giri and Chakrabarti 2012)

6.5 Effects of Viscous Stress Components

It is interesting to understand the importance of various components of viscous stress. We carried out simulations using the value of μ in Eq. (3.67) and either the $r\phi$ component of the viscous stress or all the components of the viscous term. We clearly find major differences in our results. These will be discussed now. In Fig. 6.16a–d, the radial distribution of the Mach number and the specific angular momentum on the equatorial plane and that averaged over 15 vertical grids from the equatorial plane are shown. The dash–dotted curve shows the results when only the $r\phi$ component is used and the solid curve shows the results when all the three components are used. The results are plotted at $t = 10$s. The flow parameters are $\mathcal{E} = 0.035$, $\lambda = 1.66$ and $\alpha_s = 0.03$. We also plot the results for the inviscid flows for comparison (dotted curve). Note that the distribution of angular momentum inside the shock remains almost constant when a single ($r\phi$) component is used while it becomes similar to Keplerian when all the three components are included. In Fig. 6.17a–d, we plot the distribution of density and velocity when only $r\phi$ component of the viscous stress is used (top left). Note that the jaggedness of the shock goes away when all three components of the viscous stress are included (top right). A density maximum occurs in the post-shock region. Thus, the post-shock region behaves like a thick accretion disc (Paczyński and Wiita 1980) as was also pointed out in SPH simulations (Molteni et al. 1994). The post-shock region, formed purely due to the centrifugal force, is known as the CENtrifugal pressure dominated BOundary Layer or CENBOL as mentioned earlier. This region is believed to be responsible to emit hard X-rays in black hole

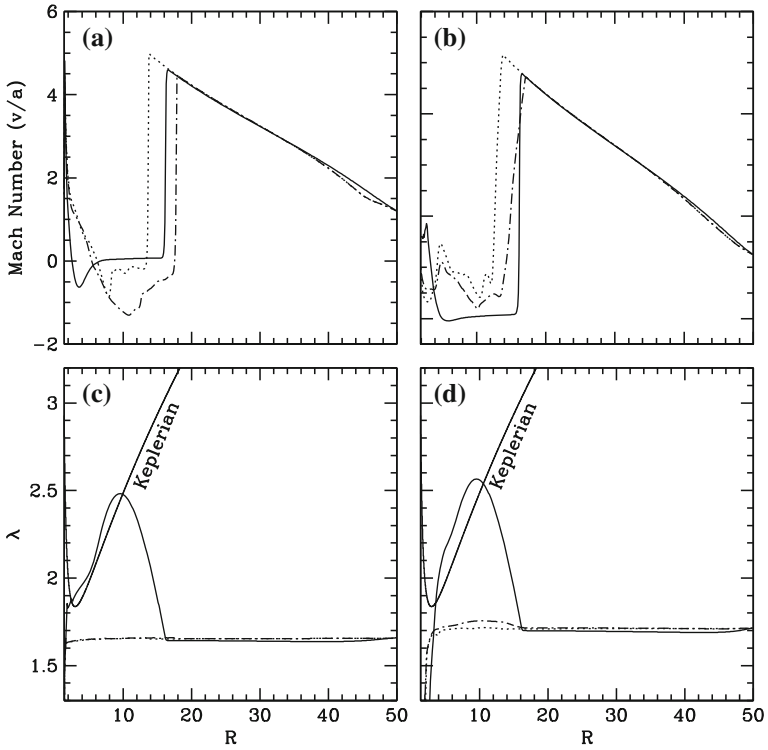

Fig. 6.16 Radial distribution of **a** & **b** Mach number, and **c** & **d** specific angular momentum on the equatorial plane **a** & **c** and that averaged over 15 vertical grids from the equatorial plane **b** & **d** for cases when only the $r\phi$ component (*dashed-dotted*) and all the three components (*solid*) are used. The results are plotted at $t = 10$s. We also plot the results for the inviscid flow for comparison (*dotted*). The angular momentum inside the shock remains almost constant when a single ($r\phi$) component is present, while it becomes similar to Keplerian when all the three components are included (Giri and Chakrabarti 2012)

candidates by inverse Comptonization of soft photons coming from Keplerian discs believed to form near the equatorial plane where the viscosity is high (Chakrabarti and Titarchuk 1995). The corresponding specific angular momentum distributions are in the bottom-left and bottom-right panels respectively. Note that up to the disc centre the angular momentum rises rapidly and becomes almost Keplerian as shown in Fig. 6.17c–d. The parameters chosen are the same as in Fig. 6.16. A comparison of the behaviour with and without all the three components indicates that the behaviour becomes smoother with transport of momentum taking place in all directions. The outflow also has a larger specific angular momentum.

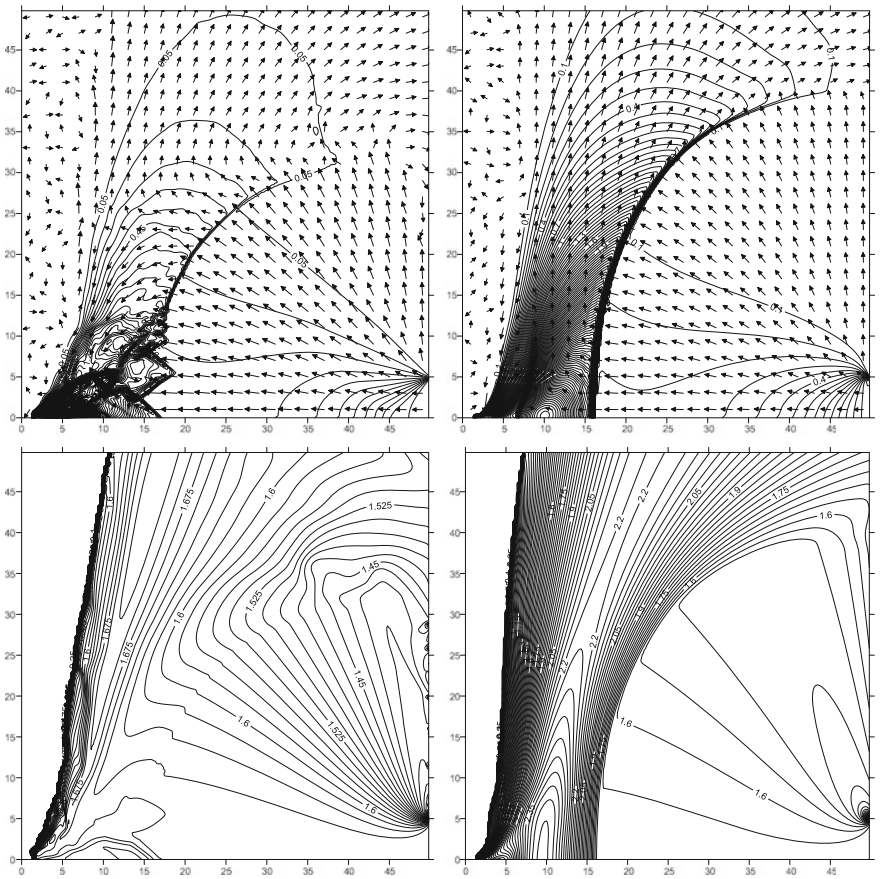

Fig. 6.17 Distribution of density and velocity when only $r\phi$ component of the viscous stress is used (*top left*). Note that the jaggedness of the shock goes away when all three components are included (*top right*). Density maximum and a consequent thick accretion disc-like structure is formed in the post-shock region in the latter case. The corresponding specific angular momentum distributions are at the *bottom left* and *bottom right* respectively. The parameters are the same as in Fig. 6.16 (Giri and Chakrabarti 2012)

References

Chakrabarti, S. K. (1989). *Astrophysical Journal*, *347*, 365.
Chakrabarti, S. K. (1990a). *Theory of transonic astrophysical flows*. Singapore: World Scientific.
Chakrabarti, S. K. (1990b). *MNRAS*, *243*, 610.
Chakrabarti, S. K., & Molteni, D. (1995). *MNRAS*, *272*, 80.
Chakrabarti, S. K., & Titarchuk, L. G. (1995). *Astrophysical Journal*, *455*, 623.
Chakrabarti, S. K. (1996). *Physics Report*, *266*, 229.
Chakrabarti, S. K. (1999). *Astronomy and Astrophysics*, *351*, 185.
Chakrabarti, S. K., & Das, S. (2004). *MNRAS*, *349*, 649.
Giri, K., & Chakrabarti, S. K. (2012). *MNRAS*, *421*, 666.

Igumenshchev, I. V., & Beloborodov, A. M. (1997). *MNRAS*, *284*, 767.
Igumenshchev, I. V., & Abramowicz, M. A. (2000). *Astrophysical Journal*, *130*, 463.
Lee, S. J., Ryu, D., & Chottopadhya, I. (2011). *Astrophysical Journal*, *728*, 142.
Molteni, D., Lanzafame, G., & Chakrabarti, S. K. (1994). *Astrophysical Journal*, *425*, 161.
Molteni, D., Ryu, D., & Chakrabarti, S. K. (1996). *Astrophysical Journal*, *470*, 460.
Paczyński, B., & Wiita, P. J. (1980). *Astronomy and Astrophysics*, *88*, 23.

Chapter 7
Effects of Power-Law Cooling in Viscous Flows

Abstract We carry out a series of numerical simulations of viscous accretion flows having a reasonable spatial distribution of the viscosity parameter. We add the power-law cooling throughout the flow. We show that in agreement with the theoretical solutions of viscous transonic flows, matter having viscosity parameter above a critical value becomes a Keplerian disc while matter having lesser viscosity remains a low angular momentum, sub-Keplerian flow. The latter component produces centrifugal pressure supported shock waves. Thus, for instance, flows having sufficiently high viscosity on the equatorial plane and low viscosity above and below, produce a Two Component Advective Flow (TCAF), where a Keplerian disc is surrounded by a rapidly moving sub-Keplerian halo. We find that the post-shock region of the Keplerian disc is evaporated and the configuration is stable. This agrees with the theoretical models which attempt to explain the spectral and timing properties of black hole candidates.

7.1 Introduction

In this chapter, we showed the results of simulations with low angular momentum, inviscid flows in two dimensions. Chakrabarti (Chakrabarti 1990a, b; Chakrabarti and Das 2001) predicted that the standing shocks are possible only when the viscosity parameters is less than a critical value $\alpha_{\rm crit}$ (which depends on other flow parameters). If α is above this critical value, the shock would move outward and the disc would become subsonic and Keplerian. In Chap. 6, we precisely see this. Radiative processes of course play an important role in shaping the flow geometry. If a flow is optically thick, the radiation is trapped and the matter is puffed up. If the matter is optically thin, radiation would leak out and the flow would be more or less isothermal. We have already seen that the viscosity transports angular momentum to make the flow Keplerian. But we can only have a Shakura–Sunyaev (Shakura and Sunyaev 1973) disc if the disc also cools appropriately.

Observation of non-thermal photons in the spectrum (Sunyaev and Truemper 1979) prompted the model builders to imagine that a hot electron cloud (the so-called Compton cloud) along with the standard disc could resolve the issue (Sunyaev

K. Giri, *Numerical Simulation of Viscous Shocked Accretion Flows Around Black Holes*,
Springer Theses, DOI 10.1007/978-3-319-09540-0_7

and Titarchuk 1980, 1985). Numerous suggestions and cartoon diagrams of the illusive Compton cloud are present in the literature (e.g., Zdziarski 1988; Haardt et al. 1994; Chakrabarti and Titarchuk 1995). Chakrabarti and Titarchuk (1995), based on the solutions of viscous and inviscid transonic flows around black holes (Chakrabarti 1989, 1990a, b) proposed that, in general, the accretion disc should really have two components: a Keplerian accretion on the equatorial plane and a sub-Keplerian halo that surrounds the Keplerian disc, and the puffed up inner part of the flow (CENBOL) which is nothing but the Compton cloud. The soft radiation coming from the Keplerian disc is intercepted by the hot sub-Keplerian flows in the CENBOL region and is re-radiated after multiple scattering. This radiative of the electron cloud. Depending on the relative importance of the Keplerian disc rate $\dot{M}_d$ and the sub-Keplerian halo rate $\dot{M}_h$, the electrons in the sub-Keplerian disc may lose (inverse Compton scattering) or gain (Compton scattering) energy. When the electron cloud gets hotter, the system is in the hard state and if the electron cloud cools down by losing energy to the photons, the system is in the soft state. The hard state is thus dominated by a power-law hard photon component.

The two component advective disc (TCAF) solution of Chakrabarti and Titarchuk (1995) was able to explain the spectral and timing properties including time lags observed in several black hole candidates (Wu et al. 2002; Smith et al. 2001a, b, 2002, 2007; Rao et al. 2000), there is as yet no work in the literature to show that the TCAF solution is stable. The cause for concern was obvious: a Keplerian disc is necessarily subsonic, while the sub-Keplerian flow is supersonic, and becomes subsonic only at the shock wave. The region between the shock wave and the sonic point near the horizon is known as the CENtrifugal pressure supported BOundary Layer or CENBOL. Thus, the questions that remain unanswered are: (a) Under what circumstances does TCAF actually form? (b) Would the Keplerian component remain stable when the sub-Keplerian component flies by or is it disrupted? (c) What is the fate of the inner Keplerian disc component when the hot CENBOL actually forms? (d) How would the subsonic Keplerian disc and the subsonic CENBOL interact, and finally (e) In presence of both the components how would the net angular momentum distribution of the flow behave?

In this chapter, we address these vital issues. Through numerical simulations of viscous accretion flow with power-law cooling effects, we show that when the injected sub-Keplerian flow angular momentum is high enough and/or the viscosity is high enough, TCAF would be formed, otherwise the sub-Keplerian flow would remain sub-Keplerian. The TCAF, when formed, is a stable configuration, i.e. the Keplerian component formed on the equatorial plane is not destroyed by the sub-Keplerian, fast moving halo component. We also show that the hot CENBOL effectively removes the Keplerian disc from the equatorial plane and the disc becomes truncated. In the work in this chapter, we carry out numerical simulation in the presence of both viscous and cooling effects. Physically, viscous heating increases post-shock pressure and also transports angular momentum faster. As a result, the Rankine-Hugoniot condition is satisfied away from the black hole. Cooling, on the other hand, reduces the post-shock pressure and the shock moves inward. With the combined effect, the shock may or may not move outward. Instead of using a constant α parameter throughout the

simulation grid, we assume that α is maximum on the equatorial plane and gradually goes down with vertical height (Giri and Chakrabarti 2013). We also use a power-law cooling process throughout the flow. We see that a cool, dense Keplerian disc is produced on the equatorial plane.

7.2 Computational Procedure

All the governing equations for viscous accretion flow are given in detail in Chap. 3 and we do not repeat it here. In Chap. 3, we presented the details of the implementation of power-law cooling within the viscous system. So, we do not repeat it here. Earlier, we had chosen a constant viscosity parameter α in the entire flow as is the trend in the subject. In this chapter, we have chosen a more realistic α parameter, so that the viscosity is high on the equatorial plane and low, away from from it. This is because, as is well known in the case of the models of the dwarf novae outbursts, the high viscosity on the equatorial plane actually drives the accretion (e.g., Cannizzo et al. 1982, 1995). Thus, the rate of transport of angular momentum on the equatorial plane should be the highest. Away from the plane, the pressure falls very slowly, and thus in order to reduce viscous effects, α itself must go down also. In the present work, instead of using the same α for the whole $r - z$ plane, we choose a smooth distribution as

$$\alpha = \alpha_{\max} - \left[\alpha_{\max}\left(\frac{z}{r_{\max}}\right)^{\delta}\right], \tag{7.1}$$

where, $r_{\max} = 200$, $0 \leq z \leq 200$ and $\delta > 0$. In our case, we have chosen $\delta = 1.5$. In Fig. 7.1 we show how α changes in the z direction. Clearly, when $z = 0$, i.e. at equatorial plane, $\alpha = \alpha_{\max} = 0.012$, while $\alpha = 0$ for $z = z_{\max} = r_{\max}$. If turbulence is the major source of viscosity, then, clearly it will be highest on the equatorial plane. But a precise knowledge is required to get the distribution of how alpha actually falls with height. That is why we assume a generic distribution. Since we have no preferred choice one way or another, we ran our code with several distributions of similar nature, but the basic result was found to remain the same. We have also chosen $\alpha_{\max} > \alpha_{\rm crit}$ so that on the equatorial region the flow can transport angular momentum efficiently and form a Keplerian disc .

The set-up of our simulation has been described in Chap. 4. Instead of only viscous flows, we add a power-law cooling in the Pseudo-Newtonian gravitational field of a point mass M_{bh} located at the centre in cylindrical coordinates $[r, \theta, z]$. The numerical calculation has been carried out with $r_o = 200 r_g$ and $N_r = N_z = 512$. Thus, each grid has a size of 0.39 in units of the Schwarzschild radius. Considering that we are interested in the shock formation that takes place at a few tens of Schwarzschild radii away and this grid size should be sufficient for this purpose. We typically find that the infall time from the outer to the inner boundary is about $\sim$0.5 s. This is

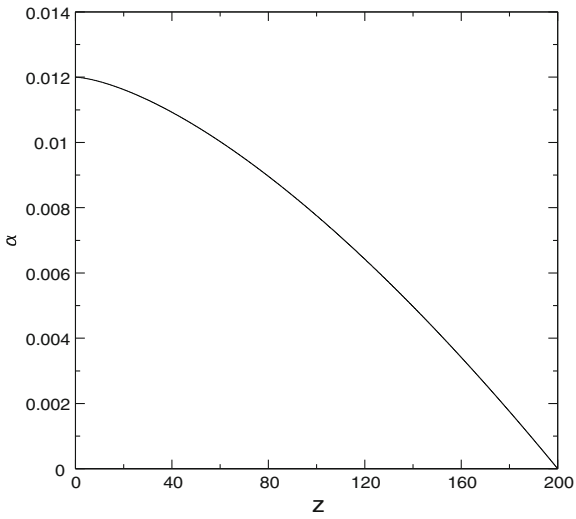

Fig. 7.1 Distribution of viscous parameter α along z direction. $\alpha_{\max} = 0.012$ is taken

computed from the sum of $\mathrm{d}r/<v_r>$ over the entire radial grid, $<v_r>$ being averaged over 20 vertical grids. In this work, we are interested to show (a) the formation of CENBOL (at tens of Schwarzschild radii) and (b) the formation of a Keplerian disc (few Schwarzschild radii thick). So, the resolution that we have ($\sim$0.4 Schwarzschild radii) is enough to catch these salient features. For a detailed study of turbulent cells, we require to refine the grids. This will be done in the future. In order to mimic the horizon of the black hole at one Schwarzschild radius, we placed an absorbing inner boundary at $R = 2.5r_g$, inside which all material is completely absorbed into the black hole. All the simulations have been carried out assuming a stellar mass black hole ($M = 10M_{\odot}$). We carry out the simulations for several hundreds of dynamical timescales. In reality, our simulation time corresponds to a few seconds in physical units. Now, we present the results for different cases as well as different sets of parameters.

7.3 Simulation Results

We assume the flow to be in vertical equilibrium (Chakrabarti 1989) at the outer boundary. The injection rate of the momentum density is kept uniform throughout the injected height at the outer edge. We inject through all the radial grids. We stop the simulations at $t = 95$ s. This corresponds to more than two hundred times the dynamical time of the flow. Thus, the presented solutions are at a time long after the transient phase. The results of the simulation are discussed below. First, we perform two-dimensional numerical simulations with viscosity and cooling for different values of specific angular momentum $\lambda = 1.3$, 1.5 and 1.7. In the absence

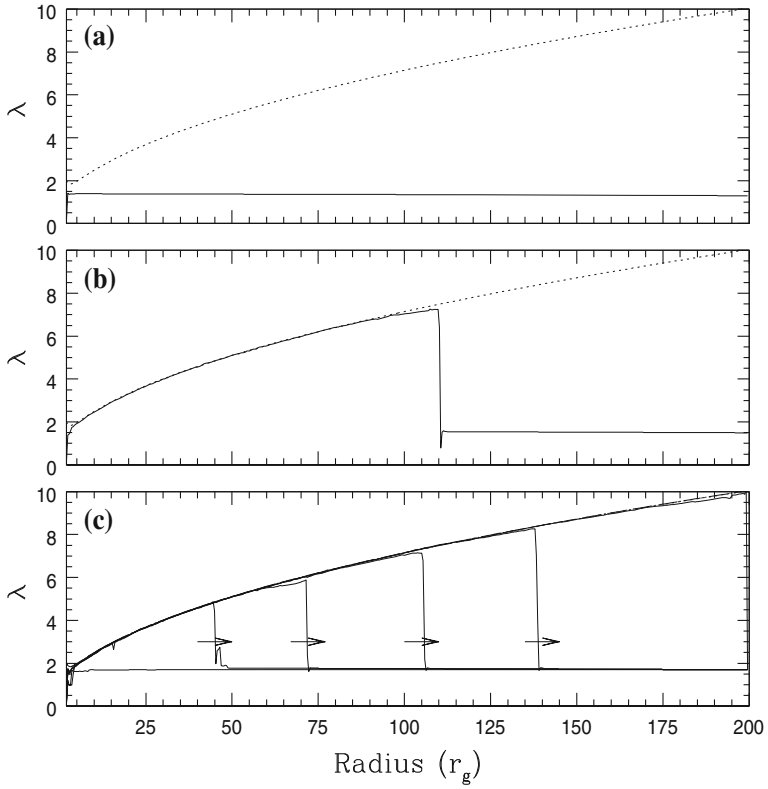

Fig. 7.2 A comparison of the specific angular momentum distribution (*solid curves*) with injected **a** $\lambda = 1.3$, **b** 1.5 and **c** 1.7 when the viscosity and the cooling effects are included. The results are compared with the Keplerian angular momentum distribution (*dotted curves*). Note that, in **b**, the Keplerian disc reaches till $\sim 110 r_g$. In **c**, however, the Keplerian disc reaching towards the grid boundary. The *vertical* boundaries are at $t = 23.71, 35.57, 47.43, 73.34$ and 95 s, respectively (Giri and Chakrabarti 2013)

of viscosity, the angular momentum would have remained the same as that of the injected value. In Fig. 7.2a–c, we show the distribution of specific angular momenta (solid curve) with Keplerian angular momentum distribution (dotted curve) on the equatorial plane when viscosity and cooling effects are added. The specific energy ($\mathcal{E}$) of the flow at the equatorial plane ($z = 0$) was chosen to be 0.001 at the outer boundary. The viscosity parameter was chosen to be, $\alpha_{\rm max} = 0.012 > \alpha_{\rm crit}$ and the cooling index was chosen to be $\beta = 1$. In all the cases, the transient behaviours are over within 1 s. In (a), where $\lambda = 1.3$, the angular momentum transport rate is negligible even when viscosity and cooling are added. But the rate is significant for the intermediate value: $\lambda = 1.5$ (b). For a large $\lambda = 1.7$, the angular momentum has been transported rapidly and the distribution of specific angular momentum in (c) coincides with its Keplerian value. From left to right, we have plotted for $t = 23.7$,

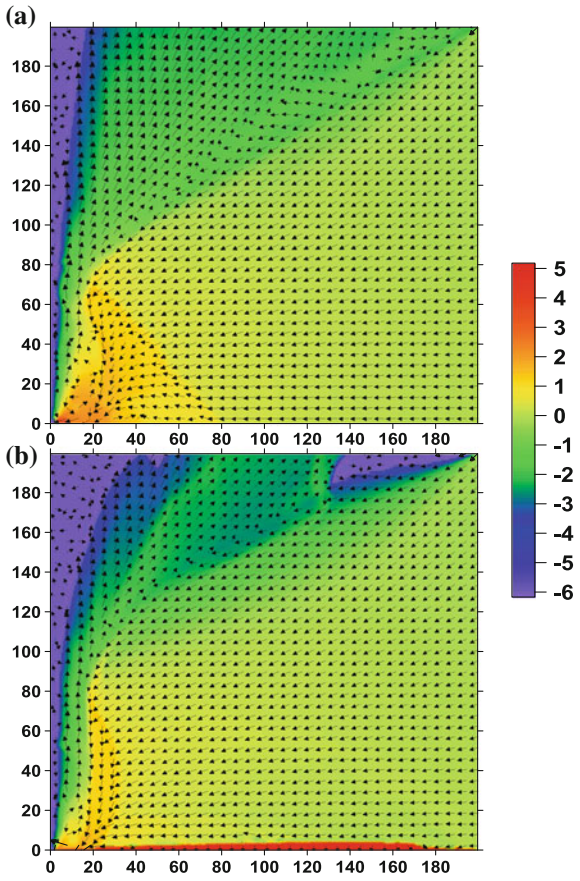

Fig. 7.3 Changes in the density and velocity distributions at $t = 95$ s **a** without and **b** with the inclusion of viscosity and cooling. Densities in normalised units are plotted in logarithmic scale as in the scale on the *right*. The density ranges from $\log_{10}\rho = -6$ to 5 in both the figures. A two-component flow is clearly formed in **b** (Giri and Chakrabarti 2013)

$t = 35.6$, $t = 47.4$, 73.3 and 95 s, respectively. In (a), the shock does not exist for such low angular momentum flow (Chakrabarti 1989). So, the case will never produce any Keplerian disc also. Both (b) and (c) produce shocks as they have sufficient angular momentum. While in (b) the shock remains standing forever, in Fig. 7.2c the shock propagated outward and the whole disc becomes Keplerian. The reason is that $\alpha < \alpha_{\rm crit}$ in (b) and $\alpha < \alpha_{\rm crit}$ in (c). In (c) if we run longer, the shock will propagate to large distance making the whole post-shock region a Keplerian disc. Only the region between the horizon and the inner sonic point ($\sim 2.5 r_g$) will remain supersonic and sub-Keplerian. Figure 7.3a–b shows the velocity and density distribution of the flow (a) without viscosity and cooling and (b) with viscosity and cooling. In order to have meaningful comparison, all the runs were carried out up to $t = 95$ s. For both the cases, $\lambda = 1.7$ and $\mathcal{E} = 0.001$ were chosen. In Fig. 7.3b, we take $\alpha_{\rm max} = 0.012$ and $\beta = 1$. The α is higher than $\alpha_{\rm crit}$ for the respective flow parameters. The density distributions in Fig. 7.3 are plotted in the logarithmic scale shown on the right. We note that on the equatorial plane, a Keplerian disc has formed out of

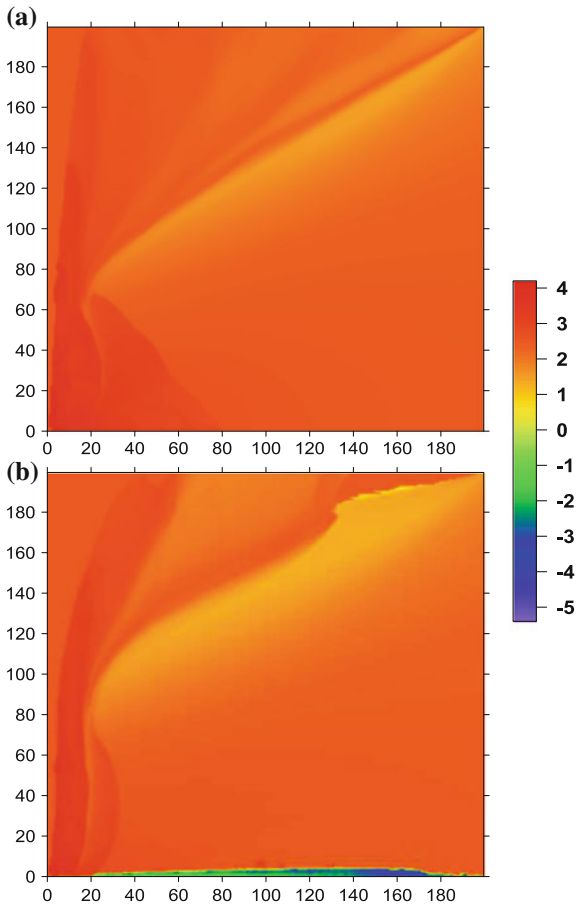

Fig. 7.4 Temperature distribution with logarithmic scale for non-viscous and viscous cases. For both the cases, the temperature ranges from $\log_{10} T = -5$ to 4.1 (Giri and Chakrabarti 2013)

the sub-Keplerian matter. Close to the outer boundary, near the equatorial plane, we are injecting sub-Keplerian matter and thus the Keplerian disc is disrupted there. In the realistic case, where the boundary is very far so that the equatorial injected matter itself is Keplerian, no such disruption should be seen. In other words, the apparent disruption of the Keplerian disc is an artefact of the simulation method. In Fig. 7.4a–b, we show the temperature distributions in keV as per colour (logarithmic) scale on the right. In the absence of cooling and viscosity, in Fig. 7.4a, the single component sub-Keplerian flow forms. In Fig. 7.4b, because of higher viscosity, flows have the Keplerian distribution near the equatorial region. Because of cooling effects, the region with a Keplerian distribution is cooler and denser. Comparatively, low-dense sub-Keplerian matter stays away from the equatorial plane. For both the cases, the Centrifugal Pressure supported BOundary Layer (CENBOL) forms. Since the inner boundary condition on the horizon forces the flow to be sub-Keplerian irrespective of their origin (Chakrabarti 1990b, 1996), the Keplerian and sub-Keplerian matter

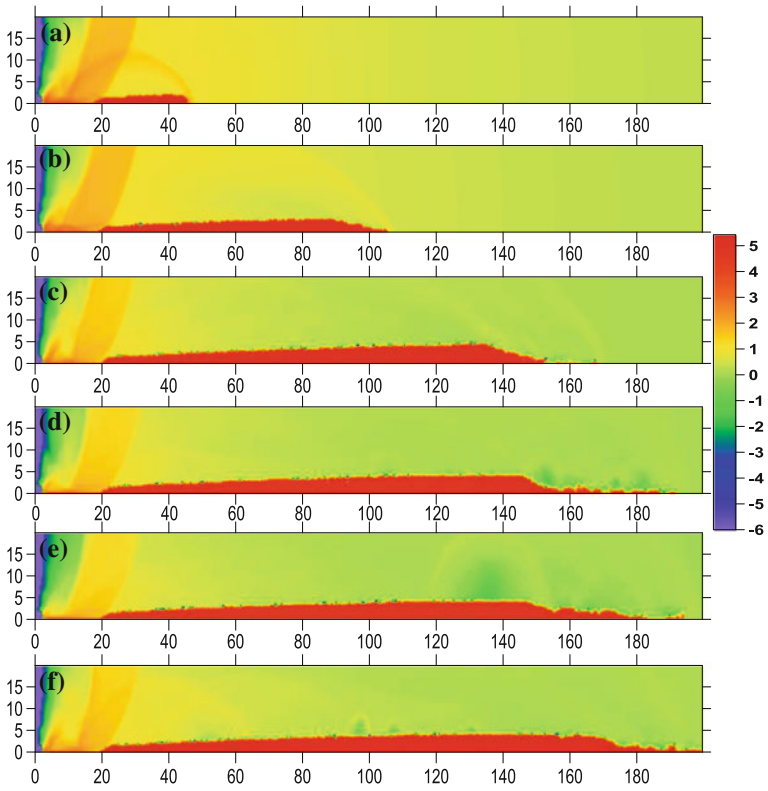

Fig. 7.5 Time variation of density distribution (in logarithmic scale) at six different times: $t = 20, 50, 70, 80, 90$ and 95 s. The density range from $\log_{10}\rho = -6$ to 5.2. The CENBOL forms at $r \sim 20$ (Giri and Chakrabarti 2013)

mixes (at the location of shock) before entering into a black hole to form a single component sub-Keplerian flow which is the CENBOL. A standard Keplerian disc forms in two steps: (a) The viscosity must be sufficiently high ($\alpha > \alpha_{\rm crit}$ as discussed in Paper II) to produce a Keplerian distribution and (b) The cooling must be sufficiently high to emit a black body locally. In order to show how the Keplerian disc actually forms out of a sub-Keplerian flows, in Fig. 7.5, we zoom the region close to the equatorial plane and show the results at six different times: $t = 20, 50, 70, 80, 90$ and 95 s. Different colours correspond to different densities as marked in the scale on the right. The red colour corresponds to $\sim 10^5$, while yellowish green corresponds to ~ 1, the injected density. The CENBOL is at $r \sim 20$ where the density increases by a factor of a few. Injected matter near the equatorial plane being strongly sub-Keplerian disrupts the Keplerian disc in the region $r \sim 180 - 200$. Note that the formation of Keplerian disc is slow compared to the inflow velocity of the sub-Keplerian matter. In the frame of the sub-Keplerian matter, the Keplerian disc behaves as an obstacle. This causes the formation of a wake at the tip of the Keplerian flow. If one starts

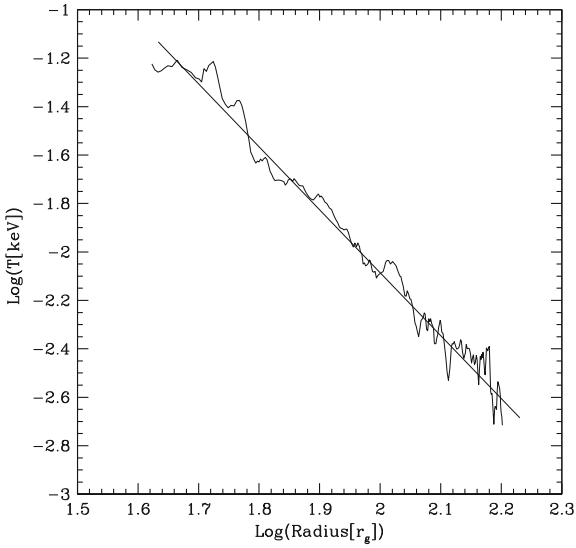

Fig. 7.6 Log–log plot of the radial distribution of time averaged temperatures (in keV) of the Keplerian component at $t = 95$ s. The slope γ of the power-law distribution $T(r) \sim r^{-\gamma}$ is 2.6 (Giri and Chakrabarti 2013)

with a Keplerian disc and gives no viscosity, the disc will immediately accrete and it will not remain Keplerian. So a disc can be Keplerian even without cooling. But a disc cannot remain Keplerian without sufficient viscosity. We have already shown in Fig. 7.2 that the angular momentum distribution of the flow close to the equatorial plane is indeed Keplerian as far as the Keplerian component goes. Now, we wish to show how the temperature is distributed. In the standard Keplerian disc (Shakura and Sunyaev 1973), in the optically thick regime, the black body cooling law $\propto T(r)^4$ leads to the disc temperature distribution of $T(r) \sim r^{-3/4}$. However, the cooling we employ here is $\propto T(r)^\beta$, where $\beta = 1$. This leads to a possible distribution of $T(r) \sim r^{-3}$, steeper than a Keplerian disc emitting black body. In Fig. 7.6, we plot the radial distribution of vertically averaged temperature at $t = 95$ s. We have plotted between 30 and $150r_g$ to avoid the boundary effects. The temperature just outside CENBOL at $r \sim 20r_g$ is found to be around 0.1 keV. The slope of the distribution ($T(r) \sim r^{-\gamma}$) is found to be $\gamma = 2.6$. This converged result is close to our predicted value. In the future, when we add the Comptonization scheme inside the simulation, we anticipate that $T(r) \sim r^{-3/4}$ distribution would be achieved. An important question in this context is: Are the Keplerian disc formation and destruction times the same, or are there some hysteresis effects? This issue is important since in the outbursting black hole candidates, the rising and declining phases take totally different times (Chakrabarti et al. 2009; Debnath et al. 2010). To see whether there is a hysteresis effect or not, we carry out a numerical experiment where we first allow the Keplerian disc to form and then remove the viscosity so that the angular momentum transport is not possible. In Fig. 7.7a–d, we show results of the simulations (with parameters the same as in Fig. 7.5 at (a) $t = 23.7$ s and (b) $t = 59$ s, respectively. The density scale is shown on the right (logarithmic). Now starting with the output of

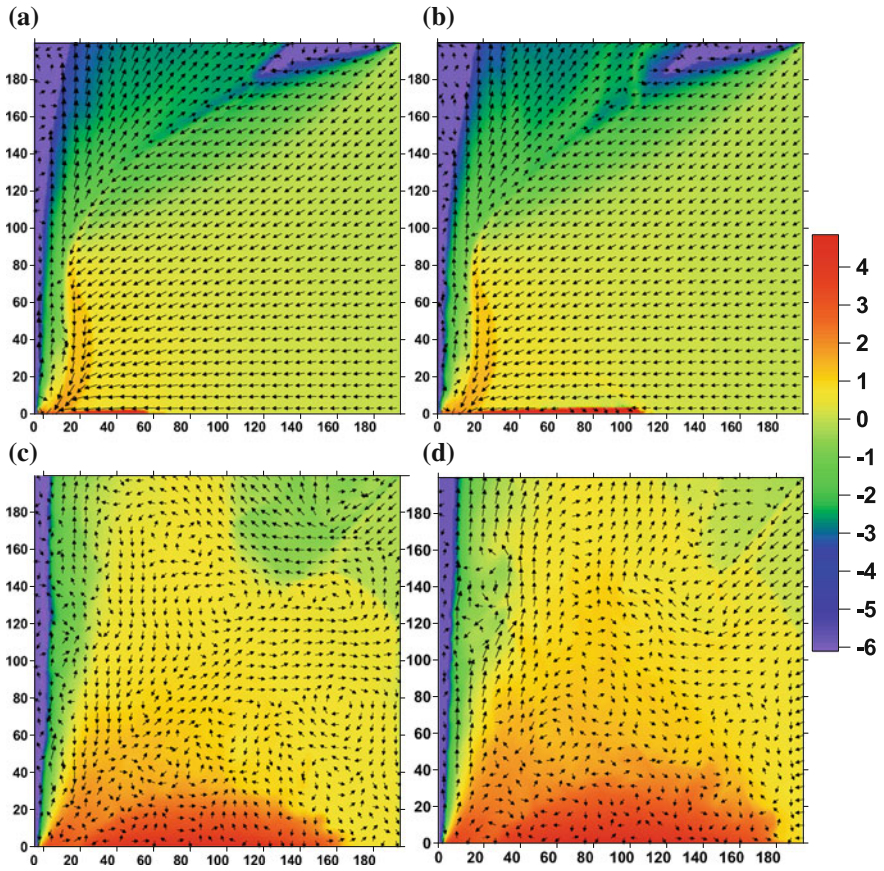

Fig. 7.7 **a**–**b** Formation of a Keplerian disc from the injected sub-Keplerian flow in the presence of viscosity and cooling effects: **a** at $t = 23.7$ s and **b** at $t = 59$ s. **c**–**d** Evaporation and mixing of the Keplerian disc started after removal of cooling and viscosity: **c** at $t = 95$ s and **d** $t = 118$ s. For all cases, density ranges from $\log_{10}\rho = -6$ to 5 (Giri and Chakrabarti 2013)

(b), we remove the viscosity and cooling and run again for another 59 s. In Fig. 7.7c, we show the results at $t = 95$ s and in Fig. 7.6d we show the results at $t = 118$ s. We note that turbulent cells are produced all over the flow and the flow pattern is greatly disturbed. Most interestingly, if there were no hysteresis effects, Fig. 7.7b, c would have been alike and Figs. 7.3a and 7.7d would have been alike. However, they are not. Naturally, the spectrum would also have the corresponding effects. Clearly, we need to carry the simulation for a much longer time to bring back the CENBOL in the inviscid flow as in Fig. 7.3a. In the outburst sources (Mandal and Chakrabarti 2010), exactly the same hysteresis effect can be seen. The time variation of the Keplerian and the sub-Keplerian flows do not obey the same route in the onset and the decline phases of the outbursts.

7.3.1 Time Variation of Matter Contents in the Keplerian and Sub-Keplerian Components

It is interesting to study the time variations of the matter contents of the Keplerian ($M_{\rm kep}$), the sub-Keplerian ($M_{\rm subkep}$), the outflowing matter ($M_{\rm out}$) and the total matter ($M_{\rm tot}$) in the system. Let us define the quantity of the total matter in the system in dimensionless units. The total matter of the system for a particular time of run is defined by $M_{\rm tot} = \Sigma(2\pi r{\rm d}r{\rm d}z\rho)$, where the summation is taken for all grids in the system. We have taken $\delta_\lambda = |\lambda_{\rm kep} - \lambda_{\rm run}|$, where, $\lambda_{\rm kep}$ and $\lambda_{\rm run}$ are Keplerian-specific angular momentum and specific angular momentum obtained from our simulation, respectively. We have calculated δ_λ for each grid point of our simulation box. So, if δ_λ is very small for a grid point, then this grid point is said to be part of the Keplerian disc. The total Keplerian matter is defined as $M_{\rm kep} = \Sigma(2\pi r{\rm d}r{\rm d}z\rho)$, where the summation is taken only for those grids when $\delta_\lambda < 0.02$. The total outflowing matter of the system is defined as $M_{\rm out} = \Sigma(2\pi r{\rm d}r{\rm d}z\rho)$, where, $\delta_\lambda < 0.02$ and $v_z > 0$. Hence, total sub-Keplerian matter of the system is defined as $M_{\rm subkep} = M_{\rm tot} - (M_{\rm kep} + M_{\rm out})$. In Fig. 7.8, we plot the time variations of total ($M_{\rm tot}$), Keplerian ($M_{\rm kep}$) and sub-Keplerian ($M_{\rm subkep}$) matter of the flow with viscosity and cooling. The solid curve represents the total

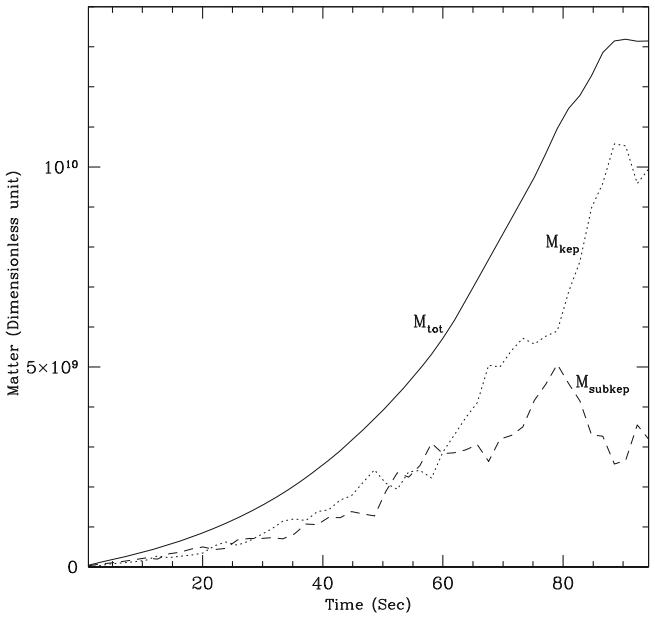

Fig. 7.8 Time variations of the Total ($M_{\rm tot}$), Keplerian ($M_{\rm kep}$) and sub-Keplerian ($M_{\rm kep}$) matter of the system at a given instant. The *solid curve* represents the total matter of the system with time, while *dotted* and *dashed curve* represents the variation of Keplerian and sub-Keplerian matter, respectively

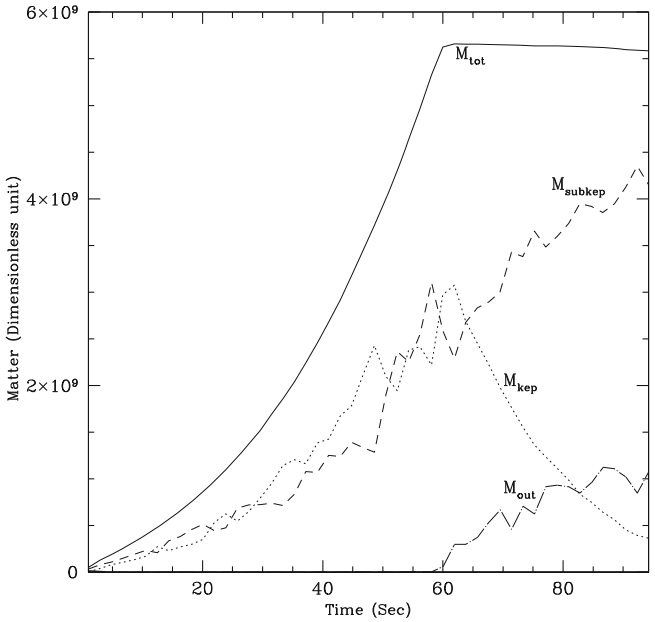

Fig. 7.9 Time variations of the total, Keplerian, sub-Keplerian and outflowing matter in the system. See text for details

matter of the system with time, while dotted and dashed curves represent the variation of Keplerian and sub-Keplerian matter, respectively. In that case, outflowing matter is so less that it is neglected. Here, for both the cases, $\lambda = 1.7$ and $\mathcal{E} = 0.001$, $\alpha_{\max} = 0.012$ and $\beta = 1$. In comparison, in Fig. 7.9, time variations of $M_{\rm tot}$, $M_{\rm kep}$, $M_{\rm subkep}$ and $M_{\rm out}$ are shown for the flow which is started initially with viscosity and cooling (from $t = 0$ to $t = 61$) and then without viscosity and cooling ($t = 61$ to $t = 94.86$). It is clear that the Keplerian matter is increasing in the system until the viscosity and cooling are switched off, while the reverse is true for the sub-Keplerian matter and outflows.

7.4 Comparison of Our Result with Other Models

It is pertinent to compare our results with the results of some of the previous studies. Igumenshchev and Abramowicz (1999, 2000), Stone et al. (1999), Proga and Begelman (2003) do not find the existence of shocks. In their simulations, the authors mainly concentrated on the time evolution of injected Keplerian or almost Keplerian disc . As the Keplerian flow itself is a subsonic flow, the time evolution of the Keplerian flow will not produce a shock. These simulations were also viscous, so a Keplerian flow remained Keplerian until the inner sonic point. By contrast, our

flows are advective with a significant radial velocity component and the flow has angular momentum much less than that of the Keplerian disc. With the addition of viscosity, the distribution becomes Keplerian along the equatorial plane and the cooling ensures that this Keplerian flow indeed radiates like a standard Keplerian disc. Since above and below the equatorial plane the density is low, the viscosity and cooling are inefficient, the flow remains sub-Keplerian and produces shocks. So, we have a complete solution in which the equatorial part behaves like a Keplerian disc, while the other part away from the equatorial plane behaves like a transonic flow with shock waves.

It is evident that the outflows are generated from inflow at both Fig. 7.3a, b. The centrifugal barrier (CENBOL) produces shock and the post-shock flow become hot. Due to heating at the jet-base (CENBOL) and subsequent expansion in the vertical direction, the outflow is generated from the disc. The excess thermal gradient force along the vertical direction in the post-shock flow drives a part of the accreting matter as the bipolar outflow which is believed to be the predecessor of the observed jet. We thus have the indication that the shock heating is an important ingredient in the ejection of matter from the disc surface. Indeed in the presence of cooling, the outflow is found to be quenched (Garain et al. 2012).

References

Cannizzo, J. K., Ghosh, P., & Wheeler, J. C. (1982). *Astrophysical Journal*, *260*, 83.
Cannizzo, J. K., Chen, W., & Livio, M. (1995). *Astrophysical Journal*, *454*, 880.
Chakrabarti, S. K. (1989). *Astrophysical Journal*, *347*, 365 (C89).
Chakrabarti, S. K. (1990a). *Theory of transonic astrophysical flows*. Singapore: World Scientific (C90a).
Chakrabarti, S. K. (1990b). *MNRAS*, *243*, 610 (C90b).
Chakrabarti, S. K. (1996). *Physics Reports*, *266*, 229 (C96).
Chakrabarti, S. K., & Das, S. (2001). *MNRAS*, *327*, 808 (CD01).
Chakrabarti, S. K., & Titarchuk, L. G. (1995). *Astrophysical Journal*, *455*, 623 (CT95).
Chakrabarti, S. K., Dutta, B. G., & Pal, P. S. (2009). *MNRAS*, *394*, 1463.
Debnath, D., Chakrabarti, S. K., & Nandi, A. (2010). *Astronomy and Astrophysics*, *520*, 98.
Garain, S., Ghosh, H., & Chakrabarti, S. K. (2012). *Astrophysical Journal*, *758*, 114.
Giri, K., & Chakrabarti S. K. (2013). *MNRAS*, *430*, 2836 (GC13).
Haardt, F., Maraschi, L., & Ghisellini, G. (1994). *Astrophysical Journal*, *432*, 95.
Igumenshchev, I. V., & Abramowicz, M. A. (1999). *MNRAS*, *303*, 309.
Igumenshchev, I. V., & Abramowicz, M. A. (2000). *Astrophysical Journal*, *130*, 463.
Mandal, S., & Chakrabarti, S. K. (2010). *Astrophysical Journal*, *710*, 147.
Proga, D., & Begelman, M. C. (2003). *Astrophysical Journal*, *69*, 81.
Rao, A. R., Yadav, J. S., & Paul, B. (2000). *Astrophysical Journal*, *544*, 443.
Shakura, N. I., & Sunyaev, R. A. (1973). *Astronomy and Astrophysics*, *24*, 337 (SS73).
Smith, D. M., Dawson, D. M., & Swank J. H. (2007). *Astrophysical Journal*, *669*, 1138.
Smith, D. M., Heindl, W. A., & Swank J. H. (2001a). *AAS*, *33*, 1473.
Smith, D. M., Heindl, W. A., & Swank J. H. (2002). *Astrophysical Journal*, *569*, 362.
Smith, D. M., Heindl, W. A., Markwardt, C., & Swank, J. H. (2001b). *Astrophysical Journal*, *554*, L41.
Stone, J. M., Pringle, J. E., & Begelman, M. C. (1999). *MNRAS*, *310*, 1002.

Sunyaev, R. A., & Truemper, J. (1979). *Nature*, *279*, 506.
Sunyaev, R. A., & Titarchuk, L. G. (1980). *Astronomy and Astrophysics*, *86*, 121.
Sunyaev, R. A., & Titarchuk, L. G. (1985). *Astronomy and Astrophysics*, *143*, 374S.
Wu, K., Soria, R., Campbell-Wilson, D., Hannikainen, D., Harmon, B. A., Hunstead, R., et al. (2002). *Astrophysical Journal*, *565*, 1161.
Zdziarski, A. (1988). *MNRAS*, *233*, 739.

Chapter 8
Conclusions and Future Plans

Abstract We draw concluding remarks and briefly mention our future plans.

The goal of my thesis was to study accretion flows around black holes with a two-dimensional axisymmetric system, and to understand the effects of viscosity and cooling on the time evolution of these discs. The first step towards this accomplishment was the development of a numerical hydrodynamics computer code, which can calculate the gravitational forces, centrifugal forces and inertial forces that decide on the dynamics of a given system. The numerical hydrodynamics were added to an already existing standard code developed by Ryu et al. (1993), and the method chosen was Total Variation Diminishing (TVD). A black hole system in general is relativistic in nature. In our work, we have used a pseudo-Newtonian potential (Paczyński and Wiita 1980), which mimics the space time of a Schwarzschild black hole.

In the Introduction chapter, we briefly introduced black holes and the general concept of accretion processes around black holes. To avoid complexity, we studied accretion processes in a strong gravitational field by considering the pseudo-Newtonian potential. A discussion of the Paczyński and Wiita (1980) potential was presented in Sect. 1.2. Next, we mentioned the fluid dynamical aspects of an accretion flow. In Sect. 1.5, we discussed the accretion shocks close to the black hole horizon. We discuss the genesis of shock conditions and the reason for formation of shocks. We presented shock conditions of different limits and studied the nature of Rankine-Hugoniot shocks for the accretion and winds around a compact object. The importance of hydrodynamics and numerical simulations is pointed out. There are quite a few accretion disc models present in the literature. We have listed some of the basic accretion disc models in Sect. 1.8, starting from a Bondi flow. In this section, we discussed the path breaking work of accretion process where a brief description of thin accretion disc model, commonly known as the 'standard Keplerian disc'. This model, although explaining the luminosity shown by black hole candidates fails to produce the high-energy power-law tail of the spectrum shown by most black holes candidates. More importantly, in this model, accretion disc is terminated at the marginally stable orbit, and the inner boundary conditions are not satisfied since the advection of flow was completely ignored. Therefore, the basic requirement of the accretion process around black hole, i.e. the transonic property,

K. Giri, *Numerical Simulation of Viscous Shocked Accretion Flows Around Black Holes*,
Springer Theses, DOI 10.1007/978-3-319-09540-0_8

is not satisfied in this model and we proceeded further for future development of this subject. Next, we presented another disc model known as the 'Thick disc,' which have a few interesting features such as the production of supercritical luminosity, its ability of jet collimation, etc. In Sect. 1.8.5, we pointed out advective discs models. In the last section of the Introduction, we presented the most general form of the accretion disc model, namely the Two Component Advective Flows or TCAF. This disc model is obtained from the actual solution of governing equations, and it satisfies all the boundary conditions of accretion processes onto black holes. TCAF explains the observed spectral properties, the state transition, the variability class transitions, quasi-periodic variations, etc.

In Chap. 2, we give an overview of numerical simulations of accretion processes around black holes since the last three decades. We then present the goals of my thesis. At the end of this chapter, we discuss the units and dimensions we used in our simulations.

In Chap. 3, we investigated hydrodynamic simulations of accretion flows around black holes. We presented the conservation equations for inviscid flows in compact form. Next, we stated numerical approaches for solving these equations. We then show the details of the structure of the equations for non-viscous system in our simulations. We derived all the eigenvalues and the corresponding left and right eigenvectors. So the solution method reduces to an eigenvalue problem. We then discuss the TVD method by which we obtained the solutions from the eigenstructure. Next, we incorporate turbulent viscosity in our system. We compare between the set of equations of viscous flows and non-viscous flows. We pointed out how molecular viscosity is negligible for accretion flows. Next, we include a simple power-law cooling in our viscous flows. We show how the energy equations change with the inclusion of cooling term.

In the next chapter, we describe the simulation procedure in detail. We discuss the geometry, computational box that we have used in our simulations. We then give the details of the initial and boundary conditions. We make some comments on timescales and code parameters used in our simulations. At the end of the chapter, we show some results of simple cases to check the validity of our code. We simulate the exact Bondi flow solutions with our code and compare the results from the numerical simulations with the theoretical results.

In an accretion flow, the study of standing and oscillatory shocks are of great importance and they decide the spectral and temporal properties of a spectrum emitted from the accretion flows. In Chap. 5, we presented the results of two-dimensional hydrodynamic simulations of matter accreting onto a black hole. We systematically chose the flow parameters $(\mathcal{E}, \lambda)$ from the parameter space, which provides the complete set of solutions of a black hole accretion flow. The parameter space was classified into regions, which may or may not produce standing shocks (Chakrabarti 1989, 1990) in an inviscid flow. The classifications were made using three different models of the flow, namely a disc of constant thickness, a disc with conical wedge cross-section and a disc that is in vertical equilibrium (Chakrabarti and Das 2001). Our motivation was to study whether a simulated result behaves like any one of these theoretical models throughout. We observed that the flow behaved like that of the

constant thickness before the shock. However, in the post-shock region, as the flow expands vertically due to higher thermal pressure, it behaves like that of a flow in vertical equilibrium. Second, the infall time in the post-shock region is several times larger compared to the free-fall time, especially due to the formation of turbulence in the post-shock region. Third, instead of only one possible shock transition, the flow shows the formation of two shocks, one very close to the black hole ($\sim$3–5) and the other farther away depending on the angular momentum. Both the shocks showed significant oscillations. While the inner shock oscillated faster than the outer shock, each of them also oscillated at the frequency of the other, though at a lesser power. These oscillations or their variants are long thought to cause the quasi-periodic oscillations (QPOs) observed in black hole intensity (Molteni et al. 1996; Chakrabarti et al. 2004). It is possible that not only the intermediate and low frequency QPOs are explained by this process, the high frequency QPOs may also be explained by the oscillations of the inner shock and the inner sonic point. However, since the volume of matter, participating in the inner shock oscillation is very small, the modulation at a high frequency would be negligible. We also observed that the outflows form from the post-shock region. The rates are especially high, and vary episodically. The amplitude and frequency of variation of the outflow rate is dictated by the amplitudes and frequencies of the two shocks. The outflow can be anywhere between 40 and 80 % of the inflow rate, provided the flow is sub-Keplerian. Since the Keplerian flows are subsonic, and therefore, strictly speaking no shocks, the outflows are not possible from a Keplerian disc in this model.

In Chap. 6, we have presented the results of the numerical simulations of two-dimensional, axisymmetric, viscous accretion flows. Three parameters, namely the specific angular momentum, the specific energy and the viscosity parameter determine the complete solution, although the results depend somewhat on the injection processes at the outer boundary. While both inviscid (Chakrabarti 1989) and viscous (Chakrabarti and Das 2004) flows allow solutions with or without centrifugal barrier dominated shock waves, we concentrated mostly on the cases when the shocks are formed. We find that the shocks move outward as the viscosity is enhanced and the post-shock region roughly attains a Keplerian distribution. When the viscosity parameter is very high, the shock moves to a large distance and the whole disc becomes a Keplerian disc. We also found that the condition of standing shock wave formation may be satisfied only in a range of the viscous parameter (keeping other parameters as constants), which is in line with the conclusions drawn in Chakrabarti and Das (2004). When the Rankine-Hugoniot conditions are not satisfied, the shocks tend to oscillate (Ryu et al. 1997; Giri et al. 2010) and the frequency of oscillation is decreased and amplitude is increased as the shock moves out. In the previous chapter, we emphasized the formation of a weaker inner shock closer to the black hole. This was not predicted by the theoretical works. In this paper, we find that this inner shock also becomes weaker and moves outward when the viscosity is introduced. The critical viscosity parameter for removal of the inner shock is lower than what is needed to remove the outer shock. It is well known that the light curves of radiation coming from an accretion disc around a black hole exhibit QPOs. It appears that in the absence of a hard surface, the standing shock itself behaves like a hard surface and

its oscillation changes the size of the post-shock region significantly. This could be the cause of the low and intermediate frequency QPOs (Chakrabarti and Manickam 2000; Rodriguez et al. 2004; Remillard and McClintock 2006; Gliozzi et al. 2010; Qu et al. 2010). When the viscosity is increased, the Keplerian rate is enhanced and at the same time, the shock recedes to a large distance and the time period is increased. Asymptotically, this means that a Keplerian disc should not show QPOs. We also observe that away from the equatorial plane, the angular momentum is sub-Keplerian (i.e. smaller compared to the specific angular momentum on the equatorial plane).

In Chap. 7, we simulated Two Component Advective Flow (TCAF). TCAF solution in the black hole astrophysics was formulated from the theoretical study of the behaviour of topology of viscous flows around black holes. One component having a higher viscosity is a cooler, Keplerian disc on the equatorial plane. The second component is a low angular momentum and low viscosity flow, which forms a standing or oscillating shock. The region between the shock and the inner sonic point behaves as a boundary layer (the centrifugal pressure supported boundary layer or CENBOL). Here, the kinetic energy of pre-shock matter is converted into thermal energy. The flow is puffed up and forms a geometrically thick disc, which is the hot Compton cloud. The CENBOL is the region that produces and collimates the outflows or jets. The spectrum is softer when the CENBOL is smaller or non-existent. The spectrum is harder when the CENBOL is present. When the CENBOL oscillates, low-frequency QPOs form. Furthermore, it is the only configuration which arises out purely from theoretical considerations. So it is important to prove that not only is the TCAF configuration realizable, it is also a stable system. So far, there are no numerical simulations in the literature to show that TCAF solution is realizable as a whole and there is no simulation to show whether such a configuration is at all stable. It is to be noted that in the literature, studies have been made on Bondi flows and thick accretion discs (e.g. Hawley et al. 1984a, b; Molteni et al. 1996; Igumenshchev and Abramowicz 2000), but a TCAF which is basically a combination of a generalized Bondi flow and a Keplerian disc in the pre-shock region, and a thick accretion disc and the outflow in the post-shock region has not been done. Our result, for the first time shows that if one assumes that the viscosity is maximum on the equatorial plane, then, a low-angular momentum injected flow is converted into a TCAF. We show that the injected flow segregated in the Keplerian and sub-Keplerian components. The sub-Keplerian component produced a shock at around $20r_g$ (this depends on the angular momentum of the injected flow) and the resulting CENBOL did not allow the Keplerian disc to have the normal structure up to innermost stable circular orbit or ISCO. The Keplerian flow remained extremely thin (about a grid thick) inside the CENBOL. However, for $r \geq 20r_g$, the density of the flow becomes very high and the temperature becomes very cool. The slope of the temperature distribution is in line with our choice of β. We have also shown that there is clearly a hysteresis effect in that, the time taken to form a Keplerian disc upon introduction of heating and cooling is faster than the time it takes to return to the original inviscid configuration. This is because the cooler matter of the Keplerian flow has lesser thermal drive to fall in. It is possible that the hysteresis effects seen in the outburst sources in the onset (turning on the viscosity) and the decline (turning off the viscosity) phases are

precisely due to this effect: the formation and the disappearance of the Keplerian flow takes different times.

The work developed in the thesis thus addresses very important and relevant issues on accretion processes around black holes. We wish to study the spectral properties for these systems. So far, we have captured all the salient features of the Keplerian disc by introducing a power-law cooling effect. In order to produce an exact standard disc that emits multicolour black body as well, we need to include the radiative transfer problem ab initio. We need to generate photons using bremsstrahlung and scatter them by the Keplerian (angular momentum) component to obtain black body radiation self-consistently. The emitted photons would then scatter from the CENBOL and the outflows and produce harder radiations, observed in black hole candidates. In the future, we plan to carry out this analysis.

We have simulated accretion flows around black holes in a two-dimensional hydrodynamics system. In the future, this work is to be evolved by more self-consistent work including three-dimensional magneto hydrodynamics and radiative transfer.

References

Chakrabarti, S. K. (1989). *Astrophysical Journal*, *347*, 365.
Chakrabarti, S. K. (1990). *Theory of transonic astrophysical flows*. Singapore: World Scientific.
Chakrabarti, S. K., & Das, S. (2001). *Monthly Notices of the Royal Astronomical Society*, *327*, 808.
Chakrabarti, S. K., & Das, S. (2004). *Monthly Notices of the Royal Astronomical Society*, *349*, 649.
Chakrabarti, S. K., & Manickam, S. G. (2000). *Astrophysical Journal*, *531*, L41.
Chakrabarti, S. K., Acharyya, K., & Molteni, D. (2004). *Astronomy and Astrophysics*, *421*, 1.
Giri, K., Chakrabarti, S. K., Samanta, M. M., & Ryu, D. (2010). *Monthly Notices of the Royal Astronomical Society*, *403*, 516.
Gliozzi, M., Rath, C., Papadakis, I. E., & Reig, P. (2010). *Astronomy and Astrophysics*, *512*, 21i.
Hawley, J. F., Smarr, L. L., & Wilson, J. R. (1984a). *Astrophysical Journal*, *277*, 296.
Hawley, J. F., Smarr, L. L., & Wilson, J. R. (1984b). *Astrophysical Journal*, *55*, 211.
Igumenshchev, I. V., & Abramowicz, M. A. (2000). *Astrophysical Journal*, *130*, 463.
Molteni, D., Sponholz, H., & Chakrabarti, S. K. (1996). *Astrophysical Journal*, *457*, 805.
Paczyński, B., & Wiita, P. J. (1980). *Astronomy and Astrophysics*, *88*, 23.
Qu, J. L., et al. (2010). *Astrophysical Journal*, *710*, 836.
Remillard, R. A., & McClintock, J. E. (2006). *Annual Review of Astronomy and Astrophysics*, *44*, 49.
Rodriguez, J., Corbel, S., Kalemci, E., Tomsick, J. A., & Tagger, M. (2004). *Astrophysical Journal*, *612*, 101.
Ryu, D., Ostriker, J. P., Kang, H. & Cen, R. (1993). *Astrophysical Journal*, *441*, 1.
Ryu, D., Chakrabarti, S. K. & Molteni, D. (1997). *Astrophysical Journal*, *474*, 378.